Investigation of the
Warm Conveyor Belt Inflow

a combined approach using airborne lidar
observations and ECMWF model simulations

Dissertation
an der Fakultät für Physik
der Ludwig–Maximilians–Universität
München

vorgelegt von
Andreas Schäfler
geboren in Friedrichshafen

München, November 2011

Erstgutachter: apl. Prof. Dr. U. Schumann

Zweitgutachter: Prof. Dr. G. C. Craig

Tag der mündlichen Prüfung: 2. März 2012

Parts of this thesis are contained in:

Schäfler, A., A. Dörnbrack, H. Wernli, C. Kiemle, and S. Pfahl, 2011: Airborne lidar observations in the in inflow region of a warm conveyor belt. *Q. J. R. Meteorol. Soc.*, 137: 1257–1272. DOI:10.1002/qj.827

iv

Contents

Zusammenfassung

Warme Förderbänder stellen dynamisch bedeutende Luftströme dar, die in extratropischen Tiefdruckgebieten auftreten. Feuchte Luftmassen werden aus dem Warmsektor der Zyklone polwärts in die Nähe der Tropopause gehoben. Die in Folge von Phasenübergängen eintretende Freisetzung latenter Wärme führt zu einer isentropenschneidenden Strömung der ansteigenden Luftmassen und zur Bildung von ausgedehnten Wolkenbändern und Niederschlag. Die Freisetzung latenter Wärme verstärkt die sich entwickelnde Zyklone. Das Ausströmen des warmen Förderbands im Tropopausenniveau beeinflusst die stromabwärtige Wetterentwicklung. Demzufolge beeinflussen Mängel in der Repräsentation von Feuchteprozessen sowie dem Transport von Wasserdampf in einem simulierten warmen Förderband die Qualität der Kurz- und Mittelfristvorhersage von numerischen Wettervorhersagemodellen.

Diese Dissertation untersucht erstmals einen umfangreichen Datensatz von flugzeuggetragenen Beobachtungen eines Doppler Wind Lidars (DWL) und eines Differentiellen Absorptions Lidars (DIAL), um Analysefehler im Einströmbereich von warmen Förderbändern aufzudecken, die durch das globale Wettermodell des Europäischen Zentrums für Mittelfristige Wettervorhersage (EZMW) simuliert werden. Der Fokus liegt dabei auf der frühen Phase der Entwicklung des warmen Förderbands, bevor Sättigung in der aufsteigenden Luftmasse eintritt, da Lidarmessungen nur unter wolkenfreien Bedingungen möglich sind. Basierend auf Trajektorienrechnungen wird ein großer Datensatz von Vertikalprofilen, der während mehrerer Forschungskampagnen gemessen wurde, hinsichtlich des Auftretens von warmen Förderbändern untersucht.

Während eines Forschungsflugs über der Iberischen Halbinsel, der im Rahmen der European THORPEX Regional Campaign (ETReC 2007) stattfand, wurde am 19. Juli 2007 ein warmes Förderband in der Grenzschicht unmittelbar vor dem starken Aufstieg beobachtet. Der Vergleich der Lidar-Feuchtemessungen mit Analysefeldern des EZMW zeigt eine signifikante Überschätzung der simulierten Feuchte von etwa 1 g kg^{-1} im Mittel für den Einströmbereich des warmen Förderbands. Eine Lagrangesche Feuchtequellendiagnostik zeigt, dass diese großen Abweichungen in Luftmassen auftreten, die vom westlichen Mittelmeer in Richtung Spanien transportiert wurden und eine starke Feuchteaufnahme über dem Ebro Tal aufweisen. Ungenauigkeiten in der Verdunstung vom Boden, der horizontalen Feuchteadvektion und dem vertikalen, turbulenten Transport von Feuchte in der Grenzschicht tragen zu den zu hohen simulierten Feuchtewerten in der Einströmregion dieses im Sommer aufgetretenen warmen Förderbands bei.

Eine Luftmasse im Einströmbereich eines warmen Förderbands wurde während eines am 19. September 2008, im Zuge der THORPEX Pacific Asian Regional Campaign (T-PARC) stattfindenden Forschungsflugs östlich von Japan beobachtet. Der Vergleich mit den Analysen des EZMW zeigt eine Überschätzung der Feuchte von ∼1,4 g kg^{-1}. Die Assimilation der mit Lidar gemessenen Wasserdampfdaten in das EZMW Globalmodell reduziert den Feuchtefehler auf ∼0,3 g kg^{-1}. Um den Einfluss des Feuchtefehlers in der Analyse auf die Vorhersagegüte quantifizieren zu können, werden zwei Vorhersageexperimente betrachtet. Eine Vorhersage, die den operationellen Feuchtefehler in den Anfangsbedingungen beinhaltet und eine andere, deren Feuchtefehler durch die Assimilation von DIAL-Messungen verringert wurde. In der Vorhersage mit verbesserter Feuchteanalyse (weniger Feuchte im Einströmbereich) wird weniger latente Wärme freigesetzt, was ein schwächeres warmes Förderband zur Folge hat. Der Anstieg der potentiellen Temperatur ist schwächer und der damit verbundene geringere vertikale Aufstieg führt zur Entwicklung einer schwächeren Zyklone (∼1,5 hPa). In Folge des Ausströmens in niedrigeren Höhen wird stromabwärtig eine niedrigere Tropopause (10-20 hPa), ein weniger stark ausgeprägter Rücken und ein schwächerer Strahlstrom (5-15 %) beobachtet. Ein Vergleich mit operationellen Analysen zeigt, dass der Feuchtefehler in der Analyse die Vorhersagegüte sowohl in Bezug auf die extratropische Zyklone als auch auf den Bereich des Ausströmens des warmen Förderbands verschlechtert.

Diese Arbeit zeigt, dass neuartige flugzeuggetragene Lidarbeobachtungen wertvoll sind, um die Feuchteverteilung im Einströmbereich von warmen Förderbändern zu untersuchen, sowie Analysefelder von numerischen Wettervorhersagemodellen zu validieren. Dabei bestätigt sich, dass die Einströmregion einen sensitiven Bereich für die Vorhersage extratropischer Zyklonen und des stromabwärtigen Wetters darstellt. Die gezeigten Methoden eignen sich sehr gut, um diese und andere (z.B. Troposphären/Stratosphären Austausch) Prozesse während geplanter Feldexperimente, wie beispielsweise das THORPEX - North Atlantic Waveguide and Downstream Experiment (T-NAWDEX), zu analysieren.

Abstract

Warm conveyor belts (WCBs) are key flow structures associated with extratropical cyclones. Moist air is transported from the cyclone's warm sector poleward and upward close to the tropopause level. The latent heat release due to phase changes leads to a cross-isentropic flow of the ascending airmasses and to the formation of elongated cloud bands and precipitation. The latent heat release amplifies the developing midlatitude cyclone. The WCB outflow near the tropopause modifies the weather downstream. Therefore, the insufficient representation of moist processes and moisture transport in the simulated WCB affect the short to medium-range forecast skill of numerical weather prediction (NWP) models.

This thesis, for the first time, investigates a comprehensive dataset of airborne observations by a Differential Absorption Lidar (DIAL) and a Doppler Wind Lidar (DWL) to reveal analysis errors in the WCB inflow region simulated by the European Centre for Medium-Range Weather Forecasts (ECMWF) Integrated Forecast System (IFS). The investigation focuses on humidity and wind observations in the early stage of the WCB development, before the air saturates, as lidar measurements are only feasible under cloud free conditions. Based on the calculation of trajectories, a large number of vertical profiles measured during several research campaigns are evaluated with regard to WCB encounters. Two identified cases form the basis to investigate the origin of the moisture errors and their impact on the forecast skill.

On 19 July 2007, a research flight over the Iberian Peninsula during the European THORPEX Regional Campaign (ETReC 2007) intersected a WCB in the boundary layer inflow region just prior to the strong ascent. Comparison of lidar humidity measurements with ECMWF analyses reveals a significant overestimation of the simulated humidity in this low-tropospheric WCB inflow region of about $1\,\mathrm{g\,kg^{-1}}$ on average. A Lagrangian moisture source diagnostic shows that these large deviations occur within airmasses that are transported from the western Mediterranean towards Spain and experience intense moisture uptake over the Ebro valley. Inaccuracies in surface evapotranspiration, in horizontal moisture advection and in turbulent vertical transport of moisture in the atmospheric boundary layer contributed to the erroneous humidity in the inflow region of this summertime WCB over Spain in the ECMWF analyses.

A WCB inflow airmass was observed east of Japan during the THORPEX Pacific Asian Regional Campaign (T-PARC) research flight on 19 September 2008. The comparison with the ECMWF analysis fields reveals a model moist bias in the WCB inflow of $\sim$1.4 g kg^{-1} on average. The assimilation of the lidar water vapour data into the ECMWF IFS reduces the bias to $\sim$0.3 g kg^{-1}. Two forecast experiments are performed to quantify the impact of the moisture analysis error on

the forecast skill: One with the operational analysis containing the moisture bias and another one where the moisture bias was reduced through the assimilation of DIAL observations. Less latent heat is released at lower levels in the forecast with improved moisture analysis (less moisture in the WCB inflow) resulting in a weaker WCB. The increase of potential temperature is lower and the reduced vertical lifting weakens the surface cyclone ($\sim$1.5 hPa). As a result of the WCB outflow at lower altitudes, a lower tropopause (10-20 hPa), a less pronounced ridge and a weaker jet stream (5-15 %) are found downstream. A comparison with operational analyses shows that the errors in the moisture analysis degrade the forecast skill, both of the midlatitude cyclone and the WCB outflow.

This thesis demonstrates that novel airborne lidar observations are useful to study the moisture distribution in WCB inflow regions and to validate analysis fields of NWP models. It is confirmed that WCB inflow regions represent sensitive regions for the forecast of extratropical cyclones and the weather downstream. The presented methods are ideally suited to analyse these and other (e.g. stratosphere/troposphere exchange) processes during envisaged field experiments, e.g. the THORPEX - North Atlantic Waveguide and Downstream Experiment (T-NAWDEX).

Chapter 1

Introduction

In the present-day fast moving world, accurate numerical weather forecasts play a crucial role in almost all aspects of life. For example, commercial sectors such as aviation or energy industry strongly depend on reliable forecasts ranging from hours to 1-2 weeks. The midlatitude weather is dominated by the sequence of cyclones and anticyclones that develop in conjunction with upper-level, synoptic-scale Rossby waves propagating along wave guides at the tropopause. During the last few decades, short and medium-range forecasts of operational numerical weather prediction (NWP) models have been continuously improved (e.g. ECMWF Annual Report 2010[1]). Enhanced spatial resolution, advanced physical parameterizations for subgrid-scale processes, advanced data assimilation methods and the increasing usage of satellite observations in data assimilation systems have fundamentally improved the forecast skill (Simmons and Hollingsworth 2002). Despite this general improvement, there still exist error sources affecting the skill of the NWP. Forecast errors in NWP models mainly result from model errors due to limitations in resolution or parameterization of sub-grid scale processes and from errors contained in the initial conditions, also called analysis errors.

Initial condition errors and model insufficiencies in a low pressure system can have a substantial impact on the medium-range forecast. In particular, the representation of latent heat release within warm and moist airmasses remains a crucial limitation of the model physics (Persson and Grazzini 2007). Didone (2006) found characteristic error patterns along the jet stream of predictions of the ECMWF Integrated Forecast System (IFS). These forecast errors could be traced back to an inaccurate representation of diabatic effects which eventually altered the upper tropospheric flow and resulted in an erroneous prediction of propagating Rossby waves (Dirren et al. 2003). This means, inaccurately represented diabatic processes are

---

[1]http://www.ecmwf.int/publications/annual_report/

a possible source of reduced forecast skill of cyclone developments in NWP models. On the other hand, analysis errors may also strongly influence the large scale dynamics, especially if they occur in dynamically sensitive areas, for example in regions of cyclogenesis (Persson and Grazzini 2007).

Latent heat release due to diabatic processes is particularly intense in the rising air of a so-called warm conveyor belt (WCB). A WCB denotes an ascending airflow carrying air parcels from the southern midlatitude boundary layer to the northern midlatitude upper troposphere in 1-2 days (Browning et al. 1973; Carlson 1980; Wernli and Davies 1997). As a result of the latent heat release the potential temperature increases during the ascent (cross-isentropic transport). Diabatic processes in WCBs are vitally important as they strongly influence both the life cycle of individual extratropical cyclones (Grams et al. 2011) and, on a global scale, the midlatitude general circulation (Eckhardt et al. 2004). Cyclones and anticyclones mainly reduce the meridional temperature contrast between polar and equatorial regions. The poleward transport of sensible and latent heat by WCBs is a key component of the overall atmospheric meridional energy transport in midlatitudes.

Condensation processes in the coherently ascending airstream produce a positive potential vorticity (PV) anomaly in the lower troposphere roughly at the level of maximum latent heating (Wernli and Davies 1997). This positive diabatic PV modification can intensify the subsequent life cycle of a cyclone (e.g. Kuo et al. 1991; Davis et al. 1993; Rossa et al. 2000). Above the level of maximum latent heating, PV is destroyed by diabatic processes leading to negative PV anomalies in the upper tropospheric WCB outflow region (Wernli 1997; Pomroy and Thorpe 2000; Grams et al. 2011). This modification of upper tropospheric PV, usually occurring at the level of the midlatitude jet stream, can significantly affect the downstream Rossby wave development and the associated surface weather (Massacand et al. 2001; Knippertz and Martin 2005).

The amount of moisture that is transported by the WCB airstreams depends on the available moisture in the atmospheric boundary layer as shown by Boutle et al. (2011). They investigated the moisture transport in midlatitude cyclones by means of idealized simulations and found that increased moisture near the surface leads to higher latent heat release and intensifies the eddy kinetic energy of the storms. This points to a high sensitivity of the cross-isentropic WCB flows to the boundary layer humidity in regions where air parcels start their ascent. Boutle (2009) states that an improved understanding of water vapour transport in WCBs and, especially, the verification of the correct representation of the WCB inflow humidity are key scientific challenges to improve the forecasts. The WCB inflow represents a moist airmass typically located in the warm sectors of developing cyclones. On the one

hand, the WCB inflow moisture content is determined by surface latent heat fluxes over ocean and over land and, on the other hand, by large-scale horizontal transport of water vapour. The enhanced boundary layer humidity converges within the WCB inflow region. According to Boutle et al. (2010) most of the boundary-layer moisture in midlatitude cyclones is transported vertically by WCBs and by shallow cumulus convection. The boundary layer moisture can also impact the precipitation distribution and therefore plays an important role for NWP (Keil et al. 2008).

Given the dynamical relevance of WCBs, it is striking that only few observational studies have been made to better characterize the properties of these airstreams (e.g. Esler et al. 2003; Vaughan et al. 2003) and to identify shortcomings in their representation in NWP models. So far, the analysis of the moisture content in the WCB inflow and the latent heating along the WCB ascent is almost entirely based upon NWP data. Accordingly, there is a demand for observations of the moisture transport within extratropical cyclones. These observations allow for detailed verification and forecast sensitivity and impact studies.

Most of the previous studies using aircraft data to investigate WCBs and cyclones map their thermodynamic structure by means of in-situ measurements and dropsondes. Additionally, ground-based radar data and satellite imagery were interpreted to investigate WCBs (e.g. Browning et al. 1973). Airborne lidar (light detection and ranging) measurements provide an alternative possibility to observe the tropospheric structure void of dense clouds, which has not been used to investigate WCBs before. During the recent years, airborne measurements with lidars of both wind and water vapour have been conducted successfully to investigate numerous meteorological phenomena in the extratropics. For example, Browell et al. (1987) and Hoinka and Davies (2007) investigated the structure of stratospheric intrusions. Flentje et al. (2005) used water vapour observations to illustrate the mesoscale fine structure of extratropical cyclones. Flentje et al. (2007) first evaluated ECMWF model simulations using lidar water vapour measurements in the tropics and subtropics over the Atlantic Ocean between Europe and Brazil. Schäfler et al. (2010) presented a method to determine the horizontal water vapour transport from collocated water vapour and wind lidar measurements in the vicinity of an extratropical cyclone. Lidar observations were also successfully used for data assimilation and forecast sensitivity studies that showed a beneficial impact on forecast skill (e.g. Weissmann and Cardinali 2007; Kamineni et al. 2006). A recent study by Harnisch et al. (2011) showed that the assimilation of water vapour lidar data is able to reduce analysis errors of moisture in the ECMWF global model.

This thesis addresses the need for a better characterization of WCBs with observations and takes the challenge to find suitable lidar observations of WCB airstreams in data sets from several airborne field campaigns performed in recent years with a state-of-the-art Doppler Wind Lidar (DWL) and a Differential Absorption Lidar (DIAL). As lidars cannot penetrate optically thick clouds, this thesis focusses on observations in the early phase of the cyclone development, i.e. in the inflow of WCBs before the air in the ascending flow saturates. In contrast to the previous studies using lidar data this work investigates the Lagrangian transport leading to the observed structures by combining lidar observations with data from a global NWP model.

This thesis treats the following three key scientific questions:

- **Q1:** Are any of the airborne lidar observations in the data pool of past international field experiments suitable to characterize the inflow of WCBs? Does the comparison of these independent measurements with NWP models reveal significant analysis errors?

- **Q2:** Where does the moisture in the inflow of a WCB originate? How do the different locations of the moisture uptake affect the observed humidity distribution?

- **Q3:** How do analysis errors in the humidity fields of a WCB inflow impact the subsequent forecasts of the associated cyclone and the downstream weather?

The NWP model used in this thesis to quantitatively analyse WCB inflows and their representation is the global IFS running operationally at the ECMWF (Persson and Grazzini 2007). For the first time, a Lagrangian diagnostic is employed to identify WCB measurements within lidar data. Based on these trajectory calculations the transport characteristics of the observed airmass and the influence of moisture uptake on the distribution of humidity in the WCB inflow and associated errors are investigated. As the DIAL data are not incorporated in the operational ECMWF analyses, they provide an independent verification data set that sheds light on possible analysis errors. Additionally, the DIAL data are assimilated in a sensitivity experiment using the ECMWF IFS to investigate the impact of improved humidity fields in the inflow of a WCB on the forecast of an extratropical cyclone and the weather downstream.

An additional task of this thesis is the assessment of the applicability and the benefit of airborne lidar instruments for future measurement efforts. In particular, it is shown when and where these observations are useful to characterize essential properties of a WCB. In this way, the results contribute to the preparation of the

envisaged field experiment T-NAWDEX (THORPEX[2] - North Atlantic Waveguide and Downstream Impacts Experiment). The overarching goal of this field experiment will be the experimental investigation of physical processes that are responsible for the degradation of forecast skill in the midlatitudes of the North Atlantic and Europe. One main focus is the observation of diabatically modified airmasses which impact the tropopause dynamics. The outcome of this thesis shall help to optimally deploy lidar instruments during T-NAWDEX.

The thesis is structured as follows. **Chapter 2** addresses the important role of WCBs for the extratropical weather. First, conceptual models that describe the structure and evolution of cyclones in an Eulerian and Lagrangian framework are discussed. The relevance of WCBs for the midlatitude circulation and the influence of the moist processes associated with WCBs on weather systems are explained from a PV perspective. A case study is used to illustrate the WCB transport and the impact on atmospheric dynamics. The theoretical considerations of chapter 2 will be summarized with regard to the research aims of this thesis.

Chapter 3 investigates research questions **Q1** and outlines the methodology of this thesis. It gives an overview of the applied lidar methods and the theoretical background of DIAL and DWL measurements. Additionally, the ECMWF model IFS is described and an overview of data assimilation and the use of DIAL data is provided. WCBs are identified by calculating Lagrangian trajectories. Their computations are explained together with the moisture uptake analysis method. A further aspect of chapter 3 is the selection of suitable WCBs. Over the past years the DLR research aircraft Falcon was involved in several international research campaigns with different scientific objectives. However, none of these studies specifically aimed to measure WCBs - neither in their lower tropospheric inflow, nor in the outflow near the tropopause. The used lidar data set and the selection of two cases are discussed together with the suitability to address research questions Q2 and Q3.

Chapter 4 focuses on research questions **Q2** and comprises a first case study on an aircraft mission during the European THORPEX Regional Campaign (ETReC) on 19 July 2007. The detailed analysis of the meteorological situation and the WCB observations over the Iberian Peninsula is followed by the quantification of moisture errors in the WCB inflow. The analysis and discussion of the moisture transport and the detailed moisture uptake analysis results in an explanation for the development of the moisture errors in the WCB inflow.

---

[2]The Observing System Research and Predictability Experiment (THORPEX) is a 10-year research program of the World Meteorological Organization (WMO), http://www.wmo.int/pages/prog/arep/wwrp/new/thorpex_new.html

A second case study on a mission from the THORPEX Pacific Asian Regional Campaign (T-PARC) on 19 September 2008 east of Japan is the topic of **chapter 5** and mainly deals with research question **Q3**. After the general analysis and discussion of the WCB measurements, this case study focuses on the impact of moisture analysis errors in the WCB inflow on the forecast of an extratropical cyclone and the weather downstream.

Chapter 6 contains the discussion of the main results and concludes this thesis. An outlook on upcoming field experiments and the benefits of deploying airborne lidar instruments is given in **chapter 7**.

Chapter 2

Warm conveyor belts - a key element of extratropical cyclones

The global atmospheric circulation of the rotating earth is mainly driven by the imbalance of the radiative heating between pole and equator. As a consequence, a meridional temperature gradient is typically observed in the midlatitudes which causes vertical wind shear according to the thermal wind relation. The increase of wind speed with height forms a strong westerly flow known as the jet stream. Rossby waves are upper-level disturbances of the jet stream which can interact with the meridional temperature gradient and force the development of synoptic-scale cyclones at lower levels (Holton 2004). Once amplified the large-scale Rossby waves meander around the entire hemisphere with a sequence of troughs and ridges. Extratropical cyclones occur in a variety of forms and in different evolution stages. Their structure depends on the background flow, moisture supply and the surface conditions (Wallace and Hobbs 2006).

This chapter gives an overview of the structure and evolution of cyclones focusing on the related WCB. Section 2.1 discusses conceptual models to understand the highly complex, three-dimensional structures and physical processes in developing cyclones as well as their life cycle both from an Eulerian and a Lagrangian perspective. Section 2.2 discusses the relevance of the WCB for the midlatitude circulation. The WCB is discussed from a PV perspective with special focus on the importance of the associated moist processes for the development of the cyclone (section 2.2.1). In a case study (section 2.2.2 and 2.2.3), the PV perspective is combined with the Lagrangian and Eulerian viewpoint to highlight the complexity of the three-dimensional WCB dynamics and its impact on the midlatitude weather. Additionally, the climatological importance is discussed (section 2.2.4). Section 2.3 summarizes the key aspects of this chapter with regard to main aims of this thesis.

2.1   Conceptual models

Eulerian perspective

The Eulerian view point describes the structure and evolution of cyclones in successive time steps. Research in extratropical cyclones goes back to the late 18th century (Davies 1997, and references therein) and led to the Norwegian polar front cyclone model developed by the Bergen school around 1920 (Bjerknes 1919; Bjerknes and Solberg 1922). The group of Scandinavian researchers analysed surface-based observations to describe the structure of the cyclone in terms of frontal zones and airmasses with different origin and thermodynamic properties. They empirically linked these structures to typical local weather phenomena (clouds, rain and wind). Figure 2.1(a) shows the characteristic stages of the cyclone's life cycle in the Norwegian cyclone model.
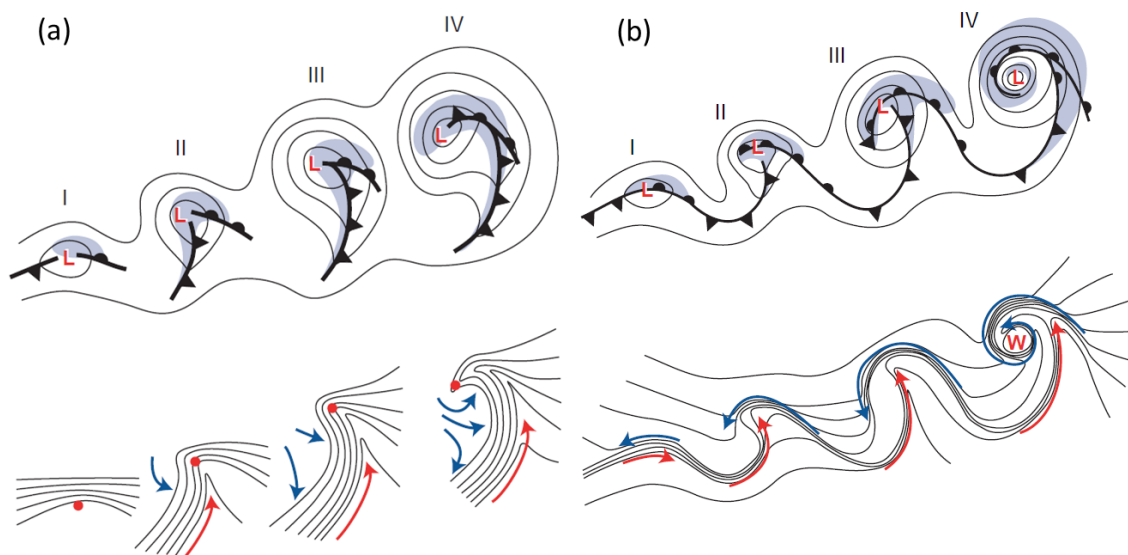

Figure 2.1: Schematic showing four stages in the development of extratropical cyclones as envisioned in (a) the Norwegian polar front cyclone model and (b) the Shapiro-Keyser model. Panels I, II, III and IV represent four successive stages in the life cycle. (Top) Idealized frontal configurations and isobars. Shading denotes regions of precipitation. (Bottom) Isotherms (black) and airflow (coloured arrows) relative to the moving cyclone centre (red dot). Red arrows indicate the flow in the warm sector, and blue arrows indicate the flow in the cold airmass. Figures taken from Wallace and Hobbs (2006).

The Bergen school also established the concept of the polar front which refers to the strong temperature gradient between polar and tropical airmasses. They showed that cyclones develop from an incipient wave in the polar front with a cold and a warm front starting to rotate around the surface low (Figure 2.1(a), I). The cyclone deepens (decrease of surface pressure) while the associated thermal gradient distorts and a warm sector forms between the cold and the warm front (Figure 2.1(a), II).

The warm sector narrows as the cold front circulates faster around the cyclone than the warm front (Figure 2.1(a), III) which finally causes an occluded front in the mature stage of the cyclone (Figure 2.1(a), IV). During the evolution of the cyclone, cold air is transported southward on the rear side of the cyclone and warm air is advected northward in the warm sector. The Norwegian model depicts a strong cold front and a short and weak warm front.

In the years after the Norwegian cyclone model was developed, innovations in theory and observing technology (e.g. radiosonde, satellite or radar data) as well as the use of NWP enabled the investigation of e.g. baroclinic instability, interaction of upper-level flow with surface fronts, frontal structure, tropopause and the constitution of related conceptual models (Shapiro et al. 1999, and references therein). Beside important theoretical studies (e.g. Charney 1947; Eady 1949), especially the observations during field experiments contributed to the understanding of the physical processes in extratropical cyclones. In the 1980s, a series of field experiments were performed on both sides of the Atlantic Ocean. On the east coast of North America, the Genesis of Atlantic Lows Experiment (GALE, Dirks et al. 1988) and the Experiment on Rapidly Intensifying Cyclones (ERICA, Hadlock and Kreitzberg 1988) observed the life cycle of cyclones and the associated fronts. On the European side, the FRONTS-87 campaign made mesoscale observations to investigate the dynamics of cold fronts in Atlantic cyclones approaching northwest Europe. During the Fronts and Atlantic Storm-Track Experiment (FASTEX) in 1997, the whole life cycle of cyclones over the Atlantic Ocean and the large scale flow interaction was studied (Joly et al. 1999).

Based on these field campaigns, the detailed analysis of the cloud structure and temporal evolution of various cyclones resulted in a further depiction of the evolution stages of a different type of cyclones named the Shapiro-Keyser model (Shapiro and Keyser 1990). This conceptual model roughly equals the Norwegian cyclone model during the first two stages (I and II in Figure 2.1(b)). However, the cyclone possesses a strong warm front and a perpendicularly moving weaker cold front (see T-bone shape in Figure 2.1(b), III). In contrast to the Norwegian model, no occlusion develops and the warm airmass moves northward around the cyclone centre and builds the so-called bent back warm front (Figure 2.1(b), III). At the latest stage, cold air spirals inward and forms a secluded warm core (Figure 2.1(b), IV). The Shapiro-Keyser cyclones are elongated in east-west direction whereas the Norwegian cyclones with their stronger cold front are meridionally elongated.

Numerical studies showed that the upper-level flow largely impacts the structure of the cyclone. For example Schultz et al. (1998) showed that variation of the wind speed along the jet stream influences the evolution of the cyclone. A confluent

wind field in the jet entrance region favours the development of a zonally elongated Shapiro-Keyser like cyclone, whereas the cyclones that develop in the diffluent jet exit region resemble the Norwegian type. Other studies showed that the cross-jet wind variation also influences the structure of the cyclone (Shapiro et al. 1999, and references therein). In a cyclonic-sheared environment, the development of Norwegian occluded cyclones are favoured whereas the Shapiro-Keyser cyclone develops under conditions without strong shear in cross-jet direction. A third category of cyclones which does not occlude (open wave cyclone) develops in an anticyclonically sheared environment.

Lagrangian perspective

Extratropical cyclones were also investigated from a Lagrangian point of view considering the three-dimensional airflow through baroclinic systems. The Lagrangian point of view developed in association with the above mentioned improvement of observational techniques that allowed exploring radiosonde and radar data to better understand the cloud and rain distribution in cyclones. By analysing winds on isentropic (dry areas) and moist-isentropic surfaces (saturated areas) deduced from radiosonde observations, the system relative motions could be investigated. In this Lagrangian framework so-called conveyor belts delineate the major airstreams within extratropical cyclones. Based on previous studies (e.g. by Browning et al. 1973; Harrold 1973), Carlson (1980) first assembled a conceptual model that shows three discrete airstreams in a moving cyclone. Figure 2.2 shows a schematic of the major transport pathways defined by characteristic pathways and properties that will be explained in the following.

The WCB transports moist and warm air from the planetary boundary layer (PBL) of the warm sector ahead of the cold front upward and poleward. It was first identified by Harrold (1973) with the above mentioned isentropic analysis. In recent years, the calculation of Lagrangian trajectories allowed the definition of objective criteria to identify WCB airmasses in cyclones (e.g. the selection of trajectories with the highest change of pressure over a certain time interval). It was shown that the typical time scale of the WCB ascent amounts to ∼48 h (Wernli and Davies 1997). During the ascent, the air saturates and the resulting latent heat release by condensation influences both the evolution of individual extratropical cyclones and the general circulation (see section 2.2.2). The slantwise ascending airstream forms an extended and often anticyclonically curved cloud band of dense medium and high level clouds. When the WCB air reaches the upper troposphere, the flow typically turns anticyclonically into the jet stream towards the downstream anticyclone. For
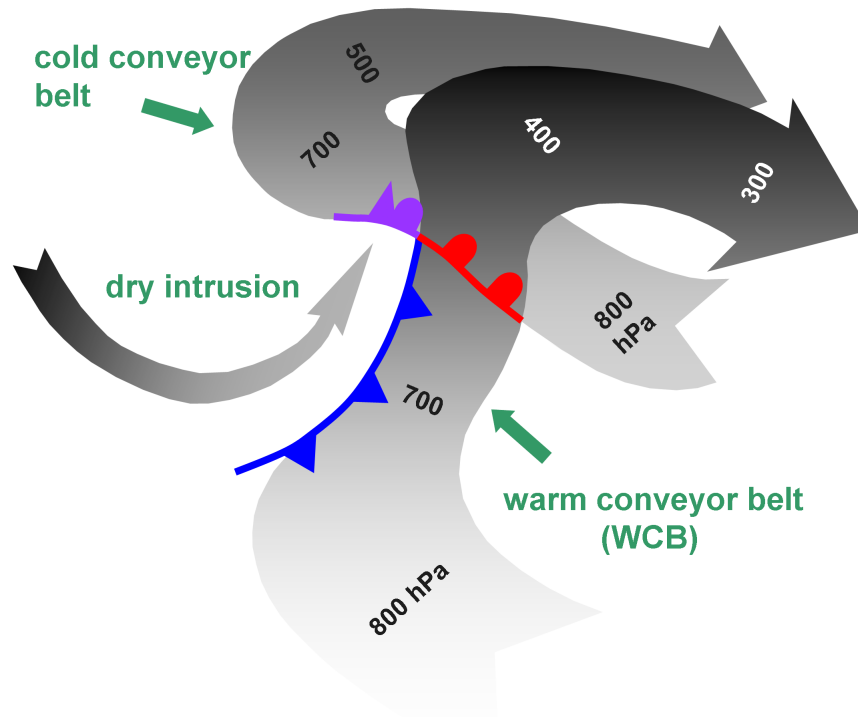
Figure 2.2: Conveyor Belt Concept following Bader et al. (1995) adapted from Carlson (1980). Grey shading indicates the altitude of the transported airmass (dark colours correspond to high altitudes). Surface fronts of a developing cyclone are shown by the red line with semi circles (warm front), blue line with triangles (cold front) and in purple (occluded front).

the case that the upper-level trough separates from the jet stream and forms a closed cyclone, which often happens in the late occluded phase of the cyclone evolution, the air in the WCB outflow can also turn cyclonically to the west (Martin 1999).

Another discrete airstream is the Cold Conveyor Belt (CCB) which originates northeast of the developing cyclone and north of the warm front at lower levels. It was first mentioned by Carlson (1980) and called CCB as colder air is transported westward ahead of the warm front and below the ascending WCB. In the concept of Carlson (1980), CCB air rises north of the cyclone centre and turns anticyclonically to the east. However, other studies report cyclonic flow at almost constant altitudes which occurs in the closed circulation of the low near the surface (Schultz 2001).

Airstreams from the upper troposphere and lower stratosphere (UT/LS) towards lower altitudes west of northern-hemispheric cyclones are named dry intrusion (Danielsen 1964). The transported cold and dry air has a clear signature in infra-red satellite images and is identifiable by an almost cloud free region (dry slot) behind the surface cyclone (e.g. Browning 1997).

2.2   Relevance for extratropical dynamics

2.2.1   WCB from a potential vorticity perspective

Intense latent heat release occurs in association with cloud formation and precipitation in the poleward ascending WCB. The influence of diabatic processes on the life cycle of cyclones and the atmospheric dynamics can be best illustrated with the aid of the "PV Thinking" concept, a fundamental approach introduced by Hoskins et al. (1985). Many studies used the quantity of PV to study the development and life cycle of cyclones. This section gives a concise description of the PV concept and the effect of latent heat release in WCBs on the dynamics of cyclones. This survey bases on the comprehensive reviews of the PV framework by Ahmadi-Givi (2002) and Wernli (2009).

The Ertel PV (Ertel 1942) combines information from the temperature and wind field and is defined as

$$Q = \frac{1}{\rho} \vec{\eta} \cdot \vec{\nabla} \theta, \tag{2.1}$$

where ρ is the density, θ is the potential temperature and $\vec{\eta}$ is the vector of the absolute vorticity $\vec{\eta} = \vec{\nabla} \times \vec{v} + 2\vec{\Omega}$ where $\vec{\nabla} \times \vec{v}$ and $2\vec{\Omega}$ are the relative and planetary vorticity, respectively. For synoptic scale motions the vertical component of $\vec{\eta}$ dominates and therefore PV in pressure coordinates can be approximated as

$$Q \cong -g\left(f + \zeta_p\right) \frac{\partial \theta}{\partial p}, \tag{2.2}$$

where $f = 2\Omega \sin \phi$ is the Coriolis parameter and $\zeta_p = \partial v/\partial x - \partial u/\partial y$ the vertical component of the relative vorticity in pressure coordinates. PV is therefore the product of the absolute vorticity and the static stability and usually given in Potential Vorticity Units [PVU] which are equivalent to $[10^{-6}~\mathrm{m}^2~\mathrm{s}^{-1}~\mathrm{K}~\mathrm{kg}^{-1}]$. From equation 2.2 it is obvious that PV increases towards higher latitude (increase of f). PV also varies with the synoptical flow structure and is generally higher in cyclonic flows ($\zeta_p > 0$) e.g. in upper-level troughs. It was shown by Hoskins et al. (1985) that dynamical structures like troughs and ridges that can be identified on isobaric charts are related to typical advection of stratospheric (trough) and tropospheric (ridge) air on isentropic surfaces (surfaces of constant potential temperature). These airmasses feature anomalously high tropopause heights in case of ridges whereas troughs possess anomalously low tropopause heights. Additionally, PV increases with higher stratification. Particularly, the transition from the troposphere to the stably stratified stratosphere leads to an abrupt increase of PV. The 2 PVU isosurface is therefore often defined as the dynamical tropopause (e.g. Birner

2006). Section 2.2.2 will give an overview of the PV distribution in the troposphere.

A key principle of "PV Thinking" is the conservation of PV in case of isentropic movements of air which is the case for adiabatic and frictionless flows. Then

$$\frac{DQ}{Dt} = 0 \qquad (2.3)$$

where the total derivation of PV denotes the temporal change for a moving air parcel. As the potential temperature is also conserved in adiabatic and frictionless flows the advection of PV can be visualized on isentropic maps. Adiabatic conditions are usually given in the free troposphere away from moist processes. A further key principle of PV is its invertibility which means that the balanced flow associated with a PV anomaly can be deduced solely from the PV distribution and the surface potential temperature.

However, PV is not conserved in the presence of radiative processes, surface fluxes or moist processes (e.g. condensation) that are summarized as diabatic processes and introduce heat to an air parcel which changes its potential temperature. Additionally, PV can be generated by frictional processes. Accordingly, PV is generated or destroyed and no longer conserved and the following equation is valid

$$\frac{DQ}{Dt} = -g\vec{\eta_p} \cdot \vec{\nabla}_p \dot{\theta} - g\vec{\nabla}_p \theta \cdot \left(\vec{\nabla}_p \times \vec{F} \right) \qquad (2.4)$$

that shows two source terms that are added to equation 2.3. The first term on the right hand side sums all processes that cause latent heating with the total diabatic heating rate $\dot{\theta}$ [K s^{-1}]. The second term ($\vec{F}$ is the three dimensional frictional force) denotes PV generation by frictional forces that are most relevant close to the ground. In the following the discussion focuses on the release of latent heat which is known to be the most important diabatic process in extratropical cyclones (e.g. Stoelinga 1996, see also discussion in section 2.2.3). Under the assumption that the third component dominates equation 2.4 is approximated as

$$\frac{D}{Dt}Q \cong -g\left(f + \zeta_p\right)\frac{\partial\dot{\theta}}{\partial p}. \qquad (2.5)$$

Since $f + \zeta_p$ is usually positive, PV is generated as long as the diabatic heating rate increases with decreasing pressure $\left(\partial\dot{\theta}/\partial p < 0\right)$ which is the case below the level of maximum heating. Above, where $\partial\dot{\theta}/\partial p > 0$ PV is destroyed. This explains the observed high diabatically generated PV values of WCBs in the lower troposphere and low or slightly negative PV values along WCBs in the upper troposphere of the downstream ridge.

Based on the quoted PV properties, Hoskins et al. (1985) created a conceptual model to explain the development of baroclinic cyclones that bases on the interaction of different PV features, i.e. a positive PV anomaly near tropopause associated with an upper-level trough, a diabatically induced positive PV anomaly at low levels and a surface potential temperature anomaly. Cyclogenesis takes place when the upper-level anomaly approaches a surface baroclinic zone. The cyclonic circulation extends downward and causes a warm anomaly by advecting warm air northward. This warm anomaly equals a cyclonic circulation which may propagate upward and enhance the upper-level PV anomaly. In the original concept of Hoskins et al. (1985) diabatic processes play only a secondary role. They are expected to reduce the static stability and amplify the interaction process by alleviating the vertical propagation of PV induced wind fields.

In the framework of "PV Thinking" the invertibility principle is often used to study the role of different PV anomalies in the development of the cyclone. A large number of theoretical and numerical studies as well as various case studies investigate the role of latent heat induced PV anomalies on the formation of extratropical cyclones. Ahmadi-Givi (2002) classifies these studies into two categories. One group assigns a secondary role to the release of latent heat like in Hoskins et al. (1985). Here, diabatically generated PV anomalies increase the surface warm anomaly and also the upper-level anomaly. The second category of studies found a strong impact on the cyclone intensity. For example Stoelinga (1996) studied the role of diabatic heating in an Atlantic cyclone and found that for this particular case the low level PV anomaly contributed approximately 70 % to the strength of the low level cyclone. It was also found that the diabatic PV improved the coupling of lower and upper-level waves. In some cases with very strong latent heat release even the extent of the upper-level positive PV anomaly is reduced (Ahmadi-Givi et al. 2004). Ahmadi-Givi (2002) speculates that the large differences in influence on the studied cyclones results from the high variability of their structure, motion and variability which also complicates a general view on the diabatically modified systems.

For the generation of a positive PV anomaly in the lower troposphere WCBs play an important role as within the fast ascending airstream latent heat is continuously released. Pomroy and Thorpe (2000) and Wernli and Davies (1997) show that PV is generated below the level of maximum latent heating. Above the level of maximum heating PV is reduced which causes the generation or intensification of negative PV anomalies in the WCB outflow region close to the tropopause. The upper tropospheric modification of PV can have a significant impact on the Rossby wave development and the surface weather downstream. Massacand et al. (2001) show that upstream diabatic processes can strengthen the downstream negative PV

anomaly which, in turn, changes the structure of a farther downstream located PV-streamer and its associated surface cyclone. The influence of the diabatic heating on the downstream cyclone development is also investigated by Grams et al. (2011). They used PV inversion to investigate the impact of a WCB in association with a TC which moved to the midlatitudes and changed over to an extratropical cyclone. By removing the entire TC from the background field, it is shown that the removed storm and the diabatic processes within a WCB substantially changed the upper-level PV structure and decreased the jet stream wind speeds from 80 to 60 m s^{-1}.

Figure 2.3 summarizes the evolution of key meteorological parameters in the flow through a typical WCB. The ascent from the boundary layer to the upper troposphere (Figure 2.3(a)) ahead of the cold front is accompanied by a release of latent heat in consequence of condensational processes in the saturated air. Therefore the amount of moisture in the inflow region is reduced by up to 2 orders of magnitude (Figure 2.3(b)). The potential temperature is increased due to latent release (Figure 2.3(c)) which causes a relative maximum of PV ($\sim$1.5 PVU, is shown in Figure 2.3(d)) in the lower troposphere and low PV values (< 0.5 PVU) in the tropopause region.
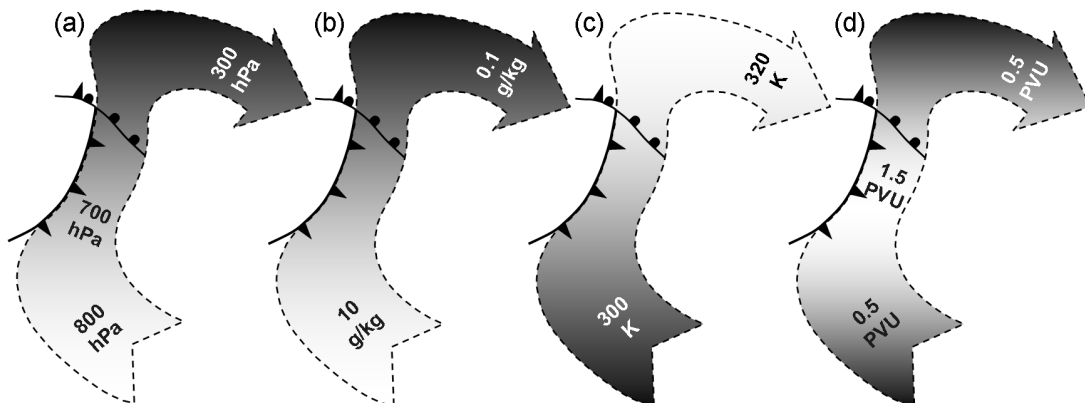

Figure 2.3: Schematic of the WCB with the typical evolution of (a) pressure, (b) specific humidity, (c) potential temperature and (d) PV. Grey shading indicates transition from high values (white) to small values (black) for the respective parameter. Surface fronts of a developing cyclone are shown by the black lines with semi circles (warm front), triangles (cold front) and both (occluded) front.

2.2.2   WCBs in an exemplary flow pattern

The following exemplary case will elaborate the importance of the WCB cross isentropic transport for midlatitude dynamics relying on the conceptual and theoretical considerations of the foregoing chapter. The Lagrangian view point (WCB trajectories) is combined with Eulerian snap shots (synoptic charts) that depict the flow

structure. The upper-tropospheric flow is discussed with isobaric and isentropic maps. The discussion is supported by a cross section that depicts the PV, potential temperature and wind distribution. With respect to the observations that are discussed later in this thesis, this will help the reader to understand the complexity of the 4-dimensional WCB transport within an evolving cyclone. WCB airmasses that ascended between 7 and 9 September 2008 are identified. The time period is chosen as two WCBs developed at about the same time in association with low pressure systems over the Pacific and Atlantic Ocean. Note, this case represents a common flow configuration in the Northern Hemisphere with Rossby waves meandering that initiate cyclogenesis and cause WCBs.

Figure 2.4(a) shows the upper-level flow in terms of geopotential height and wind speed at 300 hPa for 12 UTC 8 September 2008 based on ECMWF operational analyses (see section 3.2.1 for a description of the ECMWF data). The northern-hemispheric flow is characterized by a zonal jet stream over the Atlantic and a broad trough over eastern North America. Over the eastern Atlantic and Europe the jet stream splits up in two branches around a blocking anticyclone over the Norwegian Sea. A zonal jet stream further east is followed by a distinct undulation of shorter waves over eastern Asia and the Pacific Ocean.

Figure 2.4(b) illustrates PV on the 330 K isentropic surface. The 330 K isentropic surface was chosen as both WCB outflows are located at about this potential temperature level. The distribution of PV shows that the poleward ascending isentrope crosses the tropopause at midlatitudes with a strong PV gradient at the transition from tropospheric ($PV_{330K} < 2$ PVU) to stratospheric air ($PV_{330K} > 2$ PVU). This strong gradient of PV results from the intersection with a break of the tropopause that runs parallel to the jet stream. It was shown that Rossby waves propagate along this strong PV-gradient band (Schwierz et al. 2004) which explains the collocation of the jet stream. A maximum in the gradient of PV on isentropic surfaces represents a maximum in the jet stream flow. Figure 2.4(b) shows the typically southward extending PV streamers ($PV_{330K} > 2$ PVU) which are associated with upper-level troughs. The southward excursion of stratospheric air becomes important if these positive PV anomalies interact with surface baroclinic zones and lead to the formation of extratropical cyclones (see earlier discussion in section 2.2.1). Conversely, upper-level ridges (e.g. over the Atlantic) are characterized by low tropospheric PV values as the tropopause is located comparatively high. Rossby wave breaking leads to a strong deformation of the PV field on isentropes and stratospheric (tropospheric) air with high (low) PV values elongates equatorward (poleward) (e.g. Berrisford et al. 2007). Rossby wave breakings can form blocking anticyclones (e.g. Pelly and Hoskins 2003) as it is the case over Europe with
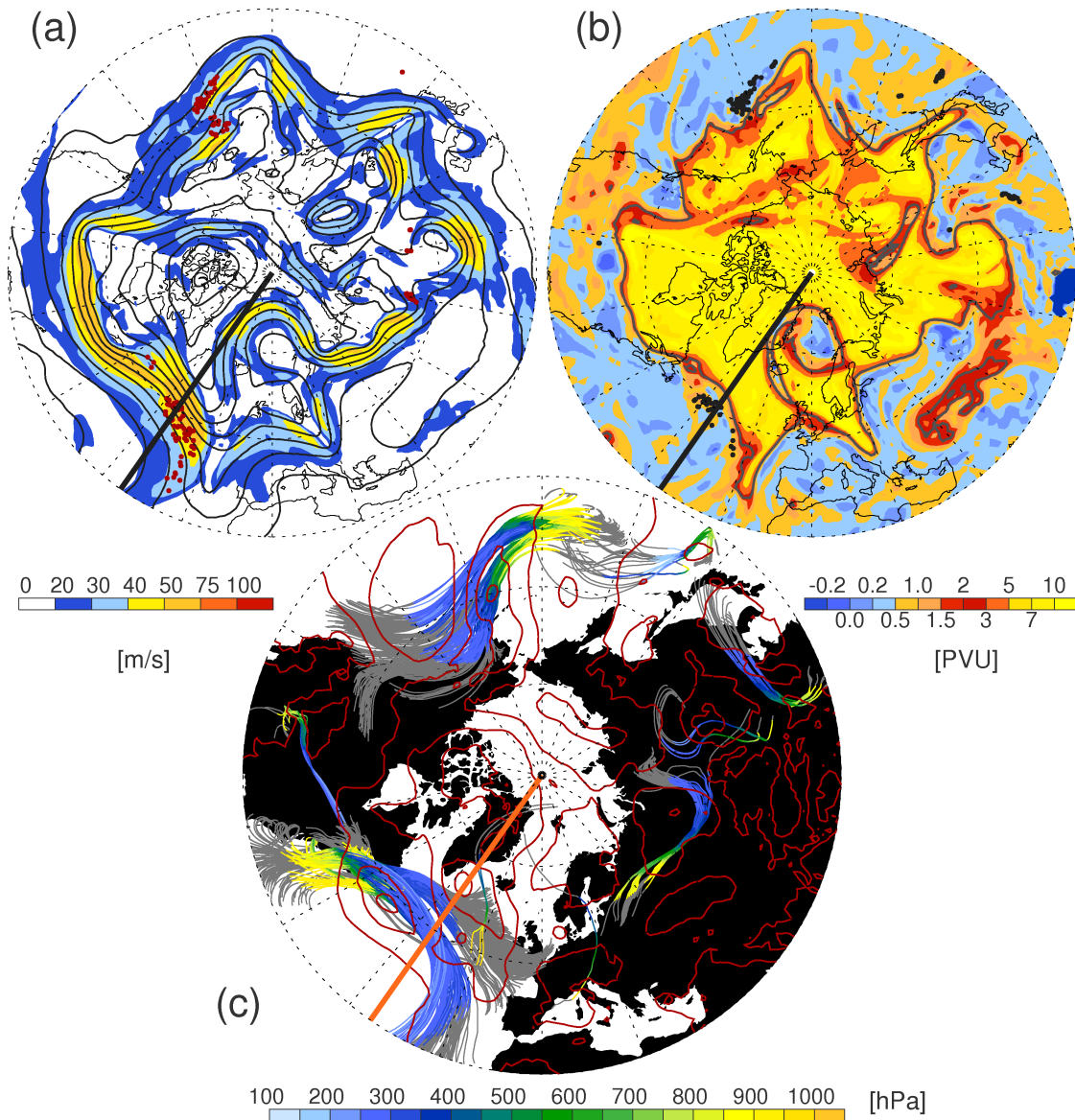
Figure 2.4: WCB and synoptic maps (ECMWF analyses) of the northern hemisphere at 12 UTC 8 September 2008: (a) 300 hPa Geopotential height (black contours, $\Delta Z_{300hPa} = 100$m), horizontal wind speed (colour shaded areas, m s^{-1}). (b) PV on the 330 K isentropic surface (colour shaded areas) with 2 PVU contour line in black. (c) Trajectories that ascend by more than 600 hPa from 00 UTC 7 September to 00 UTC 9 September (coloured in dependence of pressure along the trajectory). The respective WCB trajectories are extended forward and backward by 24 hours (grey lines). The red contour lines indicate the sea level pressure (Δp = 4 hPa). Location of WCB trajectories at 12 UTC 8 September are indicated when located in (a) ±25 hPa (red dots) and (b) ±5 K (black dots). Meridional lines at 35°W in (a), (b) and (c) indicate location of the cross section in Figure 2.5.

low PV values linked to a distinct upper-level ridge over the Norwegian Sea east of Greenland.

As mentioned earlier, PV is conserved in purely adiabatic flow. However, cross-isentropic transport in the WCB raises air from lower levels toward the tropopause.

Trajectories were calculated from all model grid points in the northern hemisphere to identify WCBs that affect the upper-level flow in the present case. Those ascending by more than 600 hPa in 48 hours are considered to be WCB trajectories. The calculation started already at 00 UTC 7 September to study the location at upper-levels 36-48 hours later when the WCB reaches the outflow stage. For a detailed description of the trajectory calculation see section 3.2.2. Figure 2.4(c) shows the WCB trajectories with colour-coded pressure information along the 48 hour ascent. Additionally, the pathways one day before and after the WCB ascent are indicated by the grey lines to get an impression where the conveyor belt originates at low levels and where the airmass turns to in the upper troposphere.

Two major WCBs can be observed that feature the typical coherent poleward and eastward ascent from the boundary layer at the North American east coast and over the central Pacific Ocean. The extended pathways (grey lines in Figure 2.4(c)) show that the airmasses in the inflow of the WCB are transported from southerly direction during the 24 hours before the ascent. After the rapid ascent to ∼300 hPa the parcels disperse horizontally in the anticyclonic outflow. The strong winds at upper-levels transport the airmass rapidly eastwards and depending on the position relative to the jet stream parcels move in different directions. In contrast to the highly idealized WCB concept, the observed WCBs consist of two main branches (Figure 2.4(c)) each with a slightly different ascent and outflow location. Figure 2.4(c) also shows the mean sea level pressure at 12 UTC 8 September 2008 (36 hours after the WCB started). Both WCBs are close to a distinct surface cyclone (at 165°W/50°N and 50°W/50°N) that has developed during the time of the ascent and moved northeastward (not shown). Fitting well with the conceptual model of baroclinic instability both surface cyclones are located on the leading edge of the upper-level trough and positive PV anomaly, respectively. Note that the WCB trajectories are shown for one specific initialization time step which does not exclude that airmasses ascended before and after that time. For example the small WCB features over Asia might represent early or late phases of WCB evolutions.

After 36 hours (time of the synoptic charts in Figure 2.4) the WCB parcels have already reached the upper troposphere. Figure 2.4(a) and (b) show the positions of WCB parcels (red and black dots) that are located within ±25 hPa of the 300 hPa surface and ±5 K above and below the 330 K isentropic surface, respectively. For the Atlantic WCB mainly parcels in the southerly branch which reaches higher altitudes (Figure 2.4(c)) are marked on the anticyclonic side of jet stream on the rear side of a downstream trough at ∼20°W. The location on the anticyclonic side of the jet stream explains the subsequent transport to southerly latitudes. Over the Pacific the jet stream at 300 hPa is less strong and divided into two maxima. The outflow

of the two WCB branches is found in the inflow of the northerly and the outflow of the southerly jet. Both WCBs show the outflow to be positioned in the troposphere with correspondingly low PV values. Consequently, this corroborates the fact that WCBs generate low PV values and can have considerable impact on the upper-level flow, e.g. for the building of upper-level ridges.

Figure 2.5 shows a vertical cross section at a longitude of 35°W which intersects the strong jet stream over the Atlantic Ocean (see Figure 2.4(a)) to determine the location of the WCB trajectories relative to the isentropes, the distribution of PV and the jet stream. The cross section from 30° to 90°N crosses Greenland which is indicated by the model topography between 66° and 84°N (white area in Figure 2.5). The potential temperature isolines indicate the horizontal north-south temperature gradient at the polar front in the midlatitudes (50° to 60°N) that extents up to 300 hPa. As a consequence of the thermal wind relation the jet stream with a wind speed maximum of $\sim$70 m s^{-1} at 53°N and 220 hPa is observed above the horizontal temperature gradient.
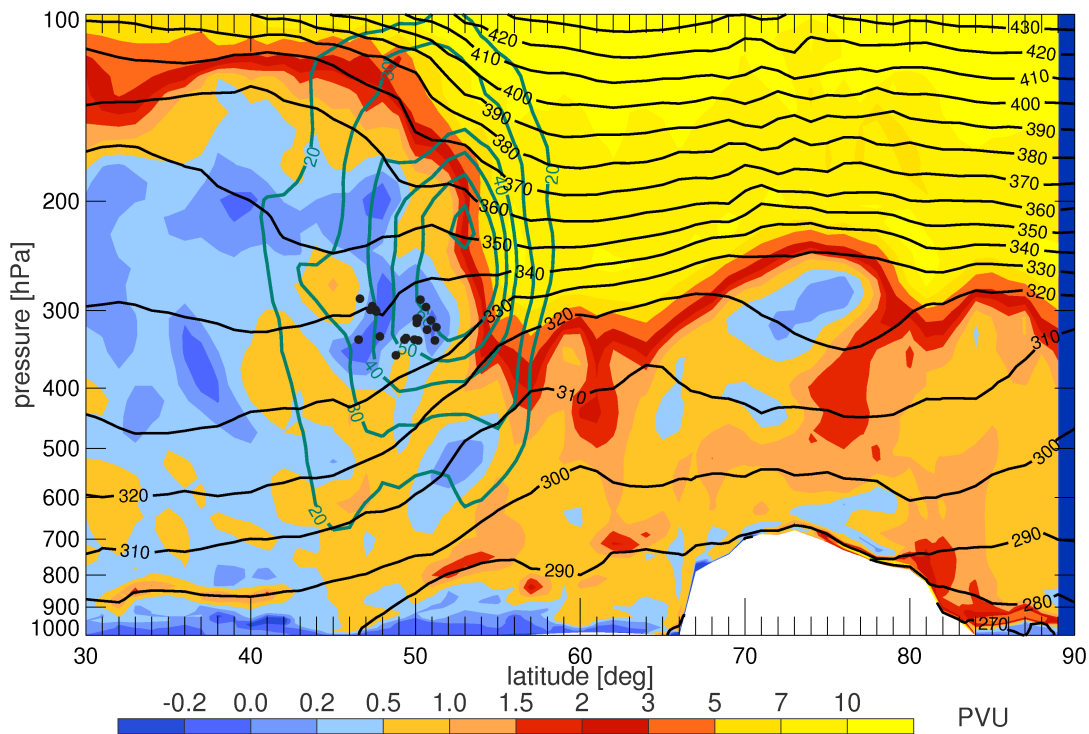

Figure 2.5: Meridional cross section at 35°W based on the ECMWF analysis at 12 UTC 8 September 2008: PV (colour shaded areas, PVU), isentropes (black contour lines, K) and zonal wind speed (green contour lines, m s^{-1}). Location of WCB trajectories intersecting the cross section (black dots).

The transition to the stratosphere is marked by a strong PV gradient resulting from the increased static stability (see increased density of isentropes). The dynamic tropopause (2 PVU isosurface) is located at about 130 hPa, south of the jet

stream and at about 300 hPa, to the north. At the jet stream the tropopause is strongly tilted and a part of the poleward ascending isentropes (320-370 K) crosses the tropopause (also known as "middleworld isentropes", see Hoskins (1991)). On these isentropes (see e.g. 330 K chart in Figure 2.4(c)) a strong gradient of PV is found at the jet stream (Schwierz et al. 2004). Grams et al. (2011) show that the low PV in the WCB outflow strengthens the isentropic PV gradient and for this reason also the strength of the jet stream. A purely adiabatic northward transport would result in a lifting of air along the respective isentrope and explains upward motion on the leading edge of troughs. Conversely, on the rear side of the upper-level lows stratospheric air is transported southward and downward along strongly tilted isentropes and forms tropopause folds (e.g. Flentje et al. 2005).

In the troposphere the PV values are low and show a minimum on the anticyclonic part of the jet stream between 200 and 300 hPa. Figure 2.5 depicts the WCB locations in the upper-tropospheric outflow located within this area of anomalously low PV some degrees south of the tropopause and the maximum wind speeds (compare Figure 2.3). The Atlantic WCB trajectories start at ∼305 K and gain about 30 K of potential temperature by latent heating which enables the air to reach the 300 hPa level. It becomes clear from following the 310 K isentrope in Figure 2.5 from south to north that WCB air parcels would not reach such high altitudes in a purely adiabatic northward transport.

2.2.3   Exemplary WCB trajectories

The thermodynamic properties of WCB airstreams are influenced by diabatic processes which transfer heat between ascending air parcels and their environment, particularly radiation and mixing. Additionally, latent heat release due to phase changes of water vapour is an internal source of heat that is supplied to the air parcels if saturation occurs. Basically, latent heat release is adiabatic and reversible as long as the formed liquid water and ice remains in the air parcel and eventually removes heat by evaporation or sublimation. Since typically large amounts of rain are formed in ascending WCB air masses, phase changes of water in WCBs are considered to be diabatic irreversible processes. Beside the release of latent heat, radiation and mixing processes can influence the evolution of moisture and temperature along WCB trajectories. In extratropical cyclones wind-shear induced turbulence or convection can cause mixing between different air masses. To distinguish between the different diabatic processes and to explore their relevance for the WCB evolution several important variables that characterize the humidity and temperature of the WCB air parcels can be examined along trajectories.

A decrease in specific humidity q, i.e. the mass of water vapour relative to the mass of humid air, indicates either condensation or deposition of water vapour to liquid water or ice depending on the temperature. In an unsaturated environment q is a conserved quantity. Conversely, relative humidity RH is non-conservative and depends strongly on temperature and moisture of an air parcel. RH gives an indication whether saturation occurs along trajectories.

The temperature evolution in a WCB is coupled with diabatic processes. The temperature of an unsaturated ascending air parcel approximately decreases with the dry adiabatic lapse rate of $\Gamma_d = \partial T/\partial z = -g/c_p \approx -9.8 \text{ K km}^{-1}$ where $g = 9.8 \text{ m s}^{-1}$ is the gravitational acceleration and $c_p = 1005 \text{ J kg}^{-1} \text{ K}^{-1}$ is the specific heat of dry air at constant pressure. As soon as the air saturates, heat is transferred to the ascending parcel and it cools at a lapse rate that is less than Γ_d due to the latent heat release that warms the air parcel. The resulting moist adiabatic lapse rate Γ_s depends on temperature and pressure and typically ranges between -4 and $-7°\text{C km}^{-1}$. Additionally, temperature gives information about the kind of phase change that can be expected. Below $0°\text{C}$ the phase transitions from or to the solid phase (e.g. freezing, depositional growth of snow) may also impact the lapse rate.

An important quantity to reveal whether an air parcel experiences diabatic warming or cooling is the potential temperature

$$\theta = T \left(\frac{p_0}{p} \right)^{\frac{R_d}{c_p}} \tag{2.6}$$

which is the temperature of an air parcel that is dry-adiabatically brought to a reference level $p_0 = 1000 \text{ hPa}$. $R_d = 287 \text{ J kg}^{-1} \text{ K}^{-1}$ is the specific gas constant of dry air. Changes in θ are indicative for either phase changes or radiation and mixing processes as θ is only a conserved quantity away from diabatic processes. Contrary, the equivalent potential temperature

$$\theta_E \cong \theta \exp \left(\frac{L_v m_s}{c_p T_{LCL}} \right) \tag{2.7}$$

(e.g. Holton 2004) is additionally conserved in saturated environment and therefore changes in θ_e along the trajectory indicate an impact of surface fluxes, mixing or radiative processes. θ_e is the temperature of an air parcel which is lifted dry-adiabatically until saturation is reached, then moist-adiabatically until all water vapour condensed and rained out and then brought dry-adiabatically to $p_0 = 1000$ hPa. $L_v \approx 2.4 \times 10^6 \text{ J kg}^{-1}$ is the latent heat of vaporisation and $m_s = q_s/(1 - q_s)$

is the saturation mixing ratio. Note that L_v slightly depends on temperature which needs to be taken into account for accurate calculations of θ_e. T_{LCL} is the temperature at the altitude where the air parcel saturates.

To discuss the role of the different diabatic processes during the ascent a subset of the Atlantic WCB, shown in Figure 2.4, is analysed. Figure 2.6(a) shows these trajectories between 00 UTC 6 September and 00 UTC 12 September 2008. Figure 2.6(b) to (f) show the distribution of q, RH, T, θ, θ_e in dependence of pressure for the WCB ascending period between 00 UTC 7 September and 00 UTC 9 September 2008. Mean values of the quantities for given pressure intervals are shown in Table 2.1.
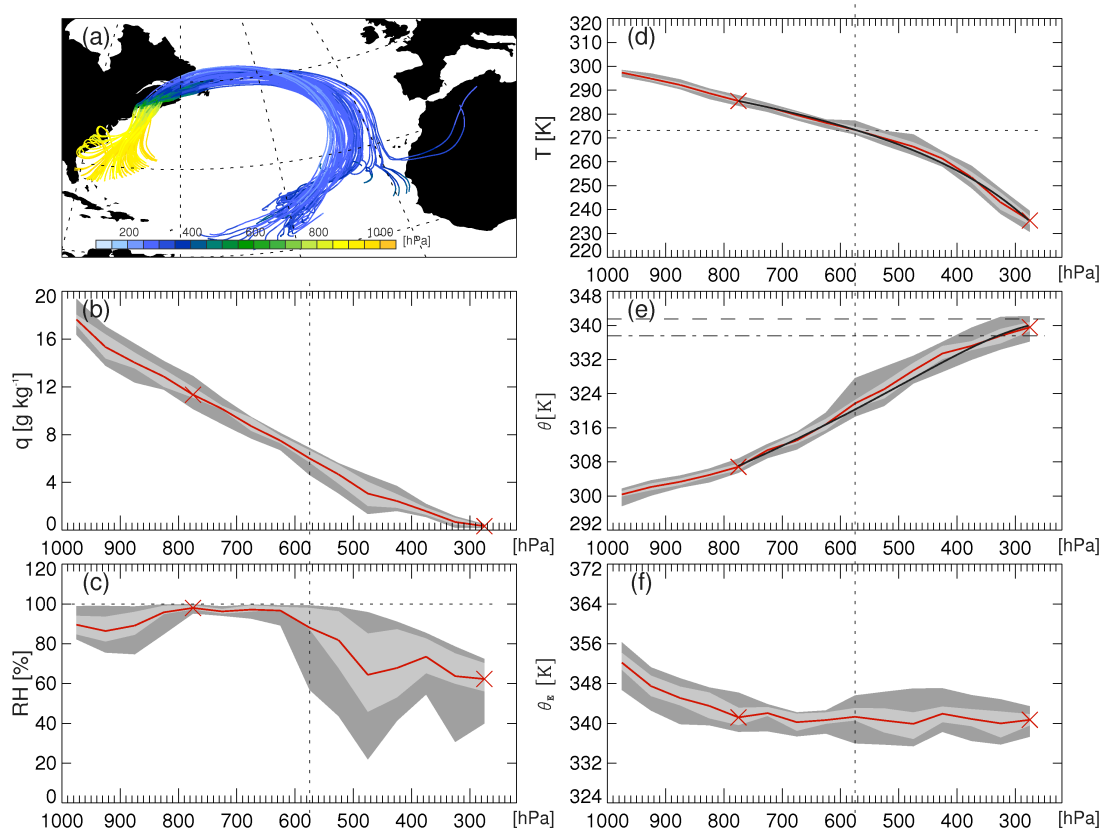

Figure 2.6: (a) Subset of WCB trajectories shown in Figure 2.4 from 00 UTC 6 September to 00 UTC 12 September 2008 (coloured in dependence of pressure along the trajectory). Distribution of (b) q, (c) RH, (d) T, (e) θ and (f) θ_e during the WCB ascent between 00 UTC 7 September and 00 UTC 9 September 2008. Grey shaded areas indicate the 5–95 % (dark grey) and 25–75 % (light grey) percentiles and red lines show the mean over all trajectories. Red crosses represent the saturation and the upper most point of the mean trajectory. Black lines in (d) and (e) represent the evolution of T and θ of an air parcel that is lifted moist-adiabatically to the upper-most point (see description in the text). Vertical black dotted lines indicate the 0°C pressure level. The horizontal dotted line in (c) indicates RH=100 %. The dashed and dash-dotted line in (e) shows θ_e calculated with different formulas (see description in the text).

In the ascending airstream q decreases from $\sim$17 g kg^{-1} to $\sim$0.3 g kg^{-1} (Figure 2.6(b)) which shows that nearly all the available water vapour passes over to

the liquid and solid phase. RH initially varies between 80 and 100 % and increases with the vertical decrease of temperature (Figure 2.6(c)). Most WCB parcels reach saturation between 900 and 850 hPa ($\overline{RH} = 98$ %). Above 600 hPa, RH is reduced and shows a higher variability.

During the ascent the mean temperature decreases by $\Delta\overline{T} = 62$ K (Figure 2.6(d) and Table 2.1). The lowest vertical temperature gradient occurs between 850 and 550 hPa ($\Gamma_s \approx$ -5°C km^{-1}) where the highest moisture decrease Δq suggests the maximum latent heat release. Above, temperature falls at a higher rate ($\Gamma_s \approx$ -8°C km^{-1}) due to the reduced latent heat release. θ increases vertically by $\Delta\overline{\theta} = 39.4$ K from 339.9 K in the inflow to 300.5 K in the outflow of the WCB (Figure 2.6(e)). The increase is strongest in the saturated layer with maximum Δq. In the boundary layer, the decrease of θ_e suggests entrainment of dry air (Figure 2.6(f)). Above, θ_e remains constant at ~340.5 K which implies that latent heat release is the primary diabatic process that controls the evolution of T and θ during the WCB ascent. However, the increasing variability of θ_e above 600 hPa and the concurrent decrease of RH suggest that mixing processes affect the WCB.

p [hPa]	RH [%]	q [g kg^{-1}]	T [K]	Θ [K]	θ_e [K]
1000 - 950	89.6	17.6	297.4	300.4	352.2
950 - 900	86.4	15.3	294.8	302.1	347.5
900 - 850	89.1	14.0	292.2	303.3	345.1
850 - 800	95.8	12.9	288.7	304.9	343.5
800 - 750	98.0	11.3	285.5	306.8	341.2
750 - 700	96.3	10.2	282.9	310.8	342.1
700 - 650	97.2	8.7	279.6	313.0	340.2
650 - 600	96.7	7.5	276.3	316.8	340.7
600 - 550	88.1	6.0	273.4	321.7	341.3
550 - 500	81.8	4.7	269.9	325.1	340.6
500 - 450	64.4	3.1	266.4	329.4	339.9
450 - 400	67.8	2.4	261.3	333.4	341.9
400 - 350	73.5	1.6	253.5	335.2	340.9
350 - 300	63.7	0.7	243.0	337.6	340.0
300 - 250	62.3	0.3	235.4	339.6	340.7

Table 2.1: Mean values in 50 hPa pressure intervals for the WCB trajectories ascending between 00 UTC 7 September and 00 UTC 9 September 2008 as shown in Figure 2.6(a).

Figure 2.6(b) shows that on average the specific humidity decreases to 0.3 g kg^{-1} and the potential temperature increases to 339.9 K. As mentioned, θ_e is the potential temperature of an air parcel that loses all of its moisture by condensation which is approximately the case for the WCB trajectories. Using $e^x = 1 + x + x^2/2! + ... + x^n/n!$, equation 2.7 can be approximated as $\theta_E \cong \theta \left(1 + \frac{L_v m_s}{c_p T_{LCL}}\right)$. This leads to $\theta_e = \theta + 30.6$ K $= 337.6$ K if values are taken at the altitude where the mean trajectory nearly saturates (see Table 2.1 at ~775 hPa: $m_s = 11.4$ g kg^{-1}, $T_{LCL} = 285.5$ K,

$\theta = 307$ K). Hence, the condensation of 11.4 g kg^{-1} of water vapour increases the potential temperature by 30.6 K. This rough estimate of θ_e (dash-dotted line in Figure 2.6(e)) is lower than the potential temperature reached by the trajectory. A more accurate calculation of θ_e using the formula of Bolton (1980) yields 341.5 K (dashed line in Figure 2.6(e)). The proximity of the calculated θ_e-values and the potential temperature that is reached by the mean trajectory indicates that latent heat release is important for the evolution of T in WCBs. This is confirmed by the calculation of the T and θ evolution of an air parcel that is lifted moist-adiabatically from the saturation point to the upper most point of the trajectory. Therefore the moist adiabatic temperature gradient Γ_s is calculated as a function of T and p (Iribarne and Godson 1981)

$$\Gamma_s \cong \Gamma_d \frac{1 + \frac{\epsilon L_v e_s}{R_d T p}}{1 + \frac{\epsilon^2 L_v^2 e_s}{c_p R_d T^2 p}} \tag{2.8}$$

where e_s is the saturation water vapour pressure at a temperature T and $\epsilon = 0.622$. The black curves in Figure 2.6(d) and (e) illustrate the temperature and θ evolution of the lifted parcel iteratively calculated after equation 2.8 and 2.6. The calculated temperature fits well with the values of the mean trajectory and the parcel reaches a potential temperature of 340.6 K. The mean over all trajectories at 275 hPa is $\overline{\theta} = 339.6$ K. The best agreement is found in the layer with highest RH-values. Above, slight differences occur in connection with mixing processes. A slight influence can also be attributed to a somewhat higher release of latent heat due to depositional vapour-ice processes (L$_d$ = 2.83×10^6 J kg^{-1}) which are not considered in equation 2.8 and occur at temperatures below 0°C. To summarize, the release of latent heat dominates the various diabatic processes during the WCB ascent. This confirms Joos and Wernli (2011) who showed that condensation in the lower and warmer part of the WCB and depositional growth of snow in the upper part are the dominating microphysical processes which reproduce the total change in θ along WCB trajectories. The presented case suggests that other diabatic processes such as mixing play a secondary role for the temperature evolution during the ascent in the WCB.

To analyse whether diabatic processes play a role in the WCB outflow, Figure 2.7 shows time-series of the above described variables over the whole time period from 00 UTC 6 September to 00 UTC 12 September 2008 (144 h). The time period from 24 h to 72 h formed the basis for the pressure averaging that was necessary for Figure 2.6 and Table 2.1. Figure 2.7(a) shows that the WCB reaches its highest altitude after ∼60 h and subsequently decreases in altitude. During the descent q remains constant at ∼0.3 g kg^{-1} which implies a constant amount of water vapour,

i.e. no phase changes take place. During the descent RH decreases (Figure 2.7(c)) which can be explained by an increase of T (Figure 2.7(d)). Figure 2.6(a) indicates a southward transport of the WCB at upper levels. Due to the fact that the adiabats are sloped downward towards the south (see Figure 2.5) one might expect the WCB trajectories to decrease in altitude. In a purely adiabatic descent T would increase due to compression of the air parcel whereas θ is conserved in adiabatic flow. However, Figure 2.7(e) shows that θ and θ_e decrease by $\sim$5 K in 4 days which suggests that heat is removed from the air parcel. As q remains constant the decrease of θ is most likely due to radiative cooling.
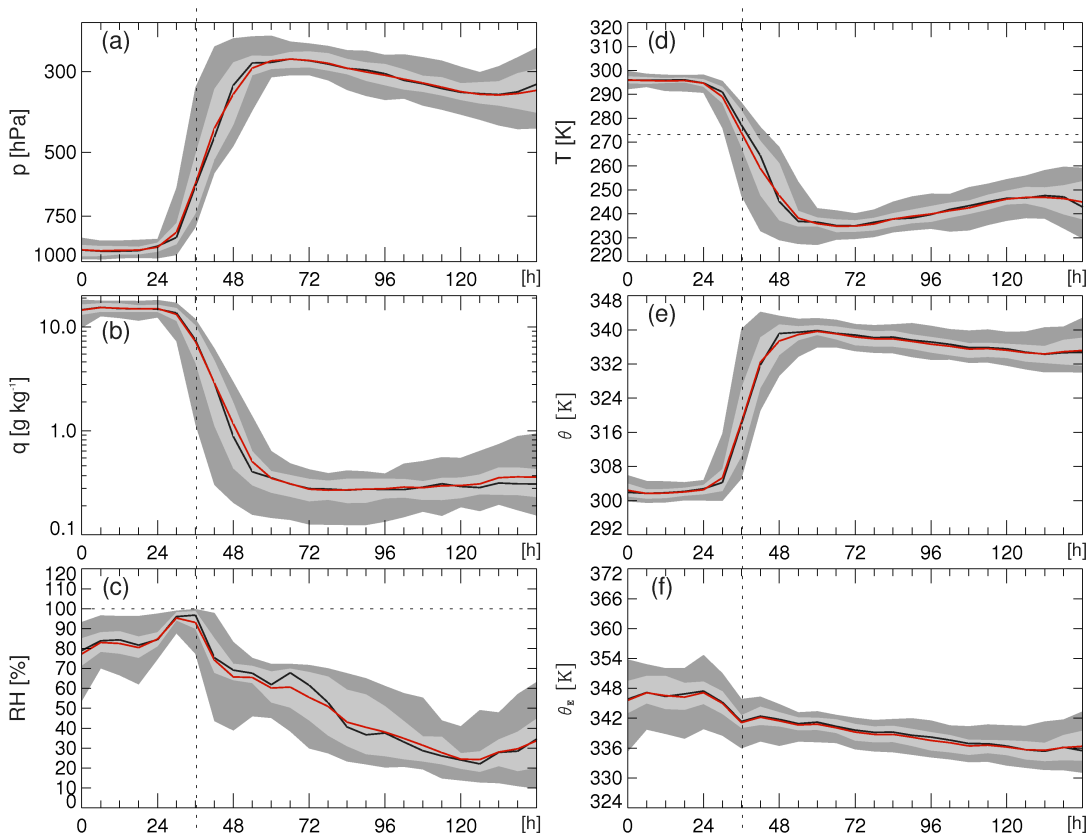

Figure 2.7: Time series of WCB trajectories shown in Figure 2.6(a) from 00 UTC 6 September to 00 UTC 12 September 2008 of (a) p (b) q, (c) RH, (d) T, (e) θ and (f) θ_e. Grey shaded areas indicate the 5–95 % (dark grey) and 25–75 % (light grey) percentiles. Red lines show the mean, black lines the median over all trajectories. Vertical black dotted lines indicate the time when 0°C is reached. The horizontal dotted line in (c) indicates RH=100 %. The dotted line in (d) shows T=0°C.

Note that this exemplary case only represents one summer-time WCB case which starts at high temperatures and high moisture contents. Additionally, it shows a transport at relatively low latitudes. It can be assumed that other WCBs exist showing a different transport depending on geographical location and season.

2.2.4   Climatological importance

Eckhardt et al. (2004) presented a global climatology of WCBs. They calculated trajectories over a time period of 15 years based on ECWMF re-analysis data. Trajectories were started on the entire globe and they extracted WCBs in a slightly more restrictive way than presented in section 2.2.2. A threshold for eastward (10° in longitude), northward (5° in latitude) and upward (60 % of the climatological tropopause height) was assumed in their analysis. They found that the typical time scale of a WCB ascent from the BL to the upper troposphere is 48 hours. The subsequent anticyclonic outflow located in the downstream ridge is characterized by a slight descent. In the northern hemisphere, the origin of WCBs lies in the mean between 25°N and 45°N with two maxima of occurrence east of North America and east of Asia. However, WCBs can originate over the entire North Atlantic and the Mediterranean (Ziv et al. 2010). Eckhardt et al. (2004) showed that WCBs are more frequent during winter and the air parcels travel faster after being lifted in the WCB which can be explained by the increased cyclone activity and stronger jet streams. Additionally, they quantified mean values of pressure, moisture and potential temperature at the start point of p(0 h) = 940 hPa, q(0 h) = 7 to 12 g kg^{-1} and θ(0 h) = 297 K. Almost the entire moisture is converted to precipitation along the ascending trajectories. The latent heat release due to water vapour condensation leads to a climatological mean potential temperature increase of 15-22 K. It was found that the Pacific WCBs start at higher moisture contents (q(0 h) = 12 g kg^{-1}) and, therefore, possess higher latent energy which caused a higher latent heat release ($\Delta\theta$ = 22 K) and a larger vertical displacement (Δp = 580 hPa in 48 h) than the WCBs appearing over the Atlantic (q(0 h) = 10 g kg^{-1}, $\Delta\theta$ = 17 K, Δp = 545 hPa). Their study also showed an expected good agreement of the WCBs with the occurrence of extratropical cyclones but also with high level clouds outside the tropics.

As the climatology showed, the transport of moisture to upper-levels influences the distribution of cirrus clouds. Spichtinger et al. (2005) showed that WCBs represent an effective mechanism to generate ice supersaturated regions in which cirrus clouds frequently occur. Hence, the WCB outflow regions represent a favourable environment for the formation of climate-relevant aircraft-induced contrail cirrus. WCBs are effective in ventilating pollutants from the boundary layer to the free troposphere (Sinclair et al. 2008) and, additionally, transport by means of WCBs is a primary mechanism for distributing pollution over long distances and to the upper troposphere (e.g. Stohl and Trickl 1999). As also shown by Eckhardt et al. (2004) a fraction of ∼6 % of the WCB trajectories reaches the stratosphere. In this way, the

WCB can affect the composition on the upper tropospheric and lower stratospheric chemistry and also the radiative forcing (Roiger et al. 2011).

Therefore, various airborne measurements during previous field campaigns focused on the chemical composition of WCBs (Bethan et al. 1998; Vaughan et al. 2003) and on the long range transport of dust and trace-gases (Cooper et al. 2002, 2004).

2.3 Summary

Driven by the differential heating of polar and tropical regions the global atmospheric circulation transports energy poleward to reduce the energy imbalance. In the midlatitudes, westerly winds caused by the sharp thermal contrast separating airmasses of subtropical and polar origin at the polar front are prevailing. Instabilities in the large-scale jet stream flow pattern result in the formation of baroclinic waves with an embedded sequence of cyclones and anticyclones. The fronts associated with extratropical cyclones are responsible for most of the poleward and upward transport and moisture in the midlatitudes. It is obvious that the WCB which is the main poleward oriented air stream in a cyclone is a key component of the overall atmospheric meridional energy transport.

The foregoing sections described the major airstreams in an extratropical cyclone and the outstanding relevance of the cross-isentropic transport within WCBs for the evolution and intensification of extratropical cyclones by means of the diabatic generation of PV. Diabatic processes contribute also to the distribution of the upper-level PV. The generation of negative PV anomalies in the WCB outflow region on the anticyclonic side of the jet can influence the upper-level wind field and the downstream weather evolution.

Apparently, the WCB couples the upper-level dynamics to low- and mid-level moist processes. Analysis and forecast errors in the framework of a WCB can therefore have particularly strong impact on forecast skill by altering the upper-level dynamics. Current NWP models are known to insufficiently reproduce the latent heating processes which are caused by different microphysical processes like e.g. condensation, freezing or evaporation (Brennan et al. 2008). However, poor forecasts do not always result from errors in the model physics. It is also critical that the model analysis accurately represents the supply with moisture to the WCB. Moister air in the inflow releases more latent heat which implies a higher $\Delta\theta$ which is consistent with a stronger lifting.

Chapter 3

Methodology

The foregoing chapters demonstrated the need for exact observations of humidity to unveil shortcomings in the model analysis and forecast fields and to study their origin and impact on NWP. An investigation of the humidity and wind structure in WCB inflow regions with state-of-the-art remote sensing lidar instruments is presented for the first time in this thesis. This thesis combines the lidar observations with data of the global NWP model of the ECMWF to enable a thorough analysis and identification of the WCB in the measured humidity profiles. Figure 3.1 gives an overview of the different methods that are applied to investigate the WCB inflow region and that are explained in the following sections.
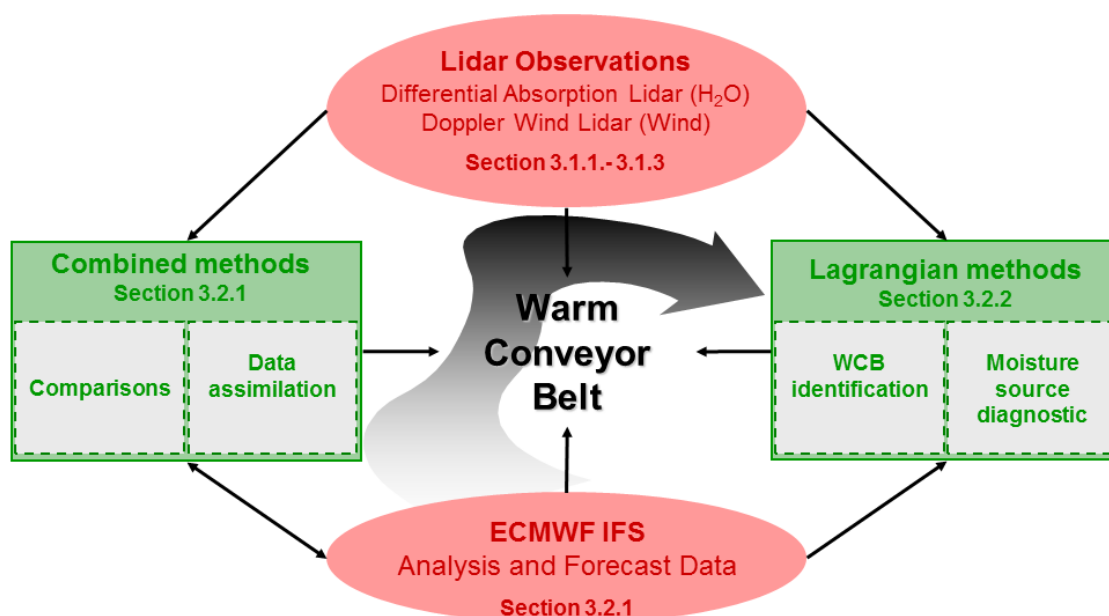

Figure 3.1: Overview of the applied methods to investigate the WCB with observational data and NWP simulations.

Section 3.1 gives an overview of the physical principles of lidar (section 3.1.1) and information about the DLR airborne DIAL (section 3.1.2) and the DWL (sec-

tion 3.1.3). Forecast and analysis data of the ECMWF IFS are explained in section 3.2.1 which also illustrates how the data can be combined with lidar observations to study the humidity structure in the WCB inflow and its representation by the ECMWF IFS. Additionally, the basic ideas of data assimilation to use DIAL humidity data within the IFS are provided. Wind data from a NWP model further constitute the basis for Lagrangian methods which are discussed in section 3.2.2 and are an essential component to identify and investigate WCBs. General information about trajectory calculations is given and a moisture source diagnostic is presented which is used to study the transport history of the observed humidity. Section 3.3 presents the lidar data pool that is taken into account for possible WCB observations. Additionally, the identification of WCB observations based on trajectory diagnostics is subject of section 3.3.1. Section 3.3.2 comprises a preliminary assessment of the suitability of the detected missions with regard to the defined scientific objectives of this thesis.

3.1   Lidar observations

3.1.1   Light detection and ranging

Atmospheric profiling with lidar came up when first laser (Light Amplification by Stimulated Emission of Radiation) systems were developed in the 1960s. Over the past decade they evolved to key techniques in the field of active remote sensing. Lidar measurements in the atmosphere rely on the interaction of light with constituents of the atmosphere. Figure 3.2 illustrates the basic principle: A laser transmits short
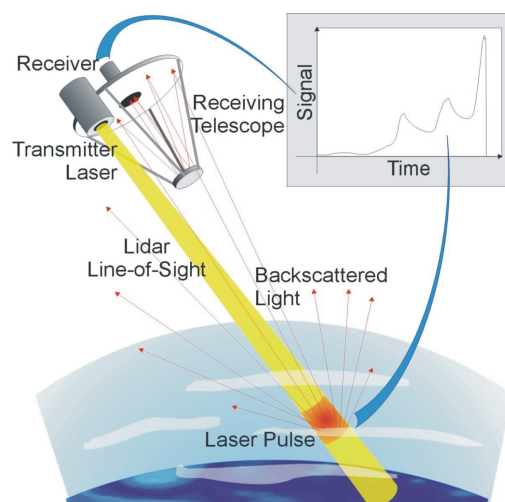

Figure 3.2: Principle of lidar observations in the atmosphere. Courtesy of ESA.

pulses with high energy into the atmosphere which are scattered by air molecules

and aerosols. A telescope observes the intensity of the backscattered light in the line of sight (LOS) direction. By recording the time delay between the emitted and received signal the distance to the scatterer can be calculated by using the speed of light. The intensity of the backscattered light which depends on the wavelength as well as the size and concentration of the scatterers is described by the lidar equation (Wandinger 2005):

$$P(r) = \underbrace{P_0 \frac{c\tau}{2} A\eta}_{K} \; \underbrace{\frac{O(r)}{r^2}}_{G(r)} \; \beta(r,\lambda) \; \underbrace{exp\left[-2\int_0^r \alpha(r,\lambda)\,dr\right]}_{T(r,\lambda)}. \qquad (3.1)$$

K summarizes properties of the lidar system, namely the average power of a single laser pulse P_0, the pulse length τ, the area of the receiver telescope A and overall system efficiency η. The geometric factor $G(r)$ consists of the quadratic decrease of the signal intensity with distance (r^{-2}) and the overlap function $O(r)$ that describes signal weakening in the near field influenced by the system design of receiver and transmitter.

The first atmospheric parameter that influences the received signal is the backscatter coefficient $\beta(r,\lambda)$ that describes how much light is scattered back towards the lidar, i.e. the scattering at the wavelength λ under a scattering angle of 180°. Both scattering by air molecules (Rayleigh scattering) and by aerosol and cloud particles (Mie scattering) contribute to the total backscatter coefficient. Molecular scattering decreases with height as it mainly depends on air density, in contrast to the highly variable particles. The last term in the lidar equation given by the Lambert-Beer-Bouger law relates the atmospheric transmission $T(r,\lambda)$ to the total extinction coefficient $\alpha(r,\lambda)$ and describes the fraction of the signal that is lost between lidar and scattering volume. The integral in the exponent of $T(r,\lambda)$ is called optical depth. The extinction coefficient accounts for absorption and scattering of light by molecules and particles. The factor 2 results from the two-way transmission path of the lidar pulse.

K and $G(r)$ are known factors determined by the lidar system, while $\beta(r,\lambda)$ and $T(r,\lambda)$ represent the unknown terms dependent on the actual atmospheric properties. There exists a variety of lidar techniques which use different interaction processes of the emitted laser pulses with the atmospheric constituents to measure trace gases, aerosols as well as atmospheric parameters like temperature, humidity and wind. Equation 3.1 represents the basis for all lidar techniques.

3.1.2   Differential absorption lidar

Methodology

The DIAL technique can be applied to remotely measure atmospheric humidity with high accuracy and spatial resolution. The DIAL principle is based on the different absorption of at least two spectrally narrow laser pulses transmitted into the atmosphere (Bösenberg 2005). The online wavelength is tuned to the centre of a molecular water vapour absorption line. The offline wavelength positioned at a non-absorbing wavelength serves as a reference. As the absorption lines are spectrally narrow, on- and offline wavelengths can be set close enough so that one can assume that the backscatter coefficient is equal for both wavelengths ($\beta_{on}(r, \lambda) \cong \beta_{off}(r, \lambda)$). Furthermore, the extinction terms of all other molecular or particulate species are almost equal for both wavelengths which leads to the following formulation of the extinction coefficient

$$\alpha(r, \lambda) = N(r)\,\sigma_{abs}(r, \lambda),\tag{3.2}$$

where $N(r)$ is the water vapour molecule number density and $\sigma_{abs}(r, \lambda)$ the absorption cross section of water vapour. Based on the lidar equation (equation 3.1) and the mentioned assumptions in terms of extinction, the logarithm of the ratio between the received online and offline signals (P_{on}/P_{off}) leads to the following expression:

$$ln\left(\frac{P_{on}(r)}{P_{off}(r)}\right) = ln\left(\frac{P_{0,on}}{P_{0,off}}\right) - 2\int_0^r (\alpha(r, \lambda_{on}) - \alpha(r, \lambda_{off}))\,dr.\tag{3.3}$$

A substitution of $\alpha_{on} - \alpha_{off}$ with $N(\sigma_{on,abs} - \sigma_{off,abs}) = N\Delta\sigma$ and a following differentiation with respect to r can be solved for N and results in the DIAL-equation (Bösenberg 2005):

$$N(r) = \frac{1}{2\Delta\sigma}\left[\frac{d}{dr}ln\left(\frac{P_{off}(r)}{P_{on}(r)}\right)\right].\tag{3.4}$$

The outstanding advantage of this measurement technique is that it goes without any calibration for the common case that the system parameters are identical for both wavelengths. To calculate the water vapour number density only the effective absorption cross section $\Delta\sigma$ is required which is obtained from spectroscopic laboratory measurements. The specific humidity q can be calculated from N with the use of the ideal gas law.

$$q(r) = \frac{R_{air}}{R_{H_2O}}\frac{N(r)\,k\,T(r)}{p(r)},\tag{3.5}$$

where R_{air} is the specific gas constant of dry air, R_{H_2O} is the specific gas constant of

water vapour and k is the Boltzmann constant. The calculation of q needs vertical information of temperature T and pressure p which are not measured by the DIAL. This information is also important for the calculation of the effective absorption cross section $\Delta\sigma$ and is normally obtained from vertical profiles of the standard atmosphere or from NWP models. However, the uncertainty of the mixing ratio caused by temperature and pressure uncertainties is small and less than a few per cent (Kiemle 2008).

The absorption spectrum of water vapour is characterized by a variety of differently strong absorption lines. The theoretical considerations require a careful selection of the absorption line strength. Enough return towards the lidar as well as a sufficient extinction on the way through the atmosphere has to be ensured. As the extinction is proportional to the number concentration of the trace gas (see equation 3.2), the line strength has to be adapted to the prevailing water vapour concentrations. A too weak absorption line would result in small differences between online and offline signal which causes undesirable noise effects. A too strong absorption line would result in a quick attenuation of the online wavelength which limits the profiling range. Generally, the airborne application of a DIAL to observe humidity from above has the advantage that the concentrations increase towards the ground so that the extinction increases as well. This enlarges the profiling range. However, it is difficult to measure the whole range of water vapour concentrations that varies in the order of 4 magnitudes from the lower stratosphere to the ground. Therefore, most recent airborne systems use a combination of multiple wavelengths centred at differently strong absorption lines to assure sensitivity in all altitudes.

Airborne DIAL WALES

Since 1985 the lidar department at the DLR Institut für Physik der Atmosphäre has developed and applied airborne water vapour DIALs. The airborne application offers high mobility to study various phenomena in different parts of the atmosphere. From 1990 a two-wavelength DIAL was operated on-board the DLR research aircraft Falcon. In 2007 a new multi-wavelength DIAL, the WALES (Water vapour Lidar Experiment in Space, Wirth et al. 2009) demonstrator was operated for the first time. The system consists of two transmitters, each based on an injection-seeded optical parametric oscillator (OPO) pumped by the second harmonic of a Q-switched, diode-pumped single-mode Nd:YAG laser. The WALES laser system is capable of emitting light at up to 4 wavelengths (3 online, 1 offline) simultaneously in the water vapour absorption band around 935 nm. Three different neighbouring and temperature insensitive absorption lines are selected to achieve sensitivity in

the whole range of tropospheric water vapour concentrations. The positions of the absorption lines are shown in Figure 3.3. The weak absorption line is individually selected depending on the meteorological situation and location of the flight, i.e. the water vapour concentrations in the arctic, midlatitude and tropical boundary layer. The entire profile is composed of the three, partly overlapping line contributions.
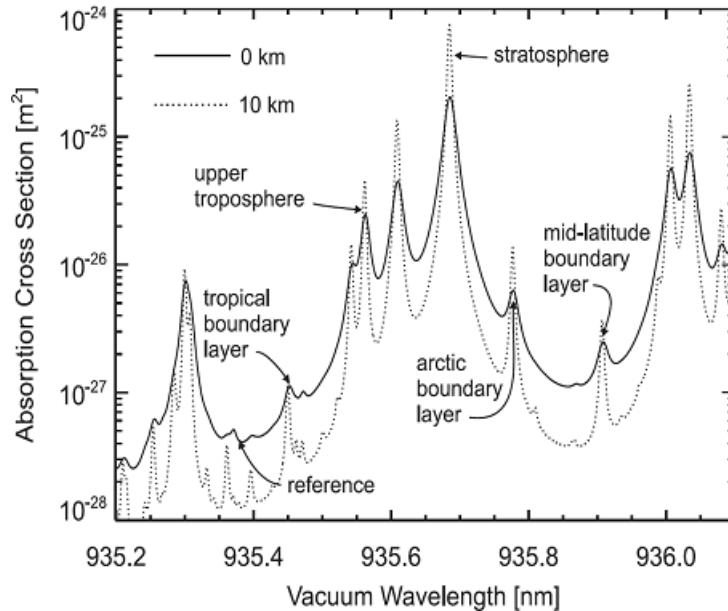

Figure 3.3: H_2O-absorption lines used for the WALES demonstrator (from Wirth et al. 2009). Absorption cross section for sea level conditions (solid line) and at 10 km altitude (dashed line) using the US-standard atmosphere.

The average output energy is 40 mJ at a repetition rate of 200 Hz (50 Hz per wavelength quadruple, see Table 3.1). A detailed technical description of the system is given by Wirth et al. (2009).

Like other remote sensing instruments, the DIAL technique has error sources which have to be considered in the data evaluation. Both, systematic and statistical errors influence the measurement accuracy (Poberaj et al. 2002). Systematic errors result for example from uncertainties in the spectral characteristics of the absorption lines, the limited stability of the online wavelength position, the residual temperature dependency of the absorption cross-section, and the spectral purity of the laser radiation. A spectral purity of 100 % would characterise an ideal laser, that emits all its radiation at the specified wavelength. Real lasers deviate from this.

In the data processing, the line-broadening Rayleigh-Doppler effect of scattering by air molecules is corrected with an algorithm based on the backscatter measurements. Instrumental noise causing random fluctuations of the signals can be reduced effectively by horizontal and vertical averaging. Therefore, all on- and offline signals are averaged over a certain time interval before the humidity is calculated. For this

study, a horizontal resolution of 60 s ($\sim$12 km) and a vertical range resolution of 350 m are used.

In recent years, the DIAL instruments demonstrated their applicability to measure water vapour at high spatial and temporal resolution (e.g. Bhawar et al. 2011; Kiemle et al. 2008). In this thesis, data from the field experiments ETReC in 2007 and T-PARC in 2008 are shown. During the ETReC flights only three out of four possible wavelengths could be used for water vapour measurements. Additionally, the online diagnostics to assess the spectral properties of the laser system were not yet fully implemented. Therefore the spectral purity of the laser which varies along the flight results in a systematic uncertainty that was estimated by processing the data and assuming two different spectral purities (see Schäfler et al. 2010). Comparisons with radiosondes and dropsondes during ETReC revealed that 90 % spectral purity was a reasonable value (C. Kiemle and M. Wirth, pers. comm., 2009). Hence, this value was used as reference and compared with data processed with a hypothetical spectral purity of 99 %. Relative differences between the two data sets larger than 15 % led to a removal of the respective data points. During T-PARC the WALES demonstrator was fully functional and operated at four wavelengths. The spectral properties of the lasers were recorded online during the flight and used in the data evaluation to correct systematic uncertainties.

	DIAL	**DWL**
Transmitter type	OPO	Diode Laser
Wavelength (nm)	935	2022
Pulse energy (mJ)	40	1.5
PRF (Hz)	200	500
Average power (W)	8	0.75
Detection principle	direct	heterodyne
Detection type	APD	PIN diode
Telescope diameter (cm)	48	10

Table 3.1: Technical characteristics of the DIAL WALES and the DWL

Additionally, atmospheric backscatter measurements were conducted at a wavelength of 1064 nm, generated by the pump-laser, to calculate the backscatter ratio (BSR) which is the ratio of the total (particle and molecular) backscatter coefficient and the molecular backscatter coefficient. The resolution of the BSR is 15 m vertically and 10 s ($\sim$2 km) horizontally with typical values ranging from 1 in a very clean atmosphere to 100 in regions with high aerosol load.

3.1.3 Doppler wind lidar

Methodology

A DWL takes advantage of the Doppler effect which describes the change in frequency and wavelength for the case that the receiver moves relative to the source of the radiation (Werner 2005). A detection of the change of frequency permits the calculation of the velocity of the source relative to the receiver. However, only the velocity component towards the receiver, called the LOS velocity can be determined from the frequency shift. The difficulty of an atmospheric application is the fact that the moving air parcel has to emit radiation, which can be achieved by illumination with laser light. The illuminated backscattering volume receives a wave transmitted by the lidar which is reemitted or backscattered towards the lidar. The received frequency is

$$f = f_0 + \Delta f = f_0 \left(1 + 2\frac{v}{c}\right). \tag{3.6}$$

f_0 is the transmitter frequency and v the relative velocity in LOS. Since typical atmospheric wind speeds only amount to a fraction of the velocity of light the frequency shifts are small and can only be measured with heterodyne detection. A transmitted frequency with $f_0 = 1.5 \times 10^{14}$ s^{-1} ($\lambda_0 = 2 \times 10^{-6}$ m) experiences a frequency shift that is not larger than 1×10^6 s^{-1} (1 MHz) and therefore very difficult to measure. Although the return decreases with larger wavelengths, the DWL wavelengths usually lie in the infrared to increase the aerosol return compared to the molecular return. Hence, DWL wind measurements benefit from the presence of aerosols.

DLR Doppler wind lidar

The DWL consists of a diode-pumped continuous wave master laser and a pulsed slave laser. The master laser has double importance for the system, namely for the injection seeding, i.e. the frequency locking of the slave laser as well as for the usage as a local oscillator. The backscattered signal is mixed with the local oscillator on the detector. The resulting difference frequency Δf is amplified and digitized. The slave laser transmits pulses at a wavelength of 2022 nm at a pulse repetition frequency (PRF) of 500 Hz (see Table 3.1).

The system uses the velocity azimuth display (VAD) technique to retrieve a three-dimensional wind vector beneath the aircraft from LOS measurements. A scanner performs a conical step-and-stare scan under an off-nadir angle of 20 degrees. For the measurements, the scanner stops at 24 positions over a 360 degree scan (every 15°). The conical scan pattern is transformed to a cycloid pattern as the

aircraft moves. A wind vector is calculated from three LOS velocities separated by 120°. In this way, 8 different wind vectors are obtained per scanner revolution. First, a mean vector is calculated and then all 24 LOS velocities are compared to the mean. Outliers are eliminated and new mean vectors are calculated repetitively until all remaining LOS velocities are situated inside a tolerance range of ± 1 m s^{-1}. The time for one scanner revolution ($\sim$30 s) and the aircraft velocity determine the horizontal resolution of the resulting wind profiles which is about 5 to 10 km, depending on the distance from the aircraft. The vertical resolution of 100 m is limited by the pulse length of 400 ns. The PRF of 500 Hz leads to an accumulation of 500 or 1000 shots per scanner position which is important for reducing noise. Detailed information about the DWL system, the calculation of the wind vector and an error assessment can be found in Weissmann et al. (2005).

3.2 Model data

In this thesis, data from the ECMWF IFS is used to complement the lidar data. In the following the model data and their application in the different methods (Figure 3.1) are explained. General information about the ECMWF IFS, comparisons of model data with lidar observations and the use of DIAL data in the IFS data assimilation system are given in section 3.2.1. Additionally, gridded model data is used to calculate kinematic trajectories. Section 3.2.2 gives an overview of the trajectory calculations and their application to identify WCBs.

3.2.1 ECMWF IFS

General information

The ECMWF's IFS is a spectral primitive equation model. The spectral representation of the prognostic meteorological variables determines the horizontal resolution. For the analysis of the WCB missions in this study the IFS version with a truncation at wavenumber 799 is used which corresponds to a grid point spacing of approximately 25 km in the horizontal (Persson and Grazzini 2007). This model version (T799) became operational in 2006 and was replaced by a T1279 version in 2010, which is equivalent to a horizontal resolution of 16 km. In the vertical, the IFS offers 91 vertical model levels which are irregularly distributed from 1000 to 0.1 hPa. The vertical resolution is highest close to the ground with the highest model level density. The hybrid model levels are terrain-following at lower levels and smoothly change into horizontal, isobaric surfaces in the upper troposphere.

Operationally, the ECMWF deterministic forecast model runs twice a day at 00 and 12 UTC. Supplementary analyses are generated at 06 and 18 UTC which corresponds to a 6-hourly temporal resolution of the analyses. Forecast fields are stored 3-hourly up to +144 h (+6 d) and subsequently 6-hourly up to +240 h (+10 d). Meteorological fields are archived on model levels and discrete pressure levels. For the purposes of this study the spectral data is interpolated to a regular lat-lon grid (0.25° resolution). Model level data is used to compare with the lidar data whereas pressure level data is retrieved to analyse the meteorological situation.

Special forecast experiments

The analyses of the ECMWF operational IFS at 00, 06, 12 and 18 UTC provide a somewhat inadequate temporal resolution to resolve the often occurring noneven (nonlinear) evolutions in the atmosphere like e.g., at fronts in midlatitude weather systems. To compare with the lidar data, an enhanced temporal resolution in the model fields is desired that can be attained by using forecast fields at the intermediate time steps. With the operational forecasts at +3 h (03, 15 UTC) and +9 h (09, 21 UTC) a 3-hourly temporal resolution can be achieved.

Special short-term forecast runs are initialized and conducted to further enhance the temporal resolution and to keep the forecast error as low as possible. The interactive interface prepIFS of the ECMWF is used to prepare research experiments and remotely access the ECMWF computing facilities. Forecasts are started four times a day from the operational analyses using the operational T799L91 model setup. PrepIFS allows changing the operational data output from every three hour to every hour. The combination of operational analyses and the four daily forecast with 1-hourly data output up to +5 h results in a uniform 1-hourly temporal resolution of the ECMWF model fields. In this, way a more accurate representation of areas with strong spatial humidity and wind gradients and a confidential comparability with the model output is guaranteed.

Interpolation methods of model data

As mentioned the comparison of model data with lidar observations in the inflow of a WCB is a key method to assess the structure of the inflow and its representation in the model fields. This technique has been repeatedly used to qualitatively and quantitatively analyse lidar observations of wind and water vapour (e.g. Flentje et al. 2007; Schäfler et al. 2010).

In a first step a bilinear interpolation from the surrounding grid points is per-

formed to project model information onto the position of lidar profiles. This is done for every model level. In a second step the resulting profile needs to be interpolated vertically towards the lidar resolution. The interpolation is performed for every one-hourly output time step of the model fields. Finally, a linear interpolation in time is performed towards the time of the respective lidar profile based on the two temporally closest model profiles. This underlines the need of maximum temporal resolutions of the gridded model fields to be able to compare with the lidar data consisting of temporally continuous profiles. The resulting model profiles possess the same spatial and temporal resolution and can be used to calculate differences or to display other meteorological variables along the observed cross section. For example the absolute difference (in g kg^{-1}) of observed and simulated specific humidity is defined in as

$$\Delta q_{ABS} = q_{ECMWF} - q_{OBS} \tag{3.7}$$

and the relative difference (in %) as

$$\Delta q_{REL} = \frac{q_{ECMWF} - q_{OBS}}{\frac{1}{2}\left(q_{ECMWF} + q_{OBS}\right)} * 100\ \%. \tag{3.8}$$

The relative differences are particularly suitable to account for the typically small differences in the upper troposphere. In this thesis, the main interest is put on differences in the lower troposphere and therefore mostly absolute differences are illustrated. Positive values of Δq_{ABS} and Δq_{REL} mean higher moisture values in the IFS forecast and analysis fields which is equivalent to an overestimation of the simulated moisture, whereas negative values indicate a dry bias in the model (see e.g. Schäfler et al. 2010).

Data assimilation and verification

Optimal initial conditions play a crucial role for the forecast accuracy of NWP models. A large amount of conventional (weather station, radiosonde, aircraft) and non-conventional (active and passive remote sensing instruments on-board different satellites) data are used to create the analysis. The ECMWF IFS uses a 4-dimensional variational (4DVAR) data assimilation system (Rabier et al. 2000) with a 12-hourly data assimilation window.

Recent studies have shown that the assimilation of lidar data is a successful method to improve model analyses. Weissmann and Cardinali (2007) and Weissmann et al. (2011) show a beneficial impact of DWL observations on the analysis. Harnisch et al. (2011) show that the analysis error can be reduced by assimilating DIAL moisture profiles in the ECMWF model. In this thesis, analysis fields pro-

vided by Harnisch et al. (2011), with an improved moisture analysis, are used to study the impact of moisture analysis errors on the WCB forecast and the relation to the evolution of an associated midlatitude cyclone.

Two data assimilation experiments were performed using all operationally available observations, the control experiment (CTRL) and another experiment (DIAL) that additionally uses the DIAL observations. The resulting two analyses provide physically consistent initial conditions that only differ by the additional use of the DIAL observations. A comparison of both analyses with the observations can be used to show how the assimilation changed the moisture in the WCB inflow. A reduction of the analysis error corresponds to a positive impact of the assimilation of the DIAL data.

Two forecasts are initialized from the different analyses (CTRL and DIAL). By comparing both runs the influence of humidity errors in the inflow region of a WCB can be assessed. Differences of predicted variables in both experiments (e.g. moisture, geopotential height or PV) can be traced back to modified initial conditions. Additionally, the forecasts are verified against the operational ECMWF analysis fields to estimate the impact of the DIAL data assimilation.

Different measures are used to quantify the forecast impact and to investigate its spatial and temporal evolution. The vertically averaged PV (between 900 and 500 hPa) impact is calculated as the difference of the forecast error in the DIAL and the CTRL forecast to see the impact of the changed moisture on the PV structure of the cyclone:

$$IM_{PV} = \left| \overline{PV}_{DIAL,550-900hPa} - \overline{PV}_{AN,550-900hPa} \right| - \\ \left| \overline{PV}_{CTRL,550-900hPa} - \overline{PV}_{AN,550-900hPa} \right| \tag{3.9}$$

The first term on the right hand side is equivalent to the averaged PV error in the DIAL forecast whereas the second is the error in the CTRL forecast. Negative values imply reduced errors due to the assimilation of the DIAL data. The same forecast quality measure is calculated for the geopotential height at different pressure levels.

A total kinetic energy norm is used to assess how and when WCB analysis errors affect the dynamical structure of the associated cyclone. Therefore the impact on the kinetic energy [m^2 s^{-2}] of the storm is calculated as:

$$IM_{KE} = \frac{1}{2} \left[(u_{DIAL} - u_{AN})^2 + (v_{DIAL} - v_{AN})^2 \right] - \\ \frac{1}{2} \left[(u_{CTRL} - u_{AN})^2 + (v_{CTRL} - v_{AN})^2 \right] \tag{3.10}$$

The first term on the right hand side is the kinetic energy of the deviations between

DIAL and analysis, the second between CTRL and analysis. The total impact is calculated as the sum of the impact at 850, 500 and 250 hPa to include contributions of the low, middle and upper troposphere.

3.2.2   Lagrangian trajectories

General remarks on trajectories

Beside the Eulerian view on meteorological fields at fixed time steps, this thesis uses several Lagrangian diagnostics to identify and analyse WCBs. In a Lagrangian framework trajectories describe the pathway of air parcels through space and time. For the calculation of trajectories information about the atmospheric motion is needed. Kinematic trajectories as calculated in this thesis need three-dimensional winds. Therefore, gridded wind fields of NWP models are used. The Lagrangian perspective of tracing air parcels in time and space offers a broad applicability in atmospheric sciences. Atmospheric trajectories are used to study various processes in atmospheric dynamics, boundary layer meteorology and also in atmospheric chemistry.

Stohl (1998) lists error sources that contribute to the accuracy of trajectories. The largest error source is the inaccuracy of the driving wind fields. Errors in the analysis as well as the temporally increasing forecast errors can affect the overall error. Stohl et al. (2001) showed that deviations resulting from uncertainties in the wind fields are higher than differences in the trajectories from different models. It also has to be mentioned that the spatial resolution of the wind fields influence the accuracy as only motions at resolved scales (with wave lengths of two grid lengths or more, Persson and Grazzini (2007)) can be traced. Below the smallest resolved scales of motion winds, e.g. arising from the convective parameterization scheme, contribute to the overall wind vector which apparently represents a possible error source, especially in convective areas. Additionally, a spatial and temporal interpolation is required to project wind information of the gridded data towards the trajectory position. Therefore an adequate spatial and temporal resolution of the wind fields is needed. It was found that it is most effective to limit the error by increasing both resolutions. Stohl (1998) also stated that the effect of interpolation errors may vary in different flow regimes. Additionally, errors result from truncation in the numerical solution of the trajectory equation and from the treatment of the vertical velocity.

The trajectory model LAGRANTO (Larangian Analysis Tool, Wernli and Davies (1997)) is used to calculate kinematic trajectories. It consists of several FORTRAN routines and Shell Scripts to calculate either forward or backward trajectories. In

this study, LAGRANTO is driven by the above described gridded wind fields of the ECMWF IFS available on 91 model levels and at a spatial resolution of 0.25°. Stohl (1998) point out that the use of wind fields every three hours instead of the 6-hourly analysis fields significantly improved the trajectory calculation. According to this, short term forecasts are used to enhance the temporal resolution to 3 hours for most trajectory applications that require the highest accuracy. Additionally to the position of the air parcel, LAGRANTO provides information about the evolution of selected meteorological parameters (e.g. pressure, temperature, potential temperature, and PV) along the trajectory.

Since hourly fields from short term forecasts are available over a 6-day period for the case study presented in chapter 4, a sensitivity study on the influence of the temporal resolution of the driving wind fields on the trajectory calculations could be performed, as presented in Appendix A. It is shown that the detection of WCB is relatively insensitive to the temporal resolution of the wind fields. Especially low level air masses that are lifted subsequently to the observation are consistently identified.

Identification of WCBs

As already mentioned in section 2.2.2, WCB airmasses can efficiently be identified with the aid of trajectory calculations and the application of objective selection criteria (Wernli and Davies 1997; Eckhardt et al. 2004). Eckhardt et al. (2004) identified air parcels to be involved in a WCB if the respective trajectory ascends by more than 60 % of the tropopause height and if it moves more than in 10° longitude to the east and more than 5° in latitude to the north. They show that the pressure decreases by approximately 550 hPa during the first 2 days for this criterion. Many studies therefore use an adjusted selection criterion based only on the pressure decrease whereby most often a threshold of 600 hPa is chosen (e.g. Spichtinger et al. 2005; Grams et al. 2011). For the purpose of this study, either the 600 hPa criterion is chosen to identify WCB trajectories or, for the case that the structure of the inflow is investigated, the respective maximum ascent is quantified for trajectories with ascents exceeding 400 hPa. Commonly LAGRANTO is used to calculate trajectories in a larger area with starting points that equal the location of the model grid points specified by their longitude, latitude and pressure. Then the desired criteria can be applied to select a certain subset, e.g. the WCB trajectories.

A main aim of this thesis is to associate the airborne lidar observations with WCBs. In section 3.3 a method to find intersections of WCB trajectories starting on model grid points in the northern hemisphere is described that allows a pre-selection

of promising missions. For the most promising flights a refined diagnostic is developed that uses LAGRANTO to calculate trajectories from positions that are located apart from the NWP grid which is the case for the lidar observations. In this way, one trajectory per observation point along the two-dimensional lidar cross section is calculated. The continuously measured lidar profiles provide a starting time for the trajectory calculation which does not correspond to the time of the underlying wind fields. Usually, the internal integration time step of LAGRANTO is 30 minutes. When a starting time is chosen that demands a higher temporal resolution, the time step of the calculation adapts automatically. If trajectories are started at a resolution of 1 minute, then the computational time increases significantly as the internal time step is set to one minute. Therefore, a starting frequency of 15 minutes is chosen as a reasonable compromise between computational costs and accuracy in the definition of the starting position. For the duration of the particular flight profiles within a time interval of 15 minutes are combined and start at a centred and uniform time. LAGRANTO uses pressure as vertical coordinate, whereas the location of the lidar observations in the vertical is defined by the geometrical height. For that reason the pressure from the ECMWF analyses was interpolated to every observation point as described above. Finally, a forward and a backward calculation are combined to a trajectory which is investigated for the maximum decrease in pressure over 48 hours to analyse the vertical displacement and the evolution phase of the observed WCB.

Moisture uptake diagnostics

As described in the introduction, one of the main aims is to study the transport characteristic of the observed WCB airmasses. Therefore trajectories backward in time from the observation are investigated with respect to the transport mechanisms. Based on these trajectories a moisture source diagnostic that was introduced by Sodemann et al. (2008) and Pfahl and Wernli (2008), is applied to analyse the location and time of the moisture uptake. In essence, the technique uses material changes of specific humidity along trajectories to quantitatively diagnose moisture uptakes due to surface evaporation. The analysis aims at clarifying whether enhanced humidity deviations can be attributed to an increased moisture uptake and/or to distinct uptake regions. The moisture change in a time interval along the trajectory is

$$\frac{\Delta q}{\Delta t} = E - P \tag{3.11}$$

and depends on evaporation E and precipitation P that influence the parcel during

the transport (Stohl and James 2004). If $\Delta q/\Delta t > 0$ then evaporation dominates and the parcel takes up humidity and moistens. The moisture uptake analysis is typically performed at 6 h time intervals and the moisture change is calculated as

$$\Delta q(t) = q(\vec{x}(t)) - q(\vec{x}(t - 6h)). \qquad (3.12)$$

$\vec{x}(t)$ denotes the parcel position at the time t (Sodemann et al. 2008). The uptake of moisture crucially depends on sub-grid scale processes which are parameterized by turbulent humidity fluxes. Only uptakes within the PBL are taken into account to ensure that the uptake is surface driven. In this way, processes that lead to the increase of moisture above the PBL, e.g. convection or evaporation from rain droplets, are excluded. A moisture source location is calculated from an average trajectory position during the six hour interval to be able to distinguish oceanic uptakes (mixing of advected air with moisture evaporated from sea surface) and continental uptakes (evaporation from the soil and transpiration from plants). In the course of a multi-day trajectory several evaporation and precipitation events can change the moisture content of the air parcel. To account for a reduced contribution of uptakes to the moisture content at the end of the trajectory (point of observation) as a consequence of a subsequent precipitation event, a relative contribution of all moisture sources along a trajectory is assigned (Sodemann et al. 2008). If all uptakes are summarized, the extent to what the moisture at the observation points can be explained by uptakes along the trajectories, is calculated (Pfahl and Wernli 2008).

3.3 Identification of WCB missions in lidar data set

As mentioned in the introduction the DLR research aircraft Falcon participated in several international research campaigns during the last years. Table 3.2 gives an overview of the campaigns considered in this study and indicates the number of flights and the respective total flight hours.

About 260 flight hours from 81 research flights during eight research campaigns over the North Atlantic, Europe and the western North Pacific are taken into account. As the main interest of this thesis is the humidity structure in the WCB inflow, all of these missions provide at least DIAL water vapour measurements and some also provide DWL wind observations. Note that during the Convective and Orographically Induced Precipitation Study (COPS) the four-wavelength DIAL was deployed for the first time on-board the Falcon. The actual total lidar observation

Campaign/Year	OBS type	flights	duration	area of operation
IHOP 2002	H_2O	6	16:00	transfer to Oklahoma, US
TROCCINOX 2004	H_2O	2	08:00	transfer to Brazil
SCOUT 2005	H_2O	2	04:00	transfer to Darwin, Australia
COPS / ETReC 2007	H_2O,Wind	15	48:30	SW Germany / SW Europe
IPY-THORPEX 2008	H_2O,Wind	17	60:00	Northern Norway
EUCAARI 2008	H_2O	15	48:30	Central Europe
SAMUM II 2008	H_2O	15	47:00	Cape Verde Islands
T-PARC 2008	H_2O,Wind	9	30:00	Japan, Western Pacific
TOTAL		81	262:00	

Table 3.2: Falcon research campaigns from 2002 to 2008 with a deployment of lidar systems (DIAL and DWL). Note that for IHOP 2002 no aircraft data was available which forms the basis for the calculation of the flight hours. Therefore the time with available lidar data is indicated.

time is slightly shorter compared to the flight duration because the systems work only when flight level is reached. The identification of WCBs in this comprehensive data set consists of three steps that are shown in Figure 3.4 and described in the following. First all missions are checked for the meteorological and geographical location (section 3.3.1). Trajectories are calculated and analysed for intersections with the flights (section 3.3.2). The location of the intersections gives information about the development stage of the observed WCB. Additionally, section 3.3.2 evaluates the identified cases with WCB observations and the ability to study the scientific objectives of this thesis. A detailed analysis of these cases is presented in chapters 4 and 5.
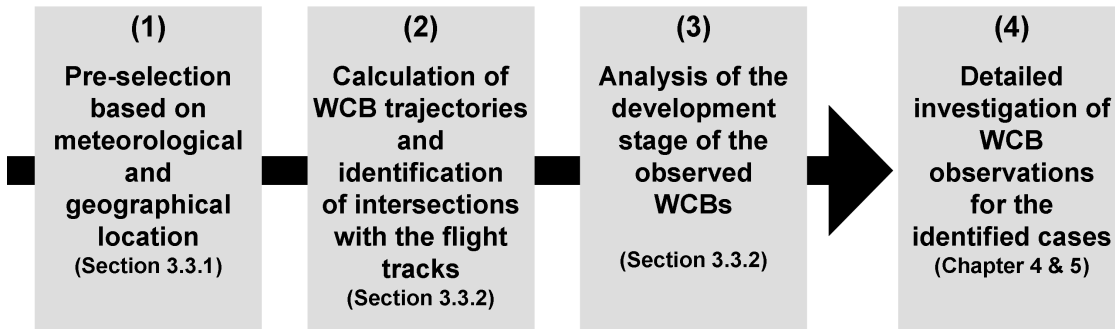
Figure 3.4: Schematic of the WCB identification method.

3.3.1 Pre-selection based on meteorological and geographical location

At first, an evaluation of the geographical location of the respective flight was carried out. The spatial distribution of WCBs, in the climatology of Eckhardt et al. (2004) showed that WCBs predominantly occur in a latitude belt between 20° and

75°N. Missions outside this latitude belt are excluded. Additionally, the flights are checked for the meteorological situation based on analysis weather charts as WCBs are preferably located on the leading edge of developing or amplifying upper-level troughs. Flights in inappropriate geographical regions or during meteorological situations that are unlikely to be associated with a WCB, i.e. in tropical and polar airmasses away from baroclinic zones as well as in high pressure situations, are excluded.

This leads to the following evaluation of the above described missions of the 8 considered field experiments. Figure 3.5(a) and (b) illustrate the geographical location of the research flights (see also Table 3.2). During 6 transfer flights to Oklahoma (Kansas, USA) where the International H2O Project (IHOP_2002, Weckwerth et al. 2004) in 2002 took place (black lines in Figure 3.5(a)) water vapour was observed in the vicinity of the Atlantic wave guide (Flentje et al. 2005). Tropospheric water vapour was probed on the inbound flights from the Tropical Convection, Cirrus and Nitrogen Oxides Experiment (TROCCINOX, Flentje et al. 2007, see dark green lines in Figure 3.5(a)) and the Stratospheric-Climate links with emphasis On the UT/LS (SCOUT) experiment (Vaughan et al. 2008, see orange line in Figure 3.5(a)). Based on the case study by Flentje et al. (2007) there is no evidence that WCB airmasses were probed on the TROCCINOX transfer flights from Brazil to Europe.
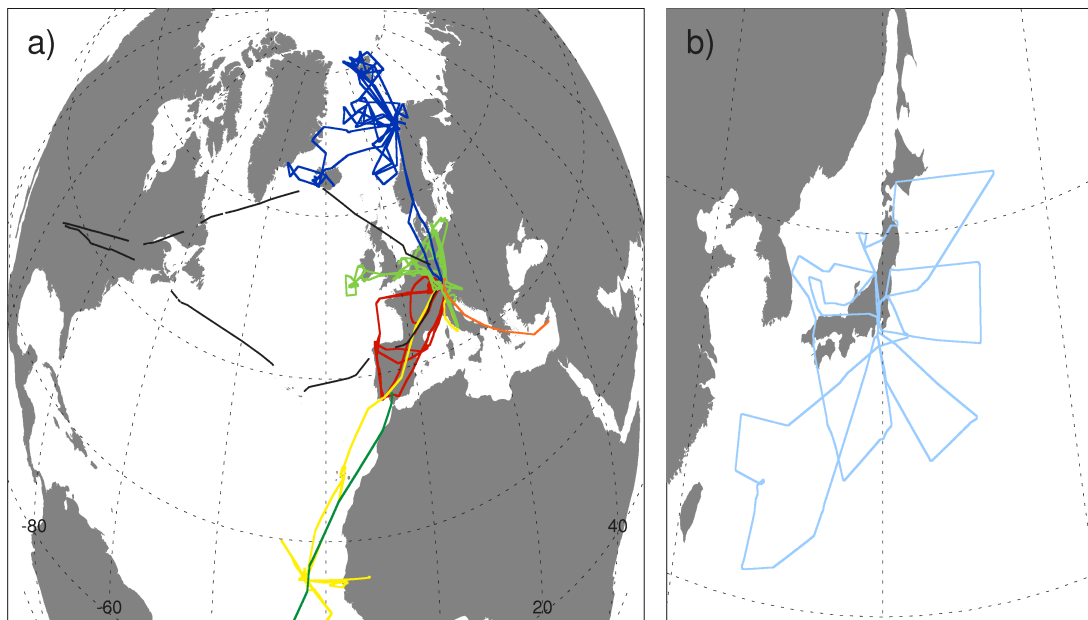
Figure 3.5: Falcon flight tracks of lidar missions considered for the WCB search from 2002 to 2008: (a) IHOP_2002 transfer flights in 2002 (black), TROCCINOX transfer in 2004 (dark green), SCOUT transfer in 2005 (orange), COPS in 2007 (red), IPY-THORPEX (blue), SAMUM 2 (yellow) and EUCAARI (light green) in 2008. (b) T-PARC in 2008 (light blue)

In summer 2007, during COPS (see Wulfmeyer et al. 2008) and ETReC 2007 the DIAL WALES and the DWL performed first collocated measurements over Western Europe (see red lines in Figure 3.5). In addition to the various local flights over southern Germany, elongated flights to upstream regions with airborne observations of the horizontal moisture transport were undertaken during the associated ETReC 2007 campaign (Schäfler et al. 2010).

The IPY-THORPEX campaign which was part of the International Polar Year (IPY) in 2008 aimed at observations of polar lows in the Barents Sea (Wagner et al. 2011, see blue lines in Figure 3.5(a)). Water vapour was also observed during the second Saharan Mineral Dust Experiment (SAMUM-2) when research flights were carried out from the Cape Verde Islands (see yellow lines in Figure 3.5(a)). IPY-THORPEX and SAMUM-2 have been rejected as both campaigns took place in polar and tropical airmasses, respectively, decoupled from the midlatitudes. During the European integrated project on Aerosol Cloud Climate and Air Quality Interactions (EUCAARI) in 2008 in-situ instruments measuring aerosol properties were supported by the DIAL to obtain water vapour and aerosol backscatter information (see light green lines in Figure 3.5(a)). A persistent blocking anticyclone that influenced central Europe made the occurrence of WCBs very unlikely and therefore the EUCAARI data could not be considered. During T-PARC in 2008 the Falcon operated over the western North Pacific to improve the forecast of tropical cyclones (TCs). Additionally, there was emphasis on the interaction of TCs with the midlatitudes (Harnisch and Weissmann 2010; Weissmann et al. 2011). Therefore most of the flights during T-PARC either focused on tropical airmasses or suffered from high cloud coverage which prevented a substantial amount of DIAL observations. However, 9 missions (see light blue lines in Figure 3.5(b)) with DIAL observations were taken into account for the WCB analysis which were also considered in the study by Harnisch et al. (2011) that shows the impact of DIAL observations on the ECMWF forecast skill during T-PARC. This study indicated one promising mission with a positive forecast impact in the midlatitudes.

After the pre-selection with regard to the meteorology and geographical location, the missions of the campaigns IHOP_2002, COPS/ETReC as well as the SCOUT transfer flight that took place in the midlatitudes are considered to be promising for possible WCB intersections. The ensuing Lagrangian diagnostic to search for WCB encounters in this subset of missions is described in the next section.

3.3.2 WCB observations and ability to study the scientific objectives

The aircraft missions that have been selected to search for possible WCB observations comprise approximately 53 flight hours. For these missions, WCBs are identified by analysing ensembles of trajectories calculated with LAGRANTO (for a detailed description of the trajectory calculations see section 3.2.2). Based on 6-hourly ECMWF analyses, trajectories were started every 6 hours during a time period of 6 days (4 days before and one day after the respective mission) at every model grid point below 850 hPa in an area from 120°W to 80°E and 10°N to 90°N. The trajectories with an ascent of more than 600 hPa in 48 hours were identified as WCB trajectories. These trajectories were investigated for intersections with the flight tracks to analyse whether lidar observations were taken in the vicinity of a WCB. Most intersections occurred during IHOP_2002, where 4 of the 6 missions showed WCB crossings. An analysis of the intersection time and altitude with respect to the position in the WCB revealed that most WCB parcels were observed in the upper troposphere several hours after the WCB ascent. During COPS and ETReC 2007, the two missions on 19 July and 1 August 2007 (see Schäfler et al. 2010, for details on this mission) offer WCB intersections.

The mission on 19 July features a considerable amount of observations taken in the lower tropospheric inflow region prior to the ascent of parcels in the WCB. Because these measurements provide key information on the initial moisture field streaming into the WCB, this mission was selected for a detailed case study presented chapter 4. As will be shown later in this thesis a considerable moisture bias in the analysis fields occurred over the Iberian Peninsula which is considered to be a comparatively data dense area. This case study therefore focused on the transport history of the observed airmass and the importance of moisture uptakes for the analysis errors.

A second mission that provides high data density in the inflow of a WCB turned out to be the T-PARC mission on 19 September 2008. Originally, this mission was noticed as it showed an improvement of the forecast of a midlatitude cyclone (Harnisch et al. 2011). As will be shown in chapter 5 the observations between a tropical and midlatitude cyclone probed in large parts the inflow of a WCB. The focus of this case study is to investigate the impact of moisture analysis errors on the physical processes in a WCB and the connection to errors in the forecast of the midlatitude cyclone and the WCB outflow.

Chapter 4

What is the origin of moisture errors in the WCB inflow? - A case study on 19 July 2007

In the following the COPS airborne lidar mission on 19 July 2007 is analysed. After a description of the synoptic situation (section 4.1), the water vapour and wind observations are presented (section 4.2). Section 4.3 depicts the location and structure of the WCB observations before section 4.4 discusses model errors along the cross section. A subsequent analysis (section 4.5) aims at clarifying whether the observed deviations are associated with moisture uptakes in distinct uptake regions. Section 4.6 summarises the contents of this chapter.

4.1   Synoptic overview

The flight on 19 July 2007 from Faro (Portugal) to Oberpfaffenhofen (Germany) took place between 1110 and 1440 UTC (see flight path in Figures 4.1(a) and (d)). After flying northward along the western coastline of Spain the aircraft turned eastward crossing Spain south of the Pyrenees into the Gulf of Lyons before crossing the Alps. Lidar observations of both humidity and wind are available between 1156 and 1314 UTC, i.e. mainly in a west-east oriented curtain along northern Spain (indicated by the solid line in Figure 4.1). The weather situation over Western Europe at that time (12 UTC 19 July, see Figures 4.1(a) and (d)) is characterized by an upper-level trough with its centre located southwest of the UK. Warm and moist air was advected northeastward ahead of the trough as confirmed by the high values of the equivalent potential temperature at 850 hPa ($\sim$1500 m). The flight path crossed this tongue of high θ_e air on the way to the Mediterranean. Over
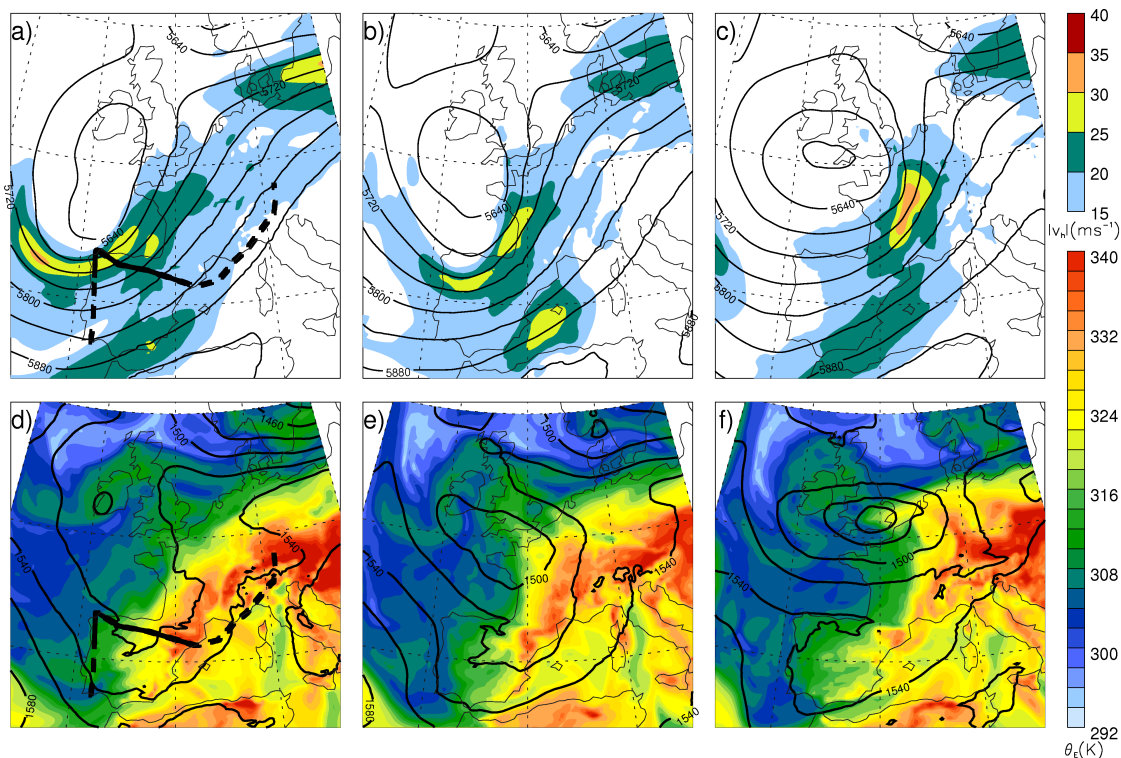
Figure 4.1: ECMWF analysis valid on 12 UTC 19 July (a, d), 00 UTC 20 July (b, e) and 12 UTC 20 July 2007 (c, f). Geopotential height (m, black lines) and horizontal wind speed (m s^{-1}, colour shaded areas) at 500 hPa (a, b and c). Geopotential height (m, black lines) and equivalent potential temperature (K, colour shaded) at 850 hPa (d, e and f). Thick black lines in (a) and (d) show the flight pattern of the DLR Falcon. The solid part indicates the section of collocated lidar measurements.

Galicia, where the aircraft turned eastward, the flight path intersected a jet stream wind maximum at 500 hPa with peak wind speed of about 30 m s^{-1}.

The ECMWF analysis taken 12 hours later depicts a jet stream maximum which is embedded in the large trough (Figure 4.1(b)). The jet streak propagated towards France and cyclogenesis was initiated in the left jet exit region over Brittany. This evolution is visible in the deepening of the geopotential height field at 850 hPa and, especially, in the deformation of the frontal zone (strong θ_e gradient; Figure 4.1(e)). Another 12 hours later, at 12 UTC 20 July, the jet streak is positioned over France (Figure 4.1(c)) and the frontal wave intensified as indicated by a significantly decreased geopotential height at 850 hPa (Figure 4.1(f)). In the course of this development intense convection was triggered by the upper-level anomaly in the unstable airmass over France and southwestern Germany during the night and the following day.

Figure 4.2 shows a composite of the Moderate Resolution Imaging Spectrora-diometer (MODIS) for 19 and 20 July 2007. The satellite imagery at 1150 UTC
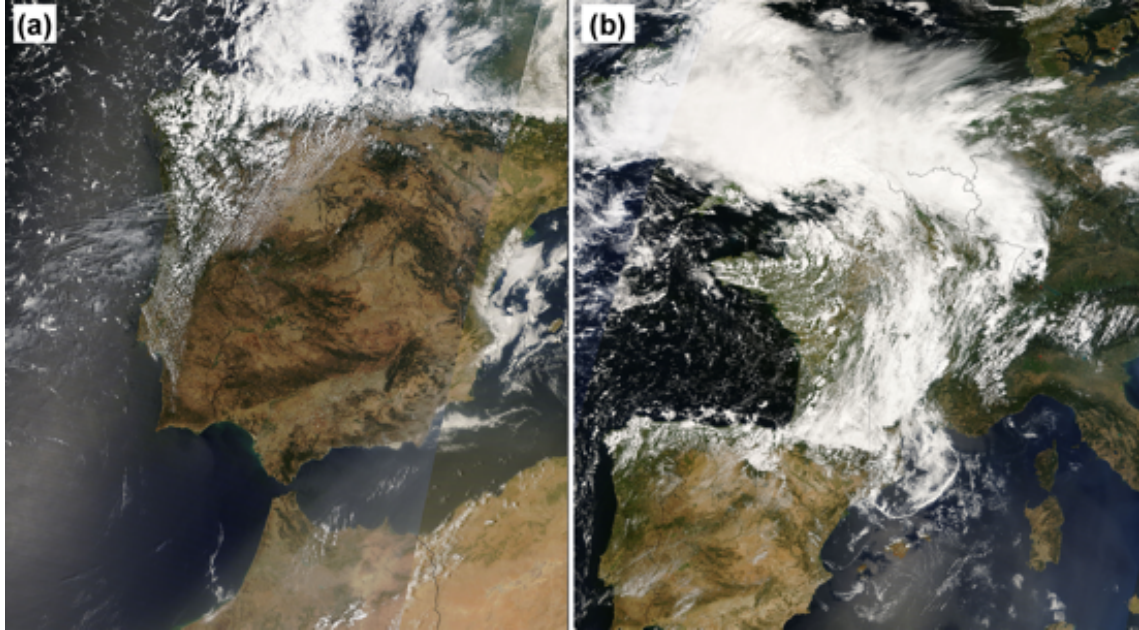
Figure 4.2: Terra MODIS visible satellite imagery: (a) composite of overpasses at 1150 (left part) and 1015 UTC (right part) on 19 July 2007 and (b) at 1225 (left part) and 1050 UTC (right part) on 20 July 2007. Available at: http://rapidfire.sci.gsfc.nasa.gov/.

19 July 2007 (Figure 4.2(a)) shows shallow, unorganized cumulus clouds over north-western Spain but not further to the east in the air associated with high θ_e values (Figure 4.1(d)). On the next day, at 1050 UTC 20 July when the developing cyclone moved to the UK, the satellite picture (Figure 4.2(b)) shows the occluded part of the frontal system with dense high level clouds over England and Ireland. Cirrus is fraying out on the northern edge. Below the cirrus shield over western Germany intense convective cells are triggered ahead of the cold front. Over France shallow cumulus formed in the cold air that arrived behind the cold front.

4.2 Water vapour and wind observations

Figure 4.3 shows the lidar observations of BSR, specific humidity and wind speed for the flight segment described in the previous section with superimposed ECMWF analysis fields. The topography along the cross section indicates the maximum elevations of the Cantabrian Mountains after the turn over the Atlantic at about 450 km distance, followed by the central Castilian plateau and the decline towards the Ebro valley. The BSR depicts clouds with a cloud top height at $\sim$3 km altitude in the first part of the flight segment and low aerosol content (BSR < 3) in the troposphere above the clouds (Figure 4.3(a)). The symmetric appearance in the cloud structure before and after the turn at a distance of $\sim$200 km is due to the spatial proximity of the probed airmasses in the southwesterly flow.
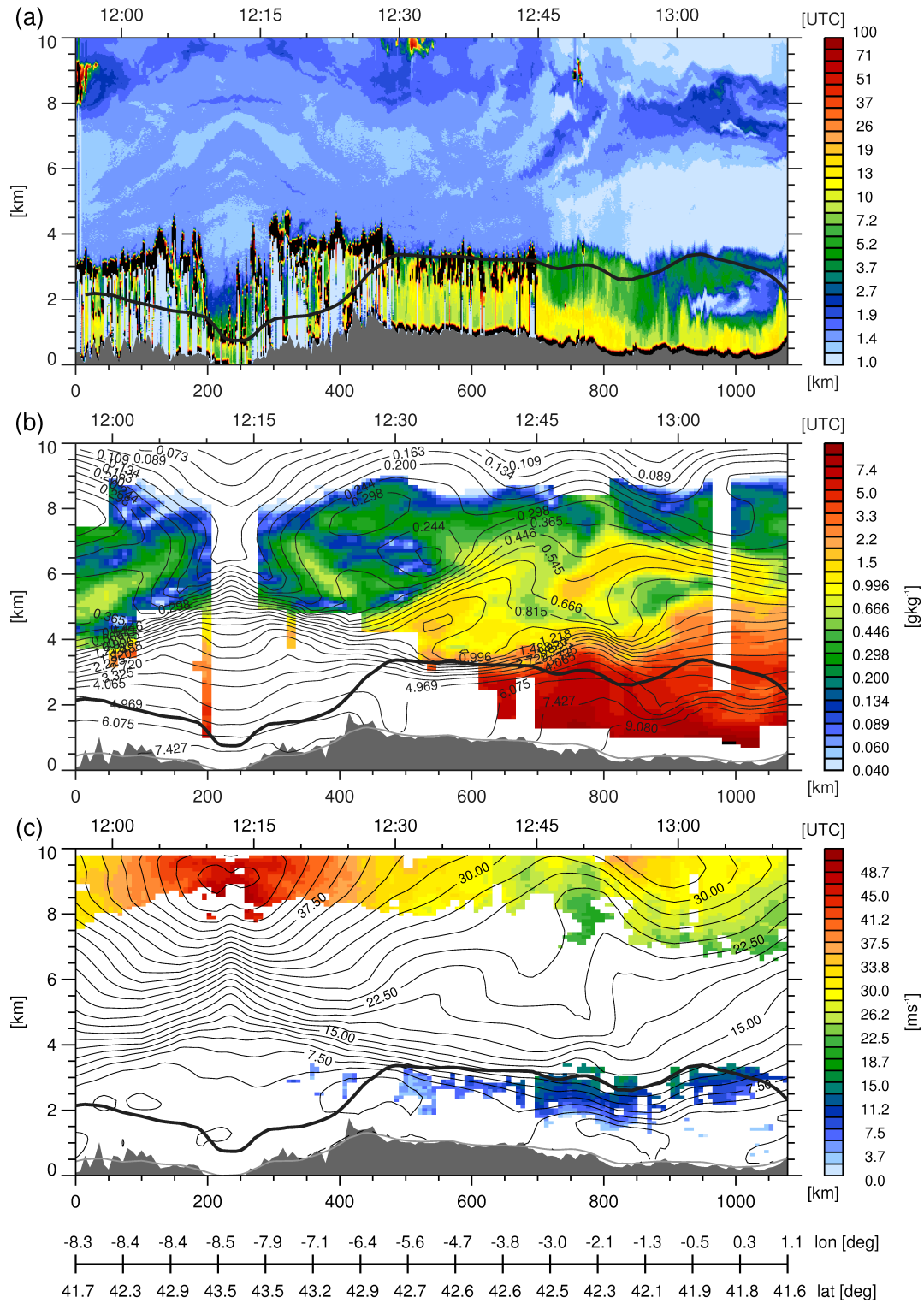
Figure 4.3: Lidar measurements on 19 July 2007: (a) BSR at 1064 nm in logarithmic scale; (b) specific humidity q (g kg^{-1}) in logarithmic scale, superimposed with contour lines of ECMWF short-term forecast and analysis data; and (c) horizontal wind speed (m s^{-1}), superimposed with ECMWF isotachs. Black line indicates BLH as diagnosed by the ECMWF IFS. Dark grey areas show the topography interpolated from GLOBE-DEM (Hastings et al. 1999), the light grey line marks the topography interpolated from the ECMWF model.

The top height of the convective clouds increases slightly towards the north. Figure 4.4(a) shows a sounding from a dropsonde that was released at 1225 UTC (∼420 km distance in Figure 4.3) over the Cantabrian Mountains. Apparently, the dropsonde penetrated one of the convective clouds as the profile indicates a saturated moist adiabatic layer below 3.5 km altitude (650 hPa). Above that layer, the moisture rapidly decreases in the clean air. The high dew point differences (T-T_D) indicate low relative humidity in the free troposphere. The convective clouds are capped by a temperature inversion at ∼3.5 km altitude.
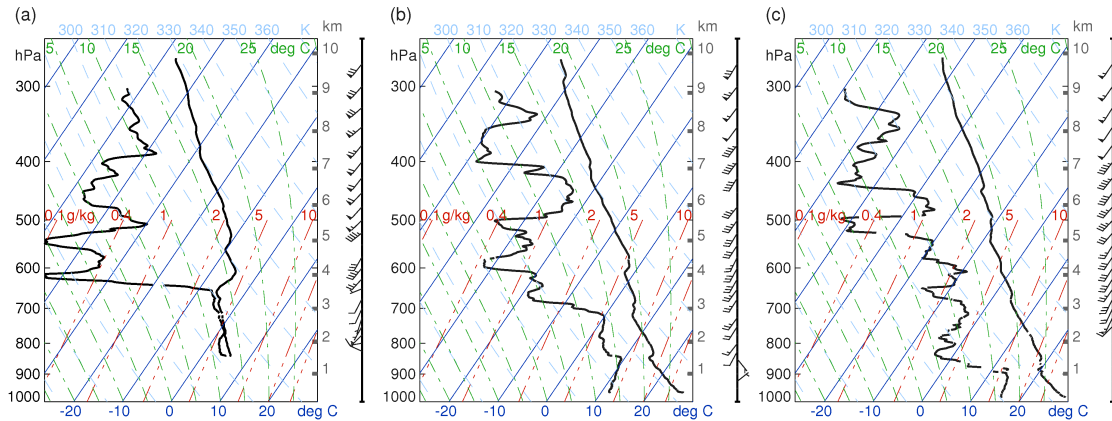
Figure 4.4: Skew-T log-p sounding from dropsondes released at (a) 1225 UTC, (b) 1254 UTC and (c) 1304 UTC on 19 July 2007. Left black line shows dew point temperature (T_D in °C) and right black line temperature (T in °C). Isotherms are indicated by sloping solid blue lines. Dry adiabats and moist adiabats are shown by light blue dashed and green dash-dotted lines. Saturation mixing ratio is given by red dash-dotted lines. Winds barbs indicate 5 knots (∼2.5 m s^{-1}, half barb), 10 knots (∼5 m s^{-1}, full barb) and 50 knots (∼25 m s^{-1}, pennant).

The cloud top height is significantly lower (∼1 km) in the marine PBL over the sea (at a distance of ∼200 km). Further to the east, at about 700 km distance in Figure 4.3(a), the absence of a strong capping inversion and a warmer PBL presumably prevented cloud formation (Figure 4.2). However, also in this region a strong vertical aerosol gradient was observed. The upper edge of the layer with BSR ≈ 5 decreases rapidly from ∼3.5 to ∼1.5 km towards the end of the flight segment. The aerosol particles in this layer are probably affected by PBL transport processes during the previous day. An elevated and separated aerosol layer occurs above the PBL between 1256 and 1310 UTC at about 3 km altitude. Closer to the ground an aerosol layer with BSR values up to 20 and a depth of 1 km follows the terrain. The upper boundaries of both layers coincide at the end of the flight.

Figures 4.4(b) and (c) show the thermodynamic situation in the cloud free air at 1254 and 1304 UTC. A vertically constant humidity and a dry adiabatic lapse rate in the dropsonde profiles up to 1.5 km and 1.1 km altitude reveal that the surface-based aerosol layer coincides with the mixed layer. The elevated layer shows

nearly dry adiabatic temperature profile and the lower but relatively well mixed humidity confirms the existence of a residual layer up to ~3 km altitude. In the free troposphere both dropsonde profiles show a decrease of moisture and the dew point difference indicates dry airmasses. At about 6 km altitude a moist layer appears that is better visible in the DIAL cross section in Figure 4.3(b).

The ECMWF analyses are in qualitatively good agreement (a quantitative comparison follows in section 4.4) with the observed humidity and wind structure (see Figures 4.3(b) and (c)). Therefore, this data is used to facilitate the interpretation within data gaps that are due to cloudy regions and curved flight segments. A nearly 2 km thick layer characterized by an enhanced vertical gradient of moisture that approximately follows the cloud top height and the upper boundary of the residual aerosol layer. This layer marks the transition from moister air in the PBL to drier air above. The humidity in the northwestern part of the flight decreases vertically from values around 3 g kg^{-1} to values lower than 0.5 g kg^{-1} in this layer. Over the Castilian plateau (~500 km) the layer splits in two bands. The lower part extends eastwards and the humidity increases towards the end of the flight to maximum values of ~11 g kg^{-1} inside the PBL. The well mixed aerosol layer and the vertically nearly constant humidity values point to convective turbulence in this region. Moisture decreases from ~9 g kg^{-1} in the mixed layer to values of ~3 g kg^{-1} above. In the free atmosphere, the humidity is higher in the eastern part of the flight segment. The lowest humidity values (<0.1 g kg^{-1}) occurred at ~8 km when the aircraft approached the jet region close to the trough centre (at around 250 km distance). The moister upper-level air on the anticyclonic side (distance > 500 km) of the jet is related to southerly advection.

The wind velocities (Figure 4.3(c)) reveal maximum values up to 45 m s^{-1} at the jet stream level in ~9 km altitude. The wind rapidly decreases towards lower levels and to the east with a secondary upper-level maximum near 2°W. In the PBL winds are weak and range between 3 and 10 m s^{-1}. The wind barbs of the dropsondes in Figure 4.4 confirm the vertically increasing winds from southwesterly directions in the entire free troposphere.

Additionally, Figure 4.3 shows the boundary layer height (BLH) from the operational analysis of the ECMWF's IFS interpolated on the flight track. This diagnosed BLH is located below the observed cloud top height before 1230 UTC (see Figure 4.3(a)). This might imply inaccurately simulated convection over the mountainous terrain by the IFS. Remarkably, the agreement between the cloud top height and the BLH is nearly perfect over the flat area of the central Castilian plateau. Further east, the diagnosed BLH coincides with the upper edge of the residual layer visible by enhanced BSR values in the cloud free region.

4.3   WCB observations

The method of calculating trajectories from every observation point was applied for this case study to identify measurements of WCB air parcels (see section 3.2.2). Figure 4.5(a) shows the maximum ascent Δp_{max} identified as the magnitude of maximum pressure decrease within 48 hours along a seven-day (168 h) trajectory which is composed of 60 h forward and 108 h backward calculations. To illustrate the vertical structure of the WCB a threshold of the pressure decrease of at least 400 hPa in 48 h is chosen. Figure 4.5(b) depicts the time lag when the ascent began
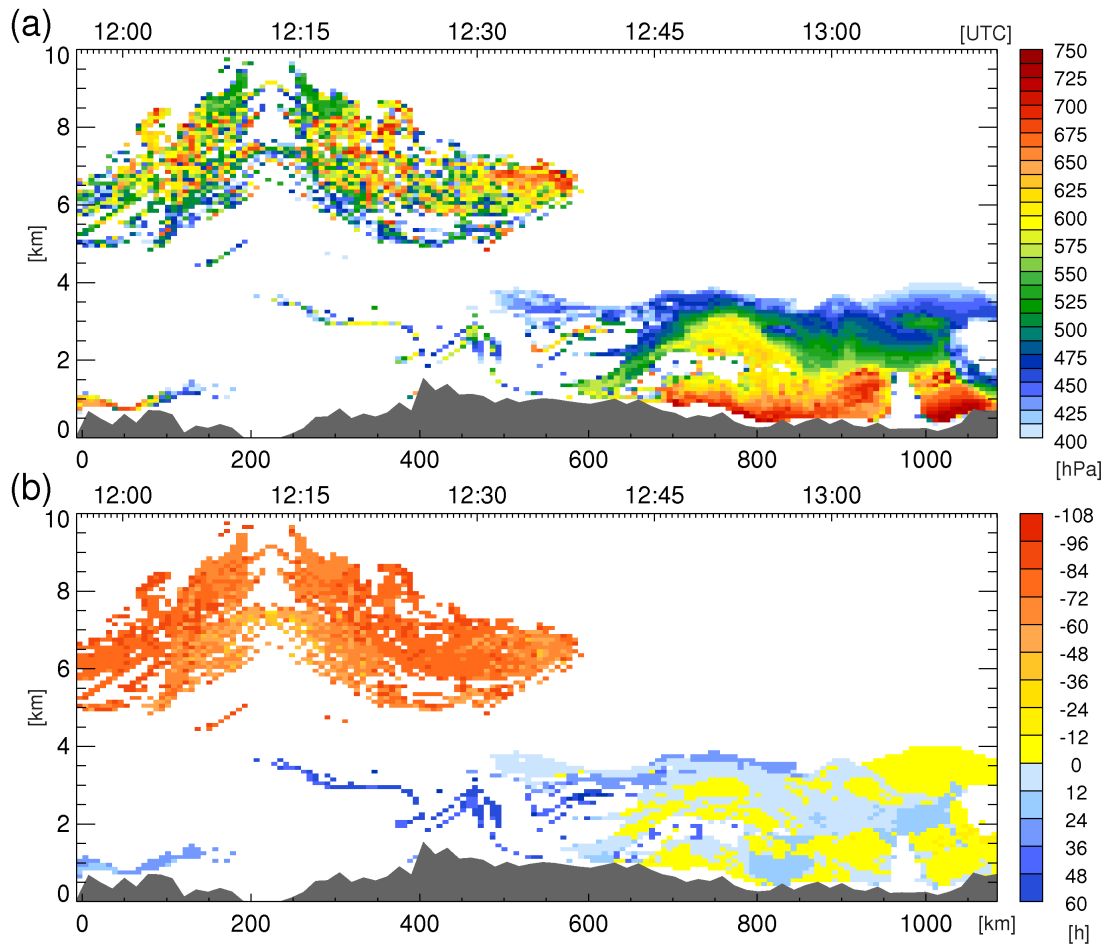
Figure 4.5: Locations of lidar observations with an ascent larger than 400 hPa in 48 hours. (a) Magnitude of the maximum decrease of pressure Δp_{max} (hPa) in 48 hours; (b) time lag of the ascent (in hours relative to the observation time). For the method to calculate the trajectories see section 3.2.2

or will begin relative to the time of the airborne lidar observation. Negative values (yellow to red coloured) indicate that the ascent of the observed air parcels within the WCB started before, whereas positive values (blue coloured) imply that the observed air will ascend after the airborne observations.

Two main regions of identified WCB air parcels can be distinguished by altitude, time lag and vertical distribution of Δp_{max}-values. One region in the first part of the flight segment is located in the upper troposphere near the jet stream which is characterized by very low humidity values (see Figure 4.3(b)). These air parcels ascended $\sim$3 days in advance of the observation (see the negative time lag values in Figure 4.5(b)). The second region with Δp_{max}>400 hPa appears in the humid PBL during the second half of the flight segment. These air parcels will flow into a WCB as the respective time lags are near zero or positive, i.e. the parcels just started to ascend or were about to start within 12 hours after the observations. The vertical distribution of the maximum ascent values Δp_{max} differs in the two regions (see Figure 4.5(a)). The lower region shows coherent horizontally extended layers of equal magnitude in Δp_{max} and, generally, a vertical decrease in Δp_{max}. Conversely, the Δp_{max} distribution at upper-levels is noisy and features a large variability without a remarkable layering and coherence.

WCB trajectories that satisfy the standard WCB criterion Δp_{max}>600 hPa in 48 h are shown in Figure 4.6(a) and (b). The two different WCB regions identified in the cross sections can be clearly distinguished by the pressure at the time of the observation (see also colouring of the trajectory pressure at 19 July 12 UTC in Figure 4.6(c)). The green and blue coloured trajectories cross the western part of the lidar curtain in the upper troposphere above 500 hPa. In accordance with the diagnostic in Figure 4.5(b) these parcels ascended already 2 to 3 days before the flight (see Figure 4.6(c)). After their ascent over Western Europe, the parcels were embedded in the trough circulation and travelled from Scandinavia to the Iberian Peninsula in $\sim$36 hours. From there, the air parcels again propagate to the north after the observations. In agreement with the small positive time lag values for the lower tropospheric region, the reddish parcels ascend nearly simultaneously, directly after the observation time in a spatially coherent belt over France (see pressure evolution in Figure 4.6(c)). In the subsequent outflow phase, the formerly coherent belt splits into three branches with different orientations.

During their ascent, parcels lose most of their water vapour (Figure 4.6(d)), which initially varies between 5 and 10 g kg^{-1}. Additionally, the potential temperature increases due to latent release (Figure 4.6(e)). The backward part of the trajectory calculation shows that most parcels are transported on the rear side of the persistent trough and either descend slightly or move close to sea level. Whereas most air parcels move over the Iberian Peninsula prior to the lidar observation time, another branch with parcels approaches from the Mediterranean to the south of Sicily and Sardinia. Interestingly, the ascent of parcels in both branches takes place at approximately the same position over France (Figures 4.6(a) and (b)).
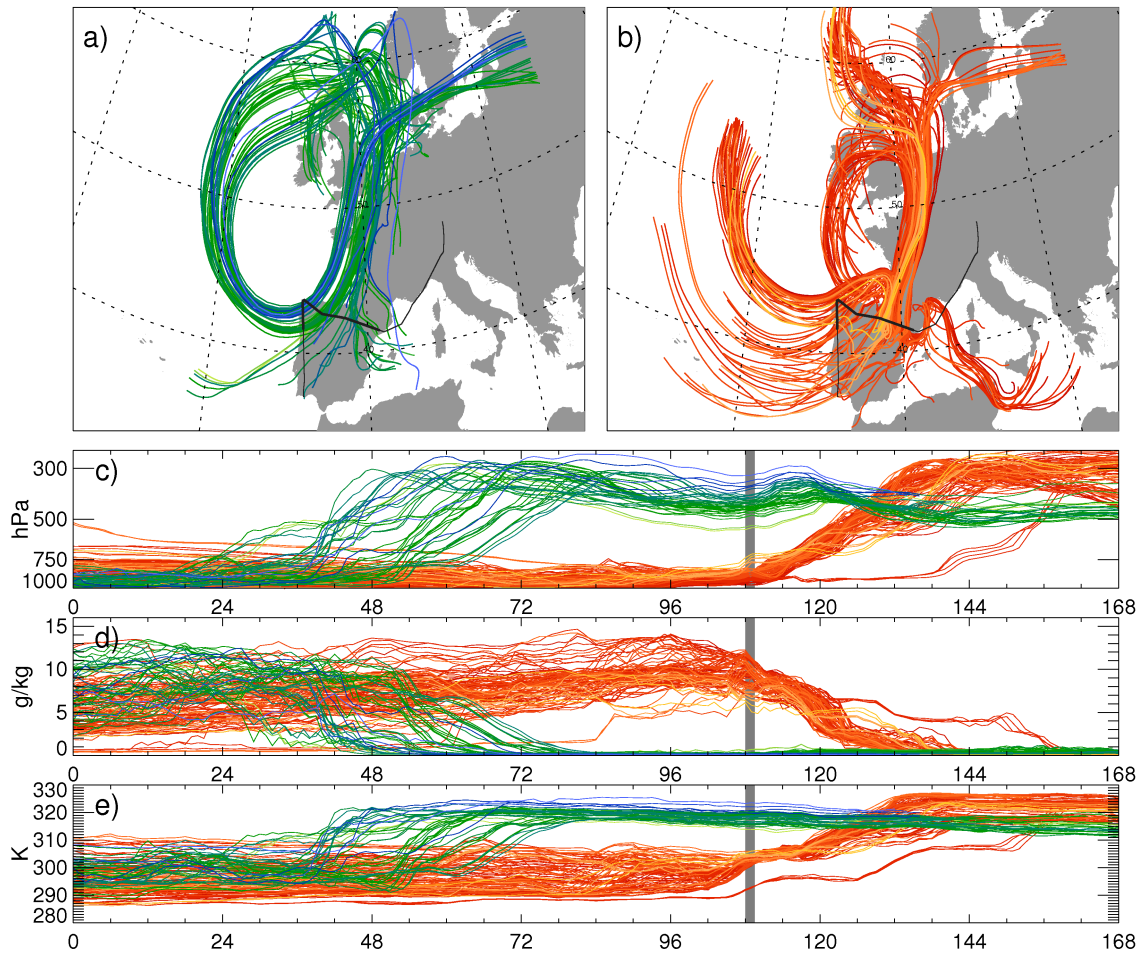
Figure 4.6: WCB trajectories ascending more than 600 hPa in 48 hours. Trajectories are colour-coded in dependence of the pressure at the time of the observation. The WCB ascent in (a) advance and (b) after the observations. Black line in (a) and (b) indicates the flight track. The thick part corresponds to the section of collocated lidar observations. Temporal development of (c) pressure, (d) specific humidity and (e) potential temperature. Time (in h) is relative to 00 UTC 15 July. The grey bar in (c), (d) and (e) indicates the time of the lidar observations. For a clear overview every second trajectory (coloured according to the pressure at the time of observation) is shown. For the method to calculate the trajectories see section 3.2.2.

Figure 4.7 depicts (a) the longitude of the starting position, (b) the maximum pressure decrease Δp_{max} as well as (c) the pressure and (d) humidity evolution for the WCB trajectories which ascend after the time of the observations (reddish parcels in Figure 4.6). The eastern portion of the WCB consists of air parcels (orange and red) that originate from the Mediterranean. They also form the branch of parcels with the anticyclonic outflow towards Russia. Trajectories with maximum ascent ($\Delta p_{max} = 774$ hPa) are located at the centre of the WCB (Figure 4.7(b)). These air parcels are predominately advected from the Atlantic (to the west of 20°W and north of 50°N). They differ from the rest of the Atlantic trajectories by moving at low levels (Figure 4.7(c)) southward over the Bay of Biscay towards the observation location.
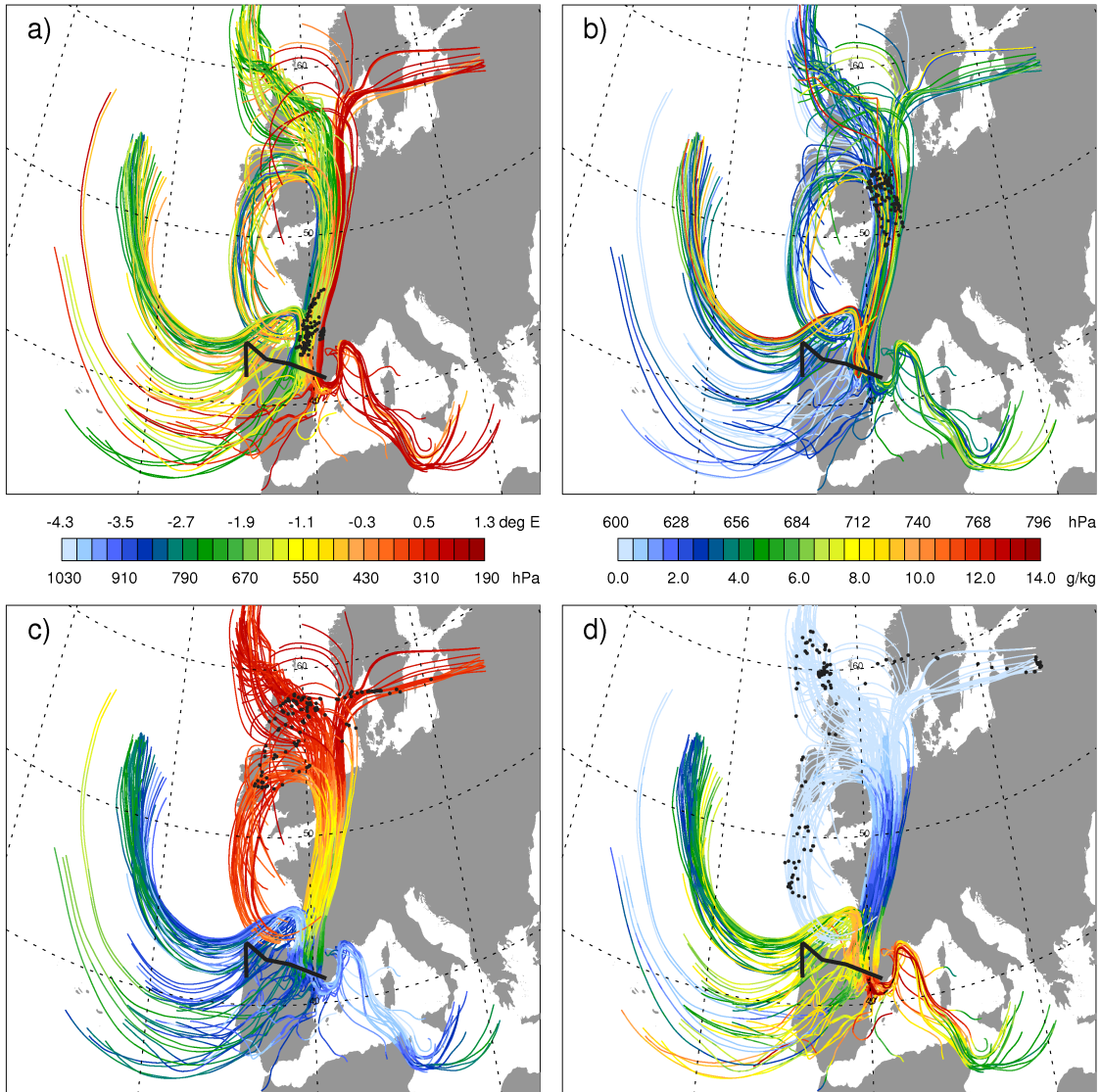
Figure 4.7: Positions of WCB trajectories ascending more than 600 hPa in 48 hours after the observations (see Figure 4.6(b)). Colour-coding in upper row depends on (a) longitude of the starting position along the flight segment and (b) maximum pressure decrease Δp_{max} in 48 hours. The bottom row is colour-coded dependent on (c) pressure and (d) moisture content at the parcel positions along the respective trajectory. Black dots indicate position for 00 UTC 20 July (a, corresponding to the 120 h time mark in Figure 4.6), 12 UTC 20 July (b), 00 UTC 21 July (c) and 12 UTC 21 July 2007 (d). For a clear overview every second trajectory is shown.

The Mediterranean trajectories exhibit a larger 48 hour ascent than the southern portion of the Atlantic ones. They also move close to the sea surface, accompanied by a humidification most probably due to surface fluxes (Figure 4.7(d)). During the ascent the parcels quickly lose their moisture, which decreases to less than 0.5 g kg^{-1} when they reach the outflow region. The 48-hour decrease of moisture within the WCB varies from 6 to 14.3 g kg^{-1}. The mean humidity loss along all trajectories is 10.3 g kg^{-1}. The 48 hour change in potential temperature amounts to 27.6 K on average with minimum and maximum values of 17.7 and 34.7 K, respectively.

Additionally, all panels in Figure 4.7 show the positions of the observed parcels at different times during the WCB ascent by means of black dots. The parcels are located close together near the flight path over southwestern France between 700 and 550 hPa 12 hours after the observations (Figure 4.7(a)). Another 12 hours later, at 12 UTC 20 July (Figure 4.7(b)), the parcels begin to spread horizontally and vertically. The fastest parcels already reach the upper troposphere over the UK. The slower ones remain in the mid-troposphere over northeastern France. Of course, only a part of the air that is lifted within the developing system was probed by the lidar measurements. However, comparing the positions in Figure 4.7(b) with the MODIS image (Figure 4.2) it can be confirmed that the observed airmass was embedded in the cloud system of the cyclone.

4.4 Differences between ECMWF data and lidar observations

Figure 4.8 shows the difference between ECMWF data and lidar observations of (a) specific humidity and (b) the horizontal wind speed along the lidar cross section. In
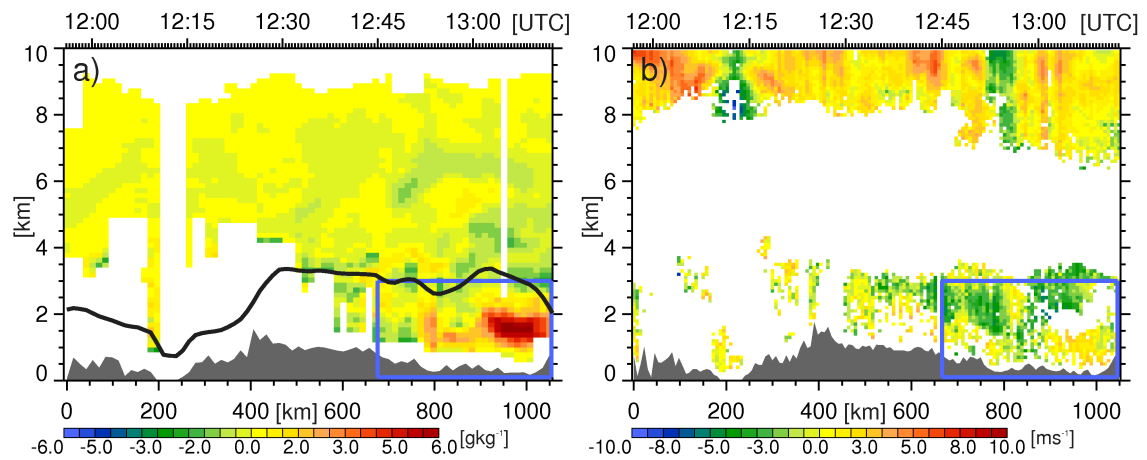
Figure 4.8: Absolute differences of ECMWF short-term forecasts and analyses and lidar observations on 19 July 2007 of the specific humidity (a) and the horizontal wind speed (b). Blue rectangle indicates the approximated WCB inflow region. Black line in (a) indicates BLH as diagnosed by the ECMWF IFS. Dark grey areas show topography interpolated from GLOBE-DEM (Hastings et al. 1999).

the eastern part of the flight segment a large positive moisture deviation beneath 3 km indicates an overestimation of the humidity by the IFS. The largest deviations up to 7 g kg^{-1} (corresponding to a relative difference of 100 %, see section 3.2.1) are located in the same region from which air parcels ascended with maximum Δp_{max}. It is noteworthy that this significant moisture bias occurs in the WCB inflow region, i.e.

within an airflow that is of great importance for the subsequent dynamical evolution of the probed weather system. Based on Figure 4.5 an approximate inflow region (blue rectangle in Figure 4.8) is defined below 3 km. Averaged over the inflow region, the mean moisture bias is $\sim$1.0 g kg^{-1} (14 %). Above the inflow region, negative deviations exist. The absolute deviations are smaller at low moisture contents in the upper troposphere. However, the partly high relative deviations (up to 200 %, not shown) indicate a significant overestimation of humidity in the upper troposphere. As discussed before, this region is less homogeneous compared to the inflow region (see Figure 4.5). Note that the deviation in the eastern part of the inflow region is smaller close to the ground which could be an effect of a better representation of the developing mixed layer in the IFS.

The absolute wind deviations (Figure 4.8(b)) are largest at upper-levels and range between -3 and +7 m s^{-1}) where higher wind speeds exist. Averaged over the inflow region the wind speed is underestimated in the IFS by -1.3 m s^{-1} (-18 %). However, below 1.5 km wind speed is typically overestimated.

A comparison of profiles from the lidar measurements, IFS data, and a dropsonde profile, in the area of overestimated humidity in the WCB inflow, is presented in Figure 4.9. Note that the line-like dropsonde measurement is compared to a lidar profile consisting of an accumulation of laser shots. The specific humidity measured by dropsonde and lidar are in good agreement and show the same shape of the vertical humidity distribution (see Figure 4.9(a)). Two lidar humidity profiles are shown
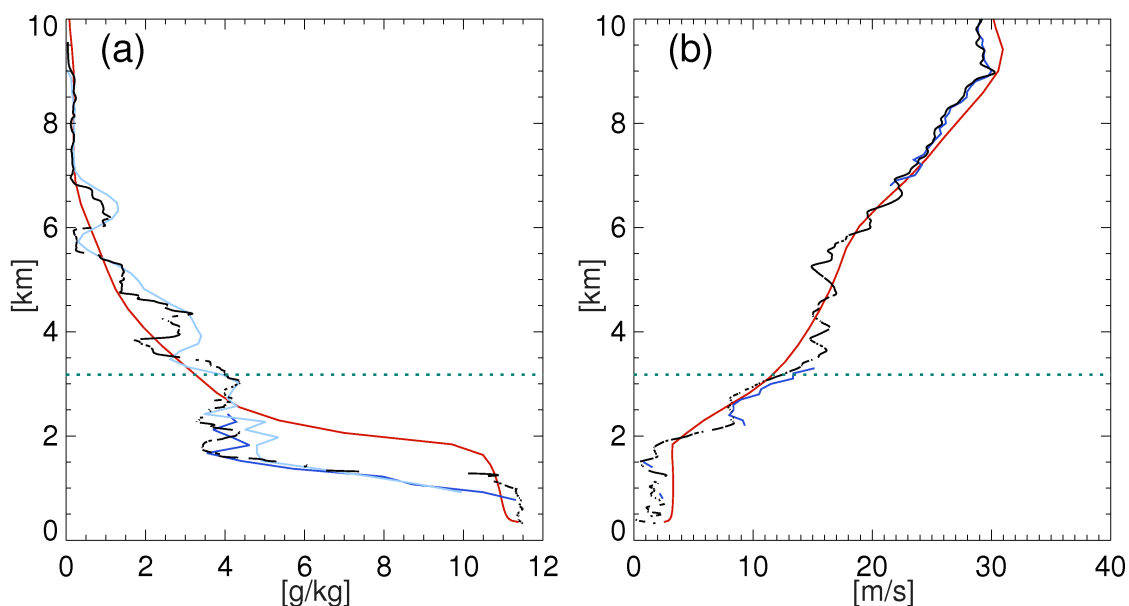
Figure 4.9: Dropsonde comparison on 19 July 2007: (a) Mixing ratio from dropsonde (black line, at 1304 UTC), ECMWF (red line, interpolated to the same time and position) and DIAL (light blue profile at 1304 UTC, dark blue at 1305 UTC). (b) Same for wind speed but with DWL profile at 1304 UTC (dark blue line). Dashed green line indicates BLH as diagnosed by the ECMWF IFS.

since the dropsonde is launched temporally in between. To some extent differences can be explained by the different character of the measurement as well as by the horizontal drift of the dropsonde with the southwesterly wind perpendicular to the flight track. The dropsonde profile confirms the overestimated humidity of the IFS runs between 1.3 and 2.5 km altitude and the smaller deviation below. Above 3 km the model is able to represent the general decrease of moisture with height, but it does not resolve the fine structures probably due to the limited resolution. The wind speed of the lidar profile and the simultaneous dropsonde are in very good agreement (± 2 m s^{-1}). Also the wind speed profile from the IFS compares very well (± 5 m s^{-1}) with the observations. The WCB inflow region is characterized by overestimated wind velocities at low wind speeds beneath 2 km altitude.

4.5   Moisture uptake analysis

In the previous section a strong moisture difference between the IFS and the lidar observations has been discovered in the WCB inflow region. Figure 4.9(a) indicates nearly constant humidity values (~ 4 g kg^{-1}) in an elevated residual layer between 1.6 and 3 km altitude observed by the DIAL and the dropsonde which were not simulated by the IFS. Figure 4.3 shows that the BLH as diagnosed by the ECMWF's IFS coincides with the top of this residual layer at ~ 3 km altitude. The ECMWF model does not simulate the structure of the lower boundary layer as shown by the differing vertical humidity profiles below 2 km. As the layer of increased humidity deviations is located inside the ECMWF boundary layer (see Figures 4.8(a) and 4.9(a)) one might guess that a too strong parameterized turbulent mixing distributed the humidity in the model over a too deep layer. The somewhat deeper (~ 1.9 km) and less moist (~ 11 g kg^{-1}) evolving mixed layer in the IFS compared to the mixed layer observed by the dropsonde (~ 1.3 km and 11.5 g kg^{-1}) in Figure 4.9(a) supports this hypothesis. However, the probably incorrectly represented local mixing in the IFS cannot explain the integrated moisture excess that occurs up to ~ 3 km altitude. Therefore, it is interesting to further investigate the processes that potentially led to the overestimated humidity in the ECMWF model.

Figure 4.7 indicated that the airmass observed in the eastern part of the flight segment originated from the Mediterranean (see also section 4.3). These trajectories show an increase in specific humidity while they were advected close to the sea surface. The history of the probed airmasses and the related moisture uptake will be discussed based on 7.5 day backward trajectories that were calculated from every lidar observation point in the WCB inflow region (see Figure 4.8). For these

trajectories a moisture source diagnostic (see section 3.2.2) was applied to analyse the location and time of the moisture uptake. The subsequent analysis aims at clarifying whether the observed enhanced deviations can be attributed to an increased moisture uptake in distinct uptake regions.

The trajectories in the WCB inflow region can be divided into five clusters defined by their origin, pathways and speed. The clustering was defined by the area encompassing characteristic groups of parcel positions ∼49 h before the time of the observations. Figure 4.10(a) shows the positions of the backward trajectories at 12 UTC 17 July within the five clusters. The dark blue box shows parcels that
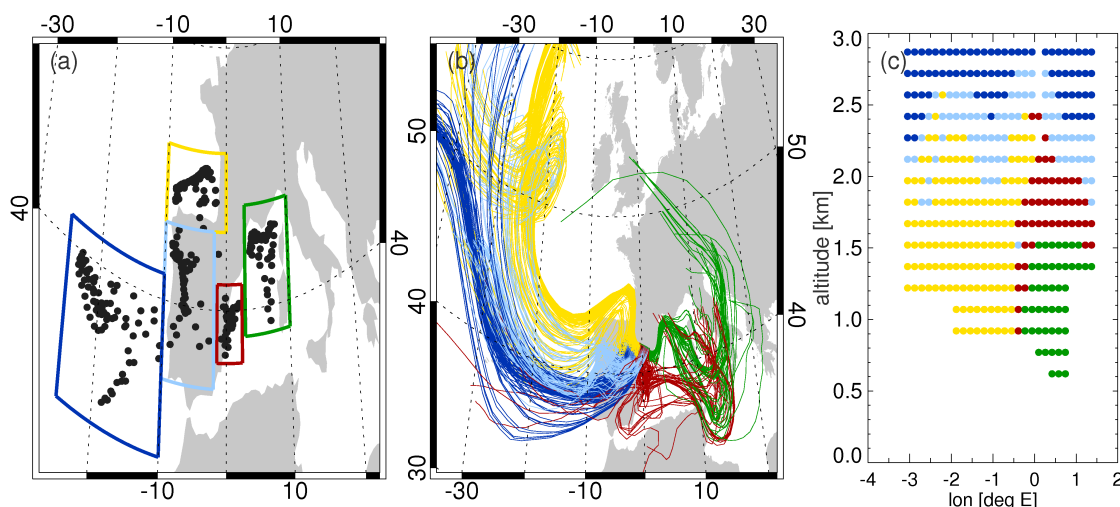
Figure 4.10: Clustering of backward trajectories starting in WCB inflow region along the lidar curtain (see Figure 4.8(a)) based on different origin, pathways and speed of the trajectories. (a) Trajectory positions at 12 UTC 17 July 2007 (-49 h) defining the five different clusters; coloured rectangles indicate clustering regions. (b) Positions of the trajectories. (c) Starting positions along the lidar cross sections. (b) and (c) are coloured in accordance with the five clusters.

are already located over the Atlantic whereas the light blue box borders parcels over the Iberian Peninsula. To the north, the yellow box contains parcels over the Bay of Biscay. Two different regions with trajectory positions are found over the Mediterranean. The positions located further south close to the Spanish coast (red box) and trajectories that travelled to the north and are close to the French coast (green box).

The yellow, light blue and dark blue trajectory clusters originate from the Atlantic (Figure 4.10(b)). The dark blue air parcels are travelling comparatively fast on the backside of the trough while descending from higher altitudes (∼500 hPa). The light blue coloured trajectories also illustrate a transport over the Iberian Peninsula. However, their locations are much closer to the ground and they experience longer residence times over land. The yellow trajectories perform loops over the Bay of Biscay at lower altitudes. The Mediterranean trajectories are divided into two

clusters. In contrast to the green trajectories that move along the northern coast of Spain, the red parcels are transported further to the south and are characterized by long residence times (3.5 days) off the coast of Spain (at $\sim 0°E/\sim 39.5°N$). Figure 4.10(c) illustrates the location of the 5 clusters on the lidar cross section. The trajectories that travel over the Iberian Peninsula (light and dark blue) belong to starting points in the upper part of the inflow area. The highest starting points at driest humidity values in the inflow region are associated with the descending dark blue trajectories. Beneath, the remaining trajectories from the Atlantic (yellow) start in the western part of the lidar subsection. The Mediterranean trajectories (red and green) are associated with the airmass that was probed at the end of the flight below about 2 km.

The identified moisture uptake regions for all trajectories from the WCB inflow region are shown in Figure 4.11. Altogether, 77 % of the ECMWF moisture at
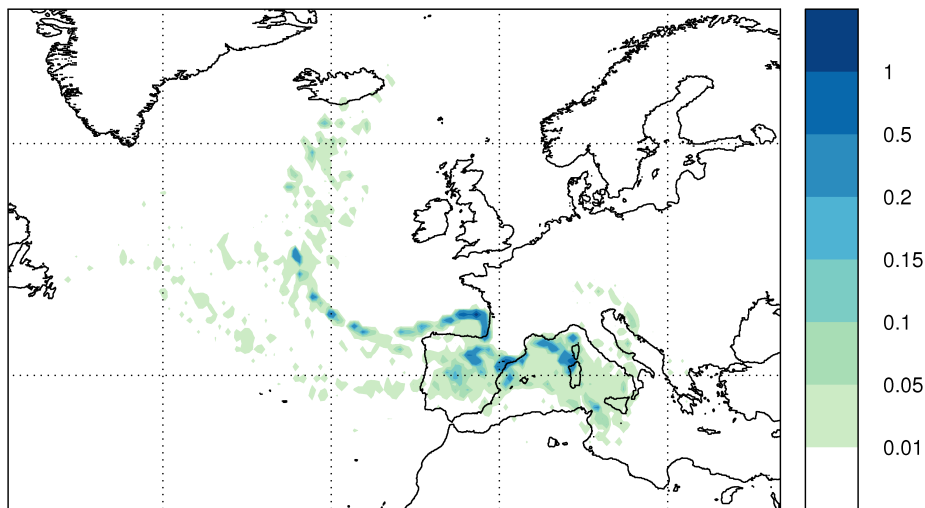
Figure 4.11: Moisture uptake regions for trajectories starting in WCB inflow region (see Figure 4.10). Units are % of final humidity per 1000 km^2.

the trajectory starting points can be related to uptake in these regions. Different regions with oceanic and continental moisture uptakes appear that can be associated with the origin of air parcels of the 5 different clusters. The moistening of the yellow trajectories is reflected in the uptake region over the Bay of Biscay and indicates that high moisture values in the western part of the WCB inflow region arise from evaporation over the Atlantic. The light and dark blue trajectories can be associated with weak moisture uptake over the Iberian Peninsula. The green and red trajectories experience strong moisture uptake over the Mediterranean and the northeastern part of Spain. In particular for the green cluster, a distinct maximum occurred between Corsica and France.

Figure 4.12 links the accumulated moisture uptake along the trajectories with the moisture deviations between the IFS and the lidar observations. The highest
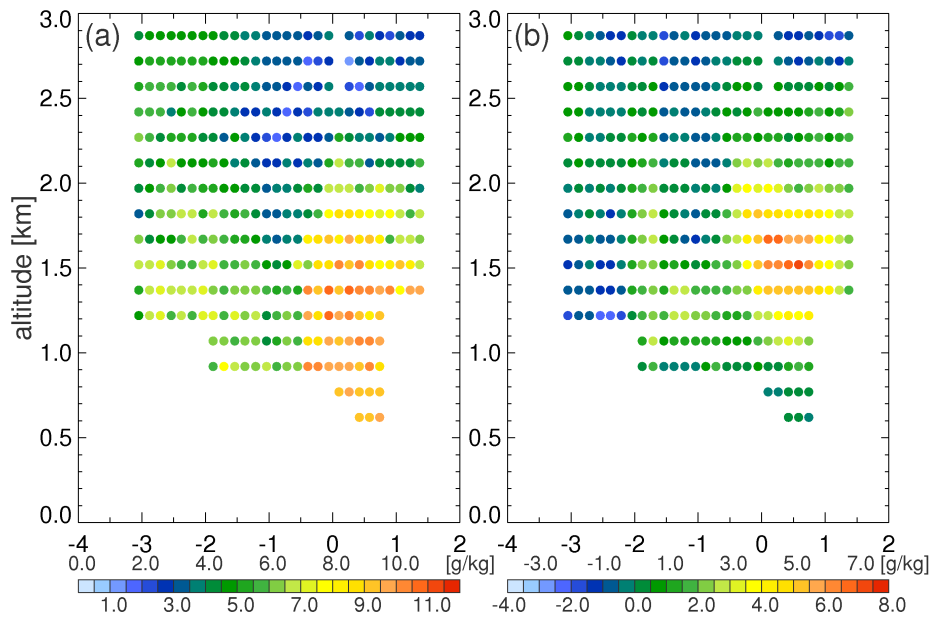

Figure 4.12: Starting points of backward trajectories in the WCB inflow region (see also Figure 4.8(a)). (a) shows the total (7.5 day) moisture uptake along the respective trajectory; (b) indicates the moisture deviation (IFS - LIDAR, note that the colour bar is different to Figure 4.8(a)).

uptake values (8 to 12 g kg^{-1} during the 7.5 days) occurred in the eastern part of the flight segment (Figure 4.12(a)). The maximum positive moisture deviations (Figure 4.12(b)) occur in the upper part of this area with high total moisture uptake values. This indicates that a high total moisture uptake does not necessarily lead to a high deviation in this particular case. However, interestingly, both high moisture uptake and large deviations are associated with the Mediterranean trajectories (see red and green dots in Figure 4.10(c)). For this reason, the Mediterranean clusters (green and red) are investigated in more detail, especially during the first 25 hours along the backward trajectories (from 13 UTC 19 July to 12 UTC 18 July) when the air parcels are close together.

Figure 4.13 shows the positions and characteristics of trajectories with a total moisture uptake exceeding 1.5 g kg^{-1} in 25 hours. The position of the air parcels that fulfil this criterion are shown in Figure 4.13(a) as black squares together with the associated moisture deviation. This subgroup of the Mediterranean trajectories covers well the main region with high positive deviations. The moisture uptakes along these trajectories were not located over the Mediterranean, but mainly took place over land above the eastern part of the widening Ebro valley floor as well as on its flanks (Figure 4.13(b), see also total moisture uptake field in Figure 4.11). The red trajectories primarily move over the mountains located in the south and

descend to the valley floor (Figure 4.13(c)) between -25 h and -12 h. The green parcels move close to the sea surface. The simulated ascent of all trajectories towards the flight track in the last 12 hours indicates the initial phase of the WCB ascent. Figure 4.13(d) shows the magnitude of the moisture uptake. The red trajectories possess the largest uptakes during the late phase of their descent (-19 h and -13 h). The green trajectories mainly moisten when they reach land at -1 h and -7 h. During these 25 hours, accumulated moisture uptakes over land are substantial and amount to roughly 3 g kg^{-1}.
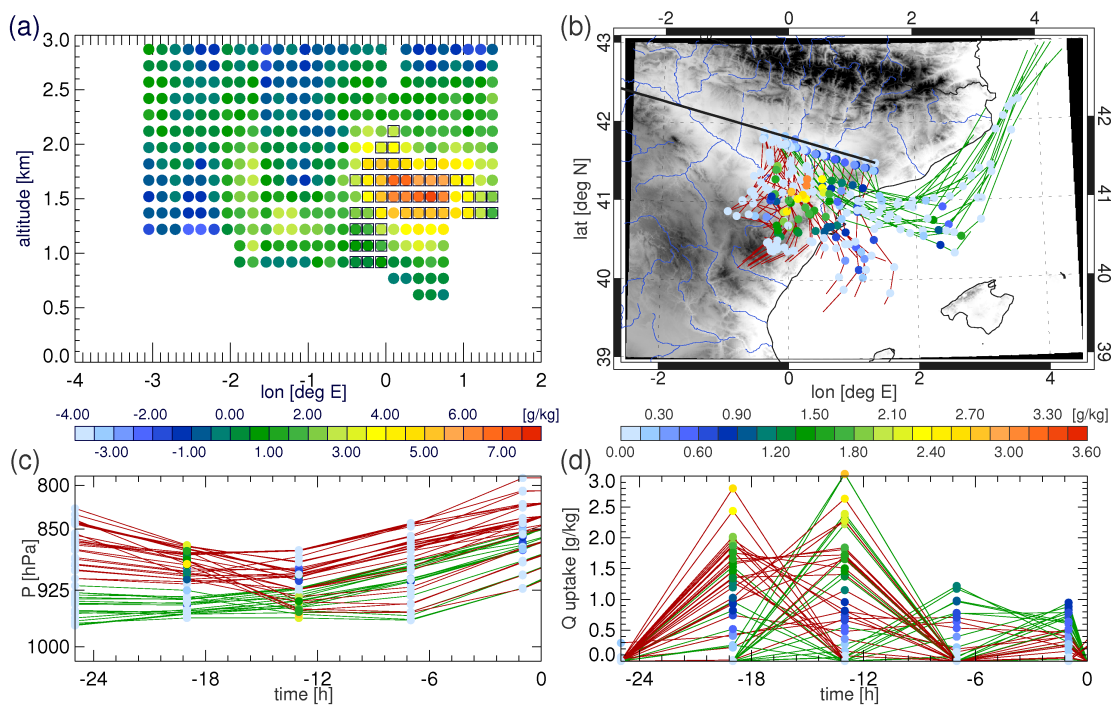
Figure 4.13: Starting points and trajectories that originate from the Mediterranean Sea and possess a total moisture uptake larger than 1.5 g kg^{-1} in 25 hours. (a) Moisture deviation (g kg^{-1}) with black markers showing starting positions of the trajectories; (b) location and strength of moisture uptakes, black line indicates inflow area on the flight track; (c) temporal evolution of pressure along the trajectory together with moisture uptakes (dots); and (d) temporal evolution of the moisture uptake along the trajectory. Red and green colouring of the trajectories is analogue to the clusters defined in Figure 4.10.

4.6 Summary

The ETReC 2007 mission on 19 July 2007 over Spain shows observations in the outflow of a first and inflow of a second WCB. This enabled a detailed investigation of the humidity structure in the inflow region of a WCB as revealed by lidar remote sensing profiles. Previous studies (e.g. Blackburn et al. 2008) showed that this WCB was associated to a cyclone which caused high impact weather, especially

high amounts of rain over the UK.

Cyclogenesis on the leading edge of a large-scale trough led to the development of a low level frontal system over France. A Lagrangian diagnostic with forward and backward trajectory calculations from every observation point was performed to directly associate observations with WCB airmasses. Two independent WCB events were observed. One WCB was probed by the lidar that ascended into the upper troposphere 2 to 3 days prior to the measurements. The second event corresponded to a WCB airmass that underwent a strong ascent immediately after being observed by the lidar. This WCB airmass at low levels was located in the warm sector of the developing cyclone. The WCB air ascended coherently ahead of the cold front after being probed by the lidar and spread out when reaching the outflow region over southern Scandinavia.

On average the trajectories starting from observations in the lower troposphere and exceeding an ascent of 600 hPa lost 10.3 g kg^{-1} of their initial humidity and increased their potential temperature by 27.6 K in 48 hours. During the 4.5 days before the observation, most of these parcels were advected within a stationary trough from the Atlantic Ocean and either descended to or moved close to sea level. Another branch originated above the Mediterranean at low levels showing a strong moistening due to surface evaporation. The advection of moistened air parcels influenced the humidity distribution portrayed by the lidar measurements. A comparison revealed that on average the humidity in the inflow region was overestimated by the ECMWF analysis by 1.0 g kg^{-1} (14 %) compared to the lidar. Although this average deviation is within the general uncertainty of humidity values in operational analyses, local peak deviations of up to 7.0 g kg^{-1} were identified. These very large deviations occur in the inflow region of a WCB and are thus of particularly high dynamical relevance.

The analysis of the diagnosed BLH in the IFS model and the comparisons of lidar and dropsonde observations with modelled humidity indicated that incorrect local mixing associated with an overestimated height of the mixed layer only partly explains the observed moisture deviation. A detailed investigation of 7.5-day backward trajectories starting in the WCB inflow region showed that most parcels associated with a large positive moisture bias were transported over the Mediterranean. A moisture source diagnostic illustrated that high total moisture uptakes in the model analysis occurred in these air parcels over the Mediterranean Sea and also over the eastern part of the Iberian Peninsula. The analysis of the moisture uptakes gives some support that the excess moisture in the inflow region is related to insufficiently represented evapotranspiration processes in the IFS that occurred in the Ebro valley. This leads to the hypothesis that land-surface evapotranspira-

tion may be crucial for accurately capturing the moisture content in the inflow of WCBs, at least during summer when evapotranspiration can be particularly intense and in regions where the airflow into WCBs originate (partially) from continental areas. The coherent distribution of the starting positions along the lidar cross section and the consistent transport from the Mediterranean underline the reliability of the moisture transport path that is shown by the model trajectories. However, incorrect moisture transport, either horizontal or vertical, the latter due to inaccurate representation of the turbulent boundary layer, has also contributed to the diagnosed moisture deviation.

Chapter 5

How can analysis errors of moisture affect the forecast of a WCB? - A case study on 19 September 2008

The objective of this chapter is to investigate the impact of analysis errors in the moisture fields of the WCB inflow region on the forecast of the subsequent WCB ascent and the associated latent heat release and PV production. Additionally, the impact on the forecast of the related extratropical cyclone will be analysed. This will be done for a mission flight during the T-PARC campaign performed on 19 September 2008. At first the synoptic situation (section 5.1) and the water vapour and wind lidar observations are interpreted (section 5.2). The observations related to a WCB are discussed in section 5.3 and model fields are compared with wind and water vapour observations in section 5.4. The impact of analysis errors on the forecast of the WCB and the related midlatitude cyclone is addressed in section 5.5 based on two forecast runs with different initial conditions.

5.1 Synoptic overview

The flight on 19 September 2008 started in Misawa, in the north of the Japanese main island Honshu at around 0110 UTC (see flight path in Figures 5.1(a) and (d)). After a short northward oriented flight section the aircraft turned eastward over the Pacific Ocean. At $\sim$154°E the aircraft turned southwestward towards the metropolitan area of Tokyo and landed in Atsugi at around 0510 UTC. Lidar observations of both humidity and wind were made between $\sim$0145 and 0430 UTC.
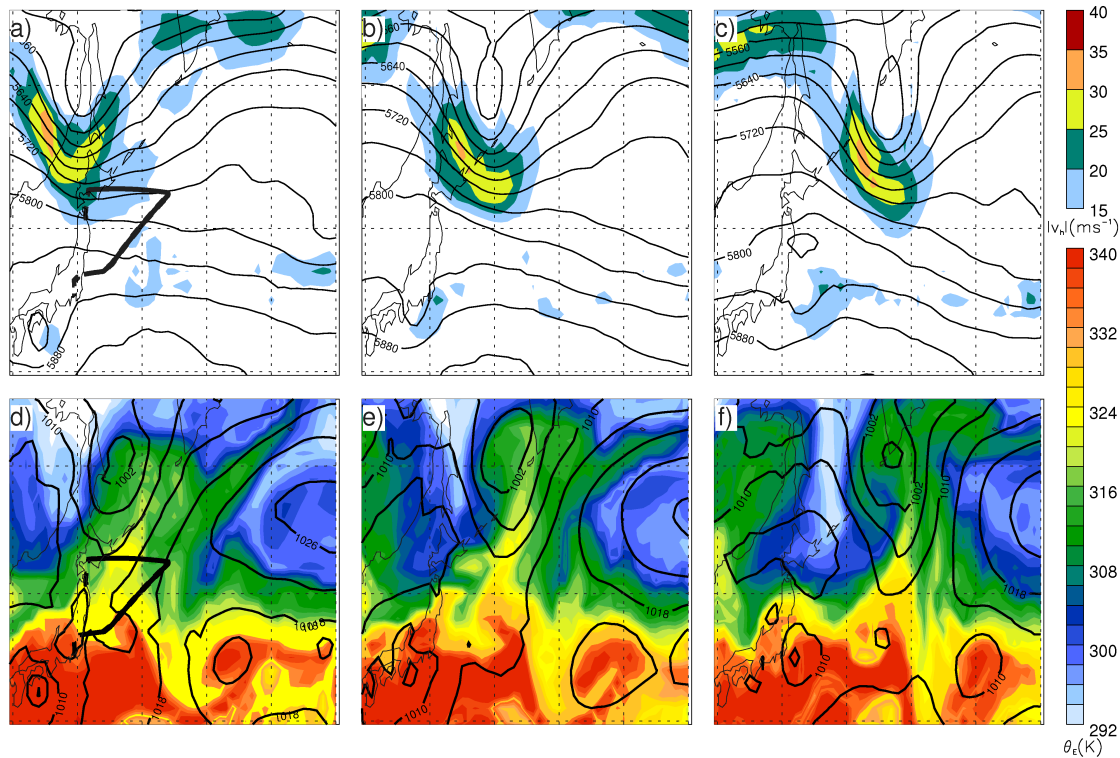
Figure 5.1: ECMWF analysis valid on (a, d) 00 UTC 19 September (b, e), 12 UTC 19 September and (c, f) and 00 UTC 20 September 2008. (a, b and c) Geopotential height (m, black lines) and horizontal wind speed (m s^{-1}, colour shaded areas) at 500 hPa. (d, e and f) Geopotential height (m, black lines) and equivalent potential temperature (K, colour shaded) at 850 hPa. Thick black lines in (a) and (d) show the flight pattern of the DLR Falcon. The solid part indicates the section of collocated lidar measurements.

The weather situation over the western North Pacific at 00 UTC 19 September 2008, at about the time of the measurements, is characterized by an upper-level trough with a distinct wind maximum at 500 hPa that approached northern Japan (Figures 5.1(a)). Further downstream of the trough, a broad ridge extended over large parts of the Northern Pacific Ocean. The location of the TC Sinlaku south of Japan can be recognised by the geopotential height contours at 500 and 850 hPa. Figure 5.1(d) shows that the flight was located in-between the tropical and the extratropical cyclone. On the leading edge of the midlatitude trough, warm and moist air was advected northeastward as confirmed by the high values of θ_e. Sharp gradients in θ_e to the east and north of the cyclone centre indicate the cold and warm front associated with the evolving cyclone. The flight crossed the tongue of increased θ_e values and reached tropical airmasses at the end of the flight northeast of TC Sinlaku.

Twelve hours later, at 12 UTC 19 September 2008, the trough at 500 hPa propagated eastward as shown by the geopotential height field in Figure 5.1(b).

During that time the cyclone slightly intensified (decreasing geopotential height at 850 hPa in Figure 5.1(e)). Additionally, the warm and moist air moved north-eastward and the frontal zone (strong θ_e gradient; Figure 5.1(e)) further deformed. Another 12 hours later, at 00 UTC 20 September, a separated cut-off low formed at 500 hPa and the cyclone deepened at 850 hPa (Figure 5.1(c) and (f)). Figures 5.1(d) to (f) indicate an eastward movement of the TC Sinlaku as well as the midlatitude trough during 24 hours.

Figure 5.2 shows visible satellite imagery of the geostationary Multi-functional Transport Satellite (MTSAT). A few hours before the observations, at 00 UTC 19 September 2008, Figure 5.2(a) depicts the cloud system of TC Sinlaku and its upper-level outflow indicated by the high level clouds around the storm centre (see also Figure 5.1(a) and (d)). Dense high-level clouds formed along the warm front of the midlatitude cyclone north of Japan. In the southwest of the low, convective clouds are visible along the cold front (compare with location of the θ_e gradients in Figure 5.1(d)). East of Japan, in between the tropical and midlatitude cyclone almost cloud free conditions prevailed in the area where the flight took place some hours later. The aircraft reached convective clouds northeast of the tropical storm at the end of the flight.

TC Sinlaku moved eastward during the next 24 hours (Figure 5.2(b)). The midlatitude cyclone intensified and propagated eastward and the centre of the occluded frontal system is located south of Kamchatka (compare with Figure 5.1(c) and (f)).
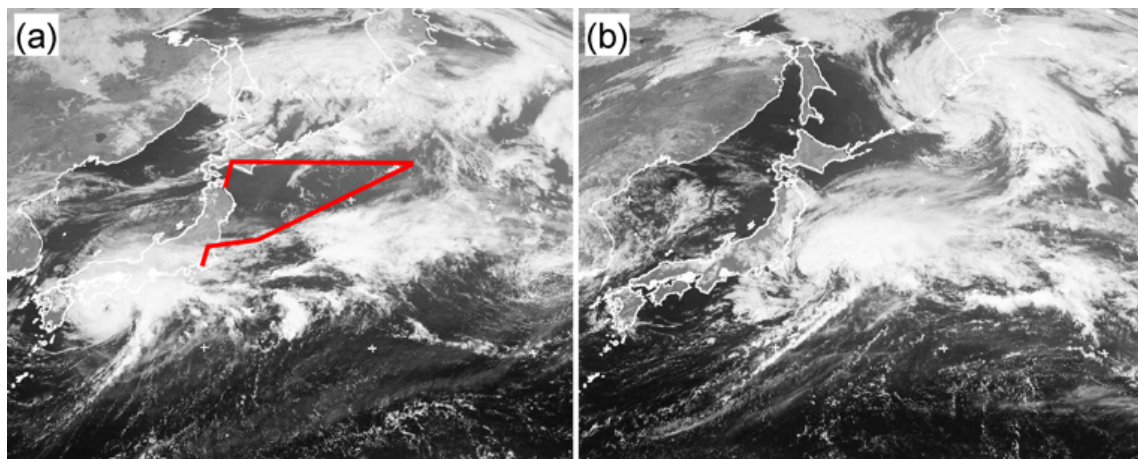
Figure 5.2: MTSAT satellite imagery (VIS, Chanel 1) at (a) 00 UTC 19 September and (b) 00 UTC 20 September 2008 (from NERC Satellite Receiving Station, Dundee University, Scotland, http://www.sat.dundee.ac.uk). Red line indicates the flight track.

5.2   Water vapour and wind observations

Lidar observations of BSR, specific humidity and wind speed for the flight segment described in the previous section are illustrated in Figure 5.3 superimposed with ECMWF analysis fields. BSR (Figure 5.3(a)) and specific humidity (Figure 5.3(b)) were observed with the DIAL for ∼3 hours between 0135 and 0440 UTC. The section with lidar observations is indicated by the solid black line in Figure 5.1(a) and (d). Wind observations (Figure 5.3(c)) are available from 0200 to 0420 UTC. Apart from the short part over northern Japan at the beginning of the flight (indicated by the topography in Figure 5.3) the ∼2300 km long flight mainly took place over the Pacific Ocean. The turning point near 154°E was reached at about 850 km distance.

The BSR shows cloud free conditions in the area between the midlatitude and tropical cyclone before 0340 UTC. After that, the BSR signal is disturbed by upper-level clouds related to deep convection northeast of TC Sinlaku that are observed until the end of the flight (note the vertical stripes in the BSR distribution below the upper-level clouds in Figure 5.3(a)). In the free troposphere, low aerosol contents (BSR < 2) are found except an elevated aerosol layer (BSR ≈ 5) which is located above 9 km altitude between 0145 and 0230 UTC. Beneath the clean air, a vertical BSR gradient indicates the transition to a different airmass. The upper edge of this layer increases from 3 km at the start of the cross section to 4.5 km at the turning point and, similarly, decreases on the southwestward oriented part of the flight to about 3.5 km when the cloudy region is approached at a distance of ∼1600 km. The BSR comprises complex structures with different layers containing variable BSR ratios. The first 200 km show a well mixed layer with a sharp vertical gradient on top that is most likely related to convective mixing over land. Low- and mid-level clouds appear at a distance of ∼500 km in an area of enhanced θ_e values (Figure 5.1(d)), that suggest reduced stability. Close to the sea surface, the maritime boundary layer is visible by increased BSR values (∼20-50) up to an altitude of ∼500 m.

Figure 5.3(b) illustrates the observed water vapour field which indicates a moist layer coinciding with the layer of enhanced aerosol. The upper edge of this layer is characterized by a strong vertical humidity gradient that is less sharp in the first part of the flight, where higher humidity values (∼1 g kg^{-1}) are observed up to about 6 km altitude before ∼0200 UTC. On the southwesterly oriented part of the flight the vertical humidity gradient (at ∼4 km altitude) is very strong and the specific humidity decreases from ∼3 g kg^{-1} to ∼0.1 g kg^{-1} in a vertical layer of ∼1 km. The modelled ECMWF moisture fields shown by the black contour lines in Figure 5.3(b) follow the colour grades of the lidar observations which implies qualitatively good agreement (a quantitative comparison follows in section 5.4). At the end of the
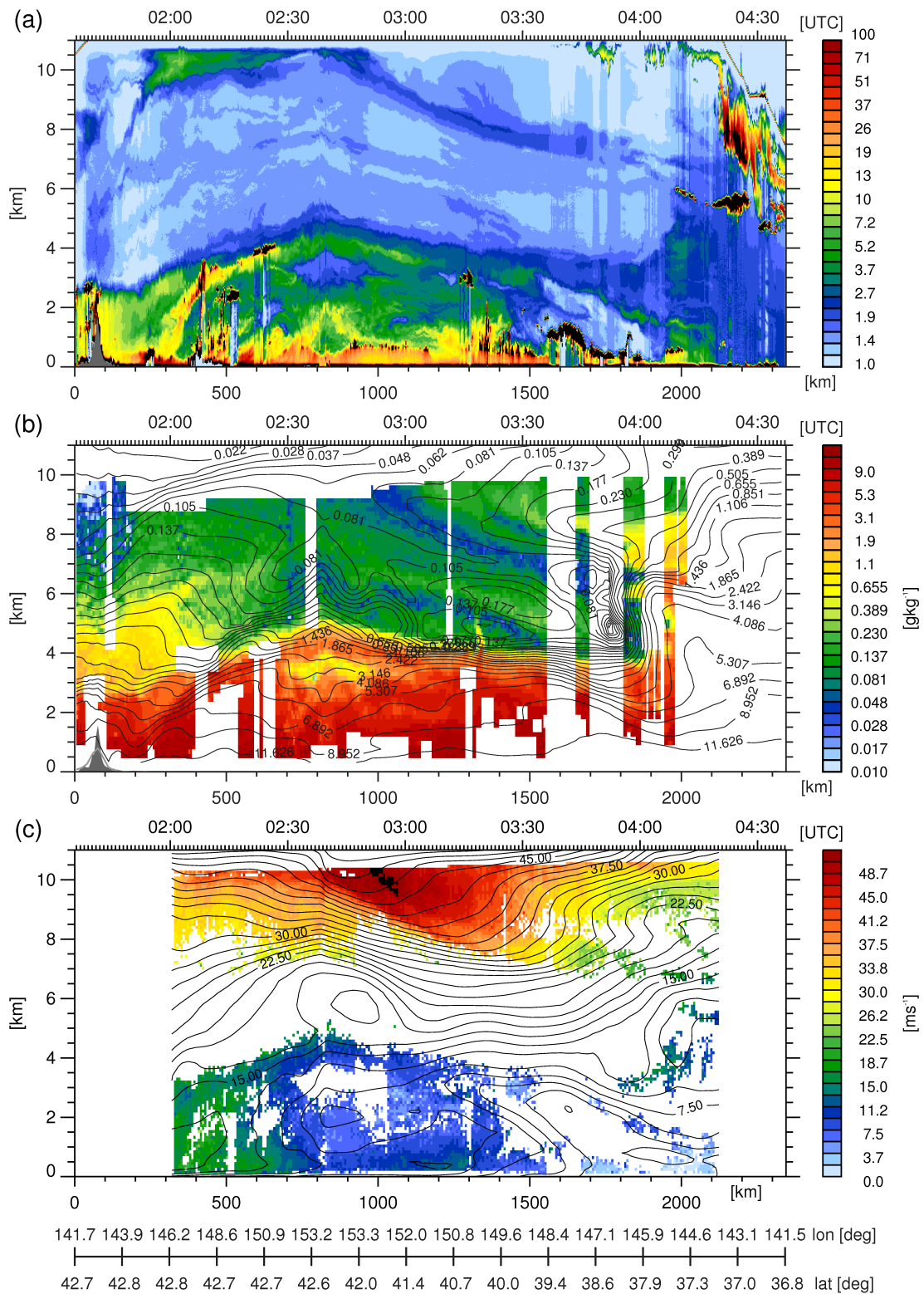
Figure 5.3: Lidar measurements on 19 September 2008: (a) BSR at 1064 nm in logarithmic scale; (b) specific humidity q (g kg^{-1}) in logarithmic scale, superimposed with contour lines of ECMWF data; and (c) horizontal wind speed (m s^{-1}), superimposed with ECMWF isotachs. Dark grey areas show the topography interpolated from GLOBE-DEM (Hastings et al. 1999), the light grey line marks the topography interpolated from the ECMWF model.

flight and close to the convective region at ∼0400 UTC the observed and simulated moisture indicates high moisture values in the upper troposphere (up to 1 g kg^{-1} at 8 km altitude).

Figure 5.3(c) depicts the observed and simulated wind speeds. The low mid-level aerosol content reduces the backscatter intensity and causes low data coverage between ∼4 and 8 km altitude. Close to the aircraft where the signal power is high, an upper-level wind maximum with wind speeds up to 50 m s^{-1} is observed on the southwestward oriented flight section right after the turning point (at a distance 850 km) that is associated with the midlatitude jet stream and also reproduced by the ECMWF simulations. In the moist and aerosol-rich layer close to the ground, the observations and simulations indicate low wind speeds that decrease towards the end of the flight.

5.3   WCB observations

Analogous to the case study in chapter 4, air parcel trajectories are started from every observation point on the lidar cross section to identify measurements that encounter WCB airmasses. An 8-day combined trajectory is composed of a backward part that represents the transport in the 2 days before and a forward part that depicts the 6 days after the observations. These trajectories are analysed for the maximum pressure decrease (maximum ascent) Δp_{max} in 48 hours (Figure 5.4(a)). Figure 5.4(b) shows the time lag of the ascent relative to the time of the observation. During the second part of the flight (after 0320 UTC) mainly convectively driven lifting near TC Sinlaku is observed. For reasons of comprehensibility the parcels are coloured grey and neglected in the following discussion of the structure of the WCB airmass. A coherent layer with a maximum depth of ∼4 km at 0200 UTC indicates an observed airmass that is part of a WCB and possesses maximum ascent rates of up to 650 hPa. Two maxima in the magnitude of the WCB ascent are located before and after the turning point. The mainly yellow coloured areas in Figure 5.4(b) show that the observed airmass rises immediately after the observation and, therefore, the inflow region of a WCB in advance of the strong ascent was detected.

Figure 5.5 shows the transport pathways of the observed WCB airmass start-ing ∼50 h before (Figure 5.5(a)) and ending ∼142 h after the observations (Figure 5.5(b)) as well as the evolution of pressure, humidity and potential temperature along the respective trajectories (Figure 5.5(c), (d) and (e)). The combined tra-jectories start at 00 UTC 17 September (00 h time mark) and end at 00 UTC 25 September 2008 (192 h). The time of the observations is indicated by the grey
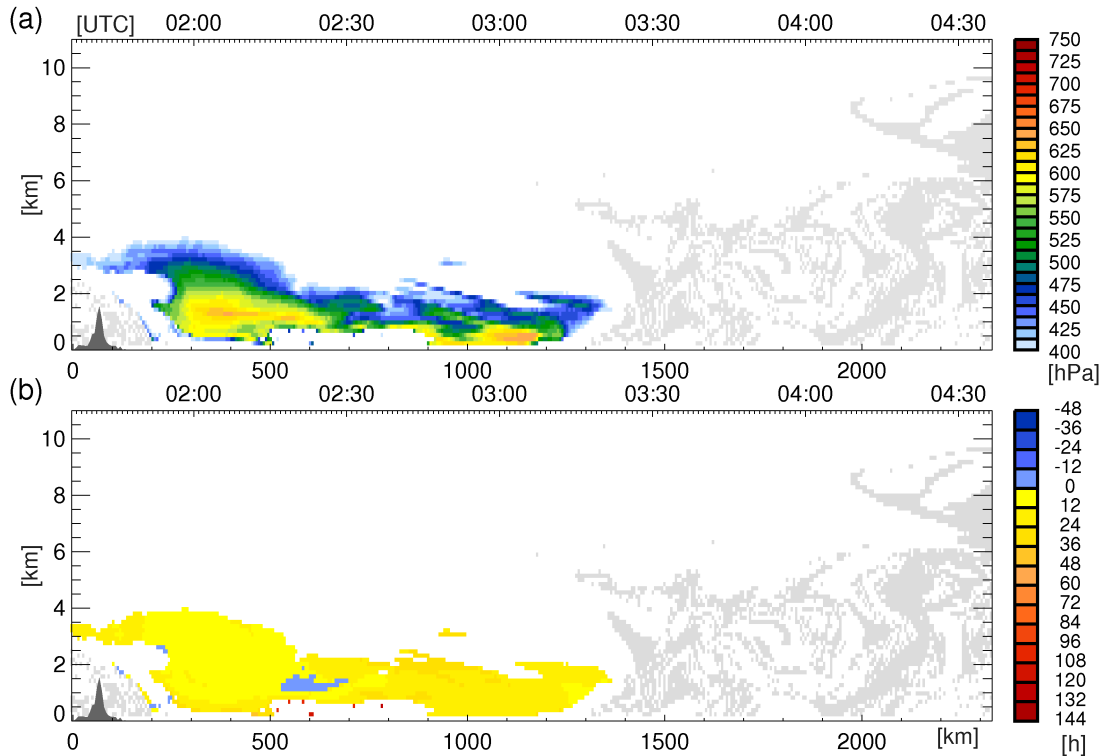
Figure 5.4: Locations of lidar observations with an ascent larger than 400 hPa in 48 hours. (a) Magnitude of the maximum decrease of pressure Δp_{max} (hPa) in 48 hours; (b) start time of the ascent (in hours relative to the observation time). Grey areas indicate ascents larger than 400 hPa associated with convective transport. For the method to calculate the trajectories see section 3.2.2.

bar in Figures 5.5(c), (d) and (e) to the right of the 48 hour time mark (00 UTC 19 September 2008). The trajectories are coloured according to the pressure at the observation time (see pressure in Figure 5.5(c) at ∼50 h). Blue colours indicate observations at higher altitudes whereas red colours belong to the lowest observations. At the observation time the moisture content of the trajectories varies from ∼1 to 12 g kg^{-1} (Figure 5.5(d)) and the potential temperature of the trajectories ranges between ∼292 and 310 K (Figure 5.5(e)).

At high altitudes (blue trajectories) the air is advected from westerly directions over China (see Figure 5.5(a)). Going to lower altitudes the advection of the observed airmass veers from southwesterly (green) to southeasterly directions at the lowest levels (yellow and red trajectories). The WCB airmass is mostly advected horizontally towards the measurement location.

After the observations, the WCB airmass moves coherently northeastward and passes Kamchatka to the east before the trajectories disperse horizontally and vertically and move anticyclonically to the east (see Figure 5.5(b)). The rapid ascent after the observations confirms that the observations were made in the inflow of a WCB. Figure 5.5(b) also depicts that the upper part of the WCB observations (green and blue trajectories) ascends earlier compared to the lower ones which leads
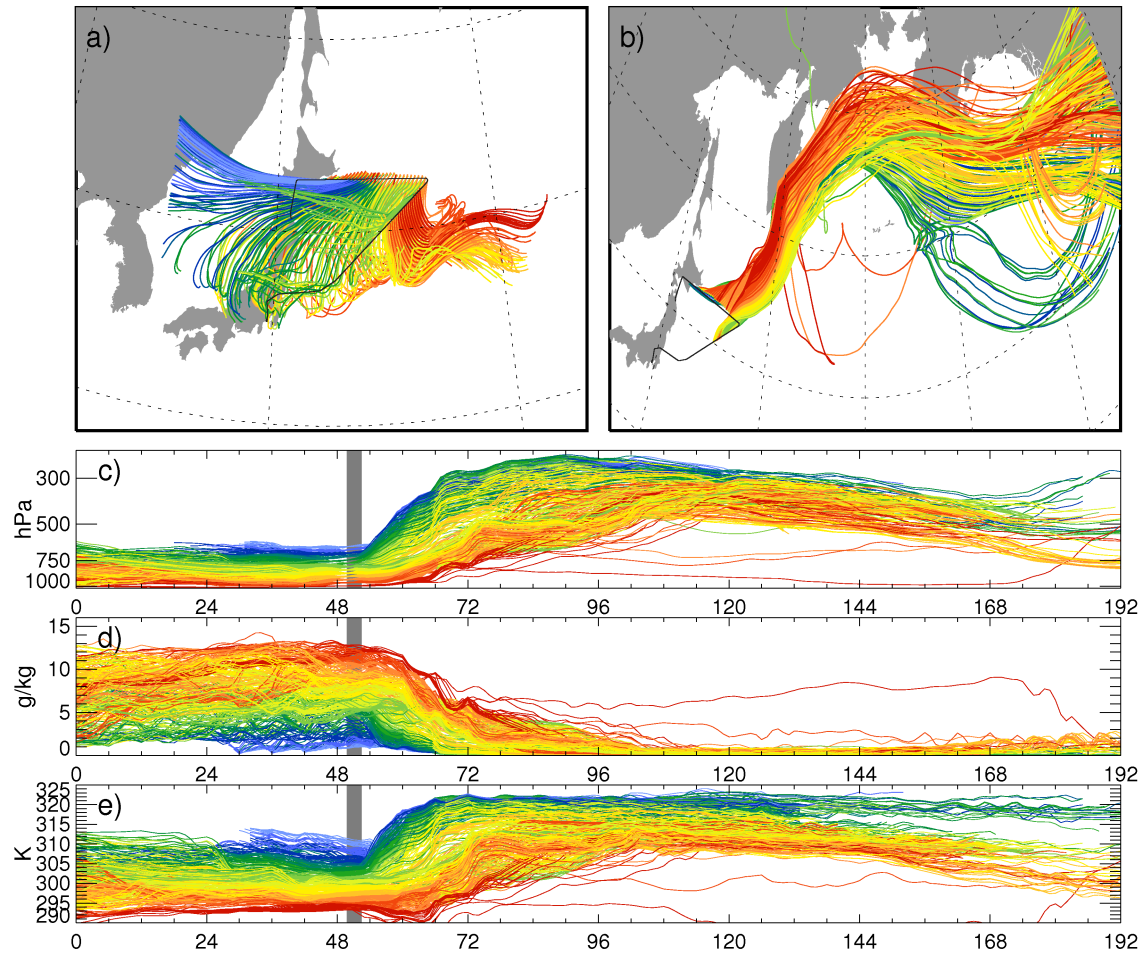
Figure 5.5: WCB trajectories ascending more than 400 hPa in 48 hours. Trajectories are colour-coded in dependence of the pressure at the time of the observation. (a) WCB trajectories in advance and (b) after the observations. Black line in (a) and (b) indicates the flight track. Temporal development of (c) pressure, (d) specific humidity and (e) potential temperature. Time (in h) is relative to 00 UTC 17 September 2008. For a clear overview every second trajectory in the vertical and every fourth in the horizontal direction are shown. For the method to calculate the trajectories see section 3.2.2. The grey bar in (c), (d) and (e) indicates the time of the lidar observations.

to a vertical dispersion. Additionally, the faster rising trajectories are lifted to higher altitudes and show a stronger anticyclonic curvature with a transport that is located further south. The trajectories feature a slight descent on the rear side of the trough in the anticyclonic outflow and further downstream. This descent is accompanied by a decrease in potential temperature which can probably be explained by radiative cooling (see also discussion in section 2.2.3). At the end of the 8-day period, the trajectories are embedded in an upper-level trough to the east of the North American west coast. The condensational processes in the WCB ascent cause a loss of initial moisture (see Figure 5.5(d)) and also an increase of potential temperature due to latent heating (see Figure 5.5(e)). The most humid trajectories lose about 12 g kg^{-1} and increase their potential temperature by ∼20 K.

Figure 5.6 depicts (a) the potential temperature evolution, (b) Δp_{max} in 48 hours as well as (c) the pressure and (d) the humidity evolution along the WCB trajectories. Figure 5.6(a) and (c) confirm the transport towards the flight path from easterly directions at higher levels ($\sim$700 hPa) and at higher potential temperatures ($\sim$310 K). The transport veers to southerly directions towards the sea surface associated with a transport of more humid airmasses. The condensational processes that characterize the WCB ascent occur south and east of Kamchatka as indicated by a strong increase of potential temperature and decrease of moisture (Figure 5.6(a) and (d)).
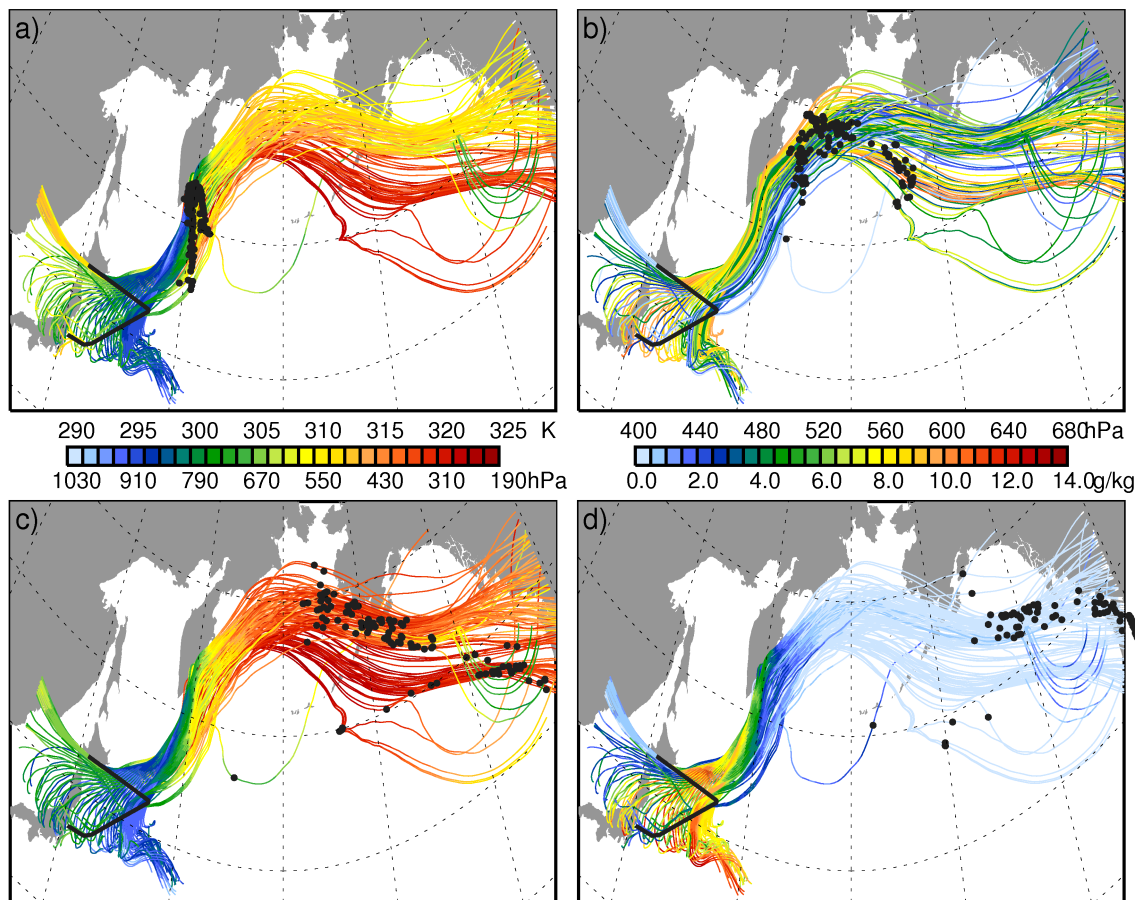
Figure 5.6: WCB trajectories ascending more than 400 hPa in 48 hours. Colour coding in upper row depends on (a) potential temperature along the trajectory and (b) maximum pressure decrease Δp_{max} in 48 hours. The bottom row is colour-coded in dependence of (c) pressure and (d) moisture content at the parcel positions along the respective trajectory. Black dots indicate position for (a) 00 UTC 20 September (corresponding to the 72 h time mark in Figure 5.5(b)), (b) 00 UTC 21 September, (c) 00 UTC 22 September and (d) 00 UTC 23 September 2008. For a clear overview every fifth trajectory is shown.

The parcel positions indicated in Figure 5.6(a) and (b) for 00 UTC 20 and 21 September south and east of Kamchatka corroborate that the latent heat release mainly takes place in the first 2 days after the observations (see also trajectories in the period from 48 to 96 h in Figure 5.5). Figure 5.5 shows that the early ascending parcels (observed at higher altitudes) are transported further south after having reached the outflow stage after ∼2 days. Figures 5.6(a) and (c) depict that the southerly transport proceeds at higher altitudes (∼280 hPa) and higher potential temperatures (∼320 K) compared to the northern part (∼350 hPa, ∼310 K). Figure 5.6(b) indicates that the ascending parcels in the western and central part of the WCB possess the largest vertical displacement in 48 hours (up to ∼650 hPa). Note that these parcels are the closest to the cold front and to the cyclone centre. In the outflow region the strongest rising parcels are distributed in both transport ways. All parcels are located in the anticyclonic outflow or are advected further eastward within the jet stream three days after the observations at 00 UTC 22 September (see Figure 5.6(c)). On the rear side of a downstream trough parcels steadily descend. At 00 UTC 23 September 2008, four days after the observations most of the WCB parcels are advected over the North American continent (Figure 5.6(d)).

5.4   Differences between ECMWF data and lidar observations

Figure 5.7 shows the difference between the ECMWF model data and the lidar observations for (a) specific humidity and (b) horizontal wind speed along the lidar cross section. In the moist layer below ∼4 km (see Figure 5.3(b)) strong positive moisture deviations indicate an overestimation of the humidity by the model. The deviations reach up to 7 g kg^{-1} and are located in the region where strong ascent within the WCB occurs afterwards. Based on Figure 5.4, an approximated inflow region is defined (blue rectangle in Figure 5.7) below 2.5 km altitude. Averaged over this inflow region, the mean moisture bias is ∼1.4 g kg^{-1} (19 %). The absolute deviations are smaller at low moisture contents in the upper troposphere.

The wind speed deviations in the moist layer and the approximated WCB inflow region show positive deviations up to 7 m s^{-1} at the turning point of the aircraft (at a distance of ∼850 km), i.e. an overestimation of the wind speed. At the beginning of the wind observation period, the deviations are negative (up to -6 m s^{-1}). In the upper troposphere, increased positive and negative deviations occur at the strong horizontal and vertical wind speed gradient which are most likely caused by a positional shift of the upper tropospheric jet stream.
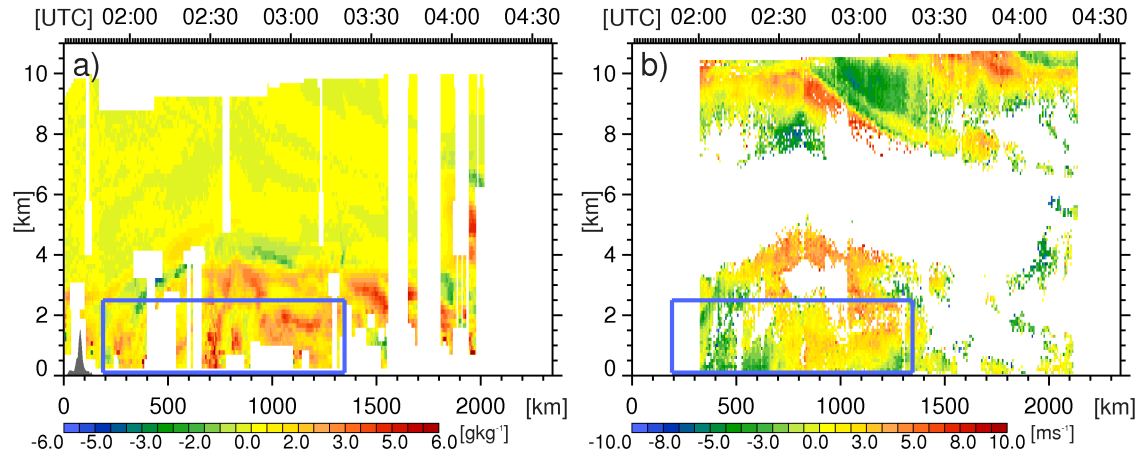
Figure 5.7: Absolute differences of ECMWF model fields and lidar observations on 20 September 2008 of (a) specific humidity and (b) horizontal wind speed. Blue rectangle indicates the approximated WCB inflow region. Dark grey areas show topography interpolated from GLOBE-DEM (Hastings et al. 1999).

5.5 Impact of moisture errors in the WCB inflow

In the following section, the influence of changed initial conditions in the WCB inflow region on the forecast of the WCB ascent and the associated cyclone will be discussed. At first, section 5.5.1 shows how the assimilation affects the humidity fields of the analysis. Section 5.5.2 elaborates the impact on the WCB forecast.

5.5.1 Impact on the analysis

Two data-assimilation experiments with the ECMWF IFS are performed: first, the control experiment (CTRL) uses all conventional data and secondly, the DIAL experiment additionally assimilates the DIAL observations to reduce the moisture bias in the WCB inflow region. In this way, two different analyses at 00 UTC 19 September 2008 were generated which provide the initial conditions for two different forecast experiments. Figure 5.7 shows the differences of the observed moisture and the analysis that was generated by assimilating all conventional data (CTRL). Conversely, the differences in Figure 5.8 are calculated with the analysis of the DIAL experiment that assimilated the additional DIAL observations.

The comparison of Figure 5.7 and 5.8 shows that the moisture along the lidar cross section is modified by the assimilation of the DIAL observations. The moisture bias between the model and observations in the inflow region decreased from 1.4 g kg^{-1} to 0.3 g kg^{-1} which means that the use of the DIAL data caused a reduction of the simulated humidity. This removal of moisture is equivalent to an improvement of the analysis, especially, in the up to 4 km deep layer with overestimated humidity. Note that also the wind analysis in the inflow region is improved
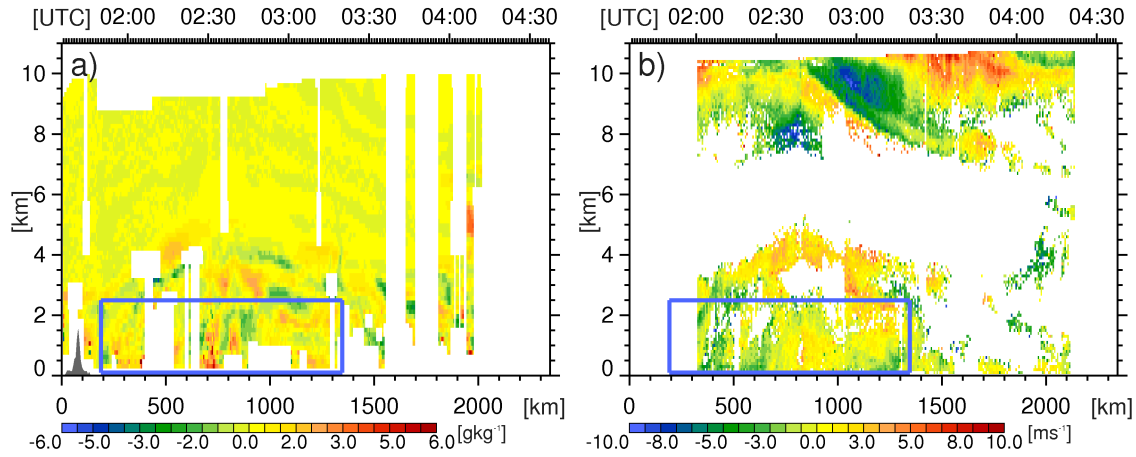
Figure 5.8: Absolute differences of ECMWF model fields (using DIAL data) and lidar observations on 20 September 2008 of (a) specific humidity and (b) horizontal wind speed. Blue rectangle indicates the approximated WCB inflow region. Dark grey areas show topography interpolated from GLOBE-DEM (Hastings et al. 1999).

as the deviations are reduced by assimilating only the moisture observations. At upper-levels the wind errors slightly increase.

Differences between moisture analysis and 12-h forecast at 850 hPa of the two assimilation experiments (DIAL - CTRL) are shown in Figure 5.9. Additionally, the geopotential height is shown for both experiments to visualise the effect on the midlatitude cyclone. The 850 hPa isobaric surface is located at ∼1500 m (see contour lines of the geopotential height close to the flight track) where the removal of moisture by the data assimilation is particularly strong (compare Figure 5.7 and 5.8) and located within the diagnosed WCB inflow region.
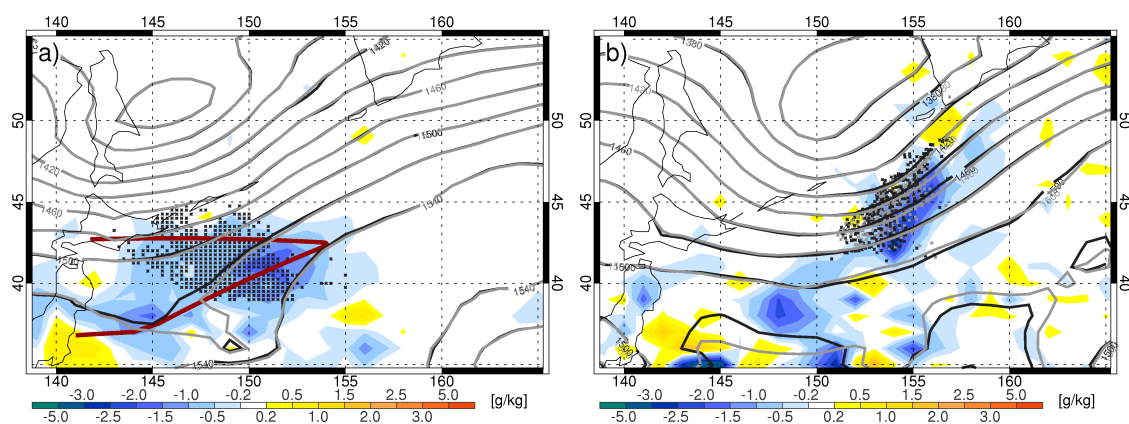
Figure 5.9: Absolute differences (DIAL - CTRL) of specific humidity (g kg^{-1}) for (a) the analysis at 00 UTC 19 September 2008 and (b) the +12 h forecast. Grey (CTRL) and black (DIAL) contour lines indicate the geopotential height at 850 hPa (in m). Positions of ascending WCB trajectories calculated with forecasts based on the DIAL (black dots) and CTRL (grey dots) analysis. WCB trajectories are parcels which are lifted from every grid point between sea surface and 700 hPa in an area from 142° to 155°E and 39° to 45°N by more than 500 hPa in 48 hours. Only parcels that are located in 850 ± 20 hPa are indicated.

At the time of the analysis, the centre of the midlatitude cyclone is located north of the flight path at 146°E/51°N (Figure 5.9(a)). The geopotential height contour lines of both analyses are very similar. Only small differences are observed south of 40°N where the gradient of the geopotential height is weak. Negative humidity differences confirm the reduction of moisture along the flight track and show that the moisture content is reduced in a broad region around the flight pattern. The maximum decrease of humidity (-2 g kg^{-1}) is located just north of the southwestward oriented flight leg. The DIAL data assimilation also affects the humidity in the tropical airmass as can be seen at the end of the flight.

Forward trajectories are calculated from the ground up to 700 hPa to assess the location of the WCB inflow and its position relative to the area of reduced moisture. The trajectory calculation is performed twice with model fields of the DIAL and the CTRL experiment to compare the representation of the WCB in both forecast experiments. In a first step, the WCB trajectories that ascended more than 500 hPa were identified in the CTRL forecast. Then trajectories using the DIAL forecast wind fields were calculated from the same starting points.

At the time of the analysis, the starting points of the WCB trajectories lie in a broad region around the flight track and on the southern part of the leading edge of the trough at 850 hPa (see black dots in Figure 5.9(a)). The WCB inflow region also coincides with the area of maximum humidity difference. As only trajectories that ascend more than 500 hPa are shown, no starting points are found close to the turning point of the aircraft where the maximum pressure decrease is lower (see Figure 5.4(a)). The coincidence of the moisture difference and the WCB inflow implies that a different amount of moisture is transported within the WCB of the two forecast experiments which may affect the cyclone shape and, subsequently, the upper tropospheric circulation.

During 12 hours of forecast time the trough at 850 hPa moves ∼5° eastward and the cyclone centre is located at ∼151°E/52°N (Figure 5.9(b)). The differences of geopotential height are small. However, on the leading edge of the trough a slight difference of the 850 hPa geopotential height is apparent. Similarly, the area of large moisture differences is displaced northeastwards. WCB trajectories driven by the DIAL (black) and CTRL (grey) forecast wind fields are similar and both are still located in the area of maximum negative moisture deviations. The persistence of the difference signal during the first 12 hours can be explained by the almost horizontal transport and constant humidity values of the trajectories at 850 hPa (Figure 5.5(c)). Subsequently, these trajectories are lifted substantially.

5.5.2   Impact on the forecast

The following section will investigate how the changed initial moisture distribu-
tion changes the forecast of the WCB event, the evolution of the cyclone and the
downstream weather. Figure 5.10 illustrates the frequency distributions of the key
meteorological parameters in dependence of forecast lead time along the WCB tra-
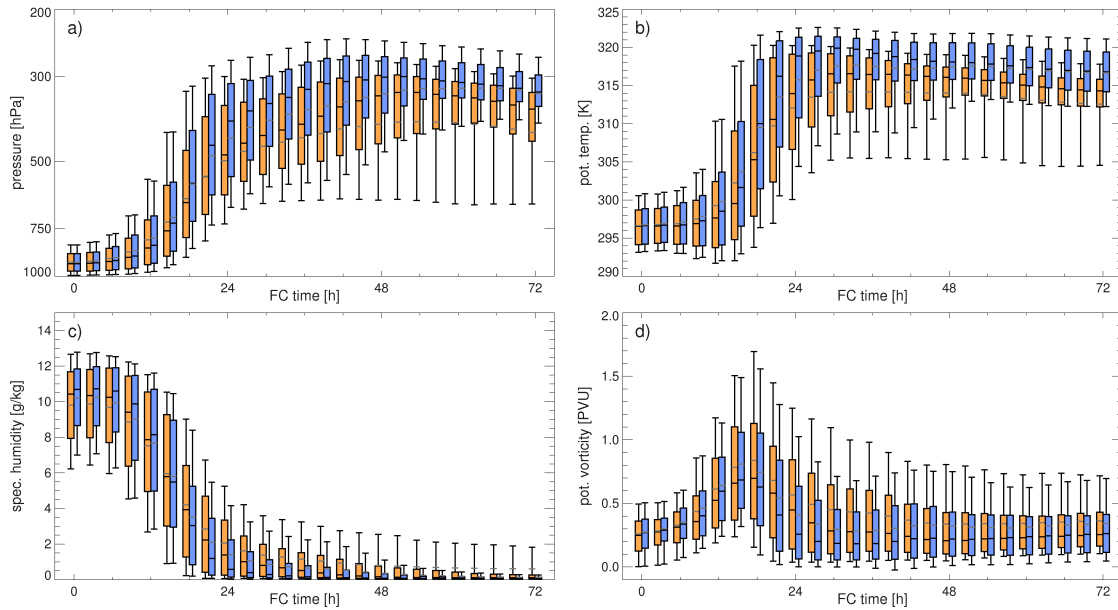jectories calculated with the CTRL and the DIAL forecast wind fields.

Figure 5.10: Statistical distribution of (a) pressure, (b) potential temperature, (c) specific humidity
and (d) PV for trajectories identified as WCB trajectories (ascent larger than 500 hPa) driven by
the CTRL (blue) and DIAL (orange) forecast wind fields and starting at the same positions at
00 UTC, 19 September 2008. The boxplot indicates the upper and lower quartile, the median
(black line) and the mean (grey) of the respective parameter. The whiskers indicate the 10th and
90th percentile.

Figure 5.10(a) shows the distribution of pressure for 3-hourly forecast time
steps up to +72 h. Both pressure distributions agree at the analysis time as all
trajectories start at the same location. The mean pressure of the WCB starting
points $\bar{p}_{CTRL,DIAL}(0\,\mathrm{h})$ is 920 hPa and the top most parcels start at 750 hPa. During
the first 12 hours, the parcels of both forecast experiments only ascend slightly
and possess similar, relatively narrow frequency distributions. However, it becomes
apparent that the parcels in the CTRL experiment are located somewhat higher than
in the DIAL forecast. This difference amplifies after 12 hours forecast time when
the parcels begin to ascend and disperse vertically. After 24 hours the mean WCB
trajectory reached the mid-troposphere and the mean WCB pressure of the CTRL
forecast ($\bar{p}_{CTRL}(24\,\mathrm{h}) = 435$ hPa) is 65 hPa lower compared to the DIAL forecast
($\bar{p}_{CTRL}(24\,\mathrm{h}) = 500$ hPa). Between 24 and 48 hours most WCB trajectories reach
the outflow stage with a considerably higher outflow of the WCB in the CTRL run

($\bar{p}_{CTRL}$(48 h) = 332 hPa, $\bar{p}_{DIAL}$(48 h) = 400 hPa). Some of the DIAL trajectories are first lifted, but they do not pass the mid-troposphere (see 10th percentile).

Figure 5.10(b) shows the distributions of potential temperature along the WCB. The parcels start at about the same potential temperature $\bar{\theta}_{CTRL,DIAL}$(0 h) $\approx$296.5 K. The moister CTRL run possess slightly higher θ-values. The ascent is associated with an increase of potential temperature, whereby the latent heating processes are strongest between 12 and 24 hours forecast lead time when the parcels are ascending to the mid-troposphere. The highest mean potential temperatures are reached after 33 hours ($\bar{\theta}_{CTRL}$(33 h) = 317.7 K and $\bar{\theta}_{DIAL}$(33 h) = 314.2 K) and show that the increase of potential temperature is 3.5 K larger in the initially moister CTRL forecast. Thus, the mean increase of potential temperature $\Delta\bar{\theta}$ is 21 K for the CTRL and 17.5 K for the DIAL forecast.

Figure 5.9 shows that the WCB trajectories start in the region of reduced moisture in the DIAL analysis which is reproduced by the moisture distribution at the time of the analysis (Figure 5.10(c)). The mean initial humidity at the starting points $\bar{q}$(0 h) is 9.8 g kg^{-1} in the DIAL analysis and 10.2 g kg^{-1} in the CTRL analysis. Note that the estimation of the θ increase due to condensational processes as presented in section 2.2.3 would result in a $\sim$1 K higher $\Delta\theta$ in the CTRL forecast. The higher difference of 3.5 K indicated by the presented trajectories can be explained by the part of the DIAL trajectories that does not pass the mid-troposphere and therefore shifts the mean of θ in the outflow to a lower value. During the first 12 hours, humidity only slightly decreases and on average the CTRL WCB trajectories remain moister. Between 12 and 24 hours, the CTRL trajectories lose their moisture more quickly because of the faster and stronger proceeding latent heat processes. The stronger lifting and diabatic heating lead to a higher outflow at lower moisture contents. This explains the moister DIAL parcels that are located in the mid and upper troposphere after 24 h.

Figure 5.10(d) shows the evolution of PV and clearly indicates the diabatically generated PV at lower levels which is highest between 12 and 24 hours. During the first 18 hours the moister CTRL trajectories produce larger values of PV at lower levels. After that time, the moister and additionally still lower DIAL trajectories generate PV for a longer time period whereas PV is again destroyed above the maximum level of latent heating in the CTRL run. The higher located CTRL trajectories possess lower PV values in the outflow region.

In summary, the forecast with the reduced moisture in the inflow of the WCB (DIAL) shows a weaker lifting and latent heat release at lower levels within the WCB ascent. The CTRL forecast shows a higher outflow which resulted in a larger reduction of moisture and increase of potential temperature. More PV is generated

below the level of maximum heating in the CTRL forecast. Above, the stronger lifting caused a higher reduction of PV and a transport of lower PV values in the WCB outflow.

Difference plots of geopotential height, sea level pressure (SLP) and PV are shown in the following to investigate the impact of the differing WCB forecasts on the cyclone and the downstream weather. Figure 5.11 shows the 500 hPa geopotential height and SLP differences at +24 h forecast time as well as the location of the WCB trajectories at the respective pressure level. The geopotential height differences on the leading edge of the trough at +12 h (see Figure 5.11(a)) also emerge at +24 h at 500 hPa as can be seen by the yellow coloured positive differences that represent higher geopotential heights in the DIAL forecast. This corresponds to a weaker cyclone development at 500 hPa in the forecast with reduced initial moisture that appears related to the weaker WCB as the trajectories are located directly in the region of largest geopotential height differences on the leading edge of the trough. At this time a large fraction of the trajectories reached the mid and upper troposphere (see Figure 5.10(a)) whereby the CTRL trajectories are lifted faster and therefore located higher. The parcels at ∼500 hPa remain coherently arranged south of Kamchatka in both forecast experiments. After 24 hours forecast time none of the
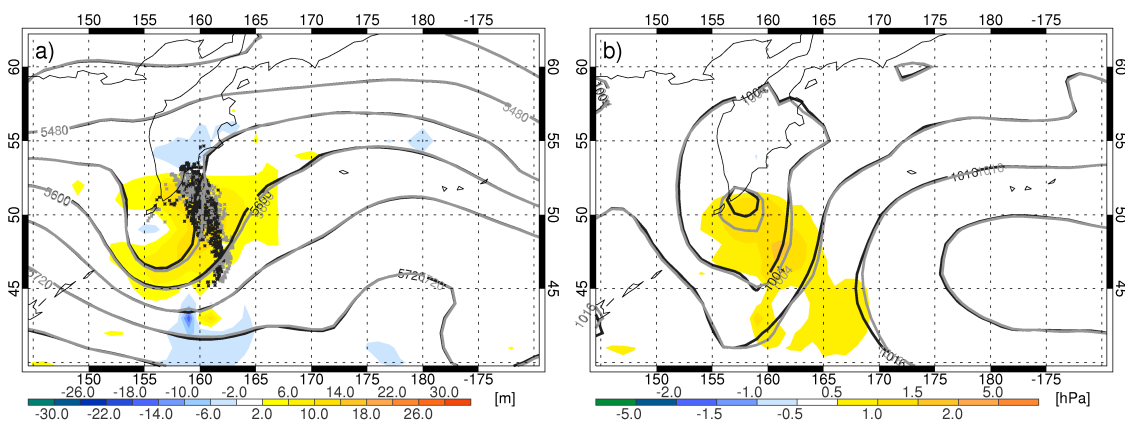
Figure 5.11: Differences (DIAL - CTRL) of (a) geopotential height at 500 hPa and (b) sea level pressure at +24 h (00 UTC 20 September 2008) forecast time. Grey (CTRL) and black (DIAL) contour lines indicate (a) the geopotential height at 500 hPa and (b) SLP. WCB positions in (a) are marked in 850 ± 50 hPa for the CTRL (grey dots) and DIAL (black dots) forecast.

WCB parcels are found close to the surface (Figure 5.11(b)). However, the weaker latent heat release and diabatically generated low-level PV in the early phase of the cyclone development also affected the low level circulation. Figure 5.11(b) shows an up to ∼2 hPa weaker surface cyclone in the DIAL forecast. The centre is located at the southern tip of Kamchatka slightly west of the ascending WCB.

During the next 12 hours, the majority of the parcels are lifted above 500 hPa and the release of latent heat decreases (see Figure 5.10(a) and (b)). At 12 UTC

20 September 2008 (+36 h) the cyclone begins to separate from the background flow at 500 hPa (see Figure 5.12(a)). The geopotential height differences expanded over the entire trough region and increased to values up to ∼20 m at 500 hPa. The trajectories that remain at ∼500 hPa are still coherent and are located to the north of the area of largest geopotential height differences. The majority of WCB parcels in 500 hPa belong to the weaker DIAL WCB (black dots) which confirms the higher pressure values of the DIAL forecast in Figure 5.10(a).
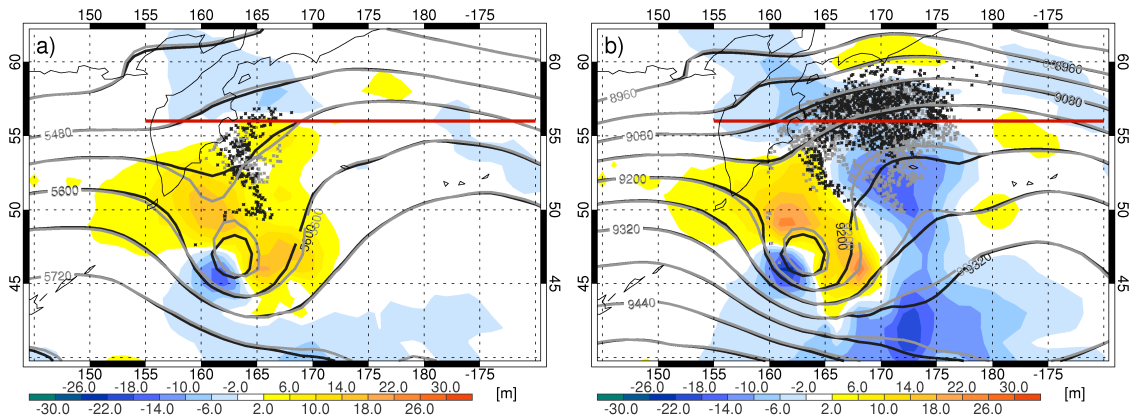
Figure 5.12: Differences (DIAL - CTRL) of geopotential height at (a) 500 hPa and (b) 300 hPa at 12 UTC 20 September 2008 (+36 h forecast time). Grey (CTRL) and black (DIAL) contour lines indicate the geopotential height at (a) 500 hPa and (b) 300 hPa. Positions of the WCB forecast are marked by grey dots for the CTRL and by black dots for the DIAL forecast. All positions in ± 10 hPa of the pressure level are marked. The red line shows the location of a vertical cross section shown in Figure 5.13.

The weaker cyclone in the DIAL forecast is also visible at 300 hPa (Figure 5.12(b)) with positive geopotential height differences up to ∼25 m. Additionally, the downstream ridge features negative differences. This means that the geopotential is higher for the CTRL forecast which possesses a higher WCB outflow. The relation of the stronger ridging to the stronger WCB is supported by the location of the WCB trajectories.

Figure 5.13 shows a cross section at 56°N at a forecast lead time of +36 h. The cross section extends from the western part of the ridge at 155°E to the eastern side at 190°E and intersects the WCB outflow and the area of negative geopotential height differences at 300 hPa (see red line in Figures 5.12(a) and (b)). The dashed and the solid line show the tropopause heights (2 PVU isoline) for both forecasts and the colour shading illustrates the differences between PV of the DIAL and the CTRL forecast. On the western side of the cross section, at the transition to the upper-level ridge (∼165°E; compare also with Figure 5.12(b)) the tropopause slightly ascends before it proceeds at a nearly constant pressure level of ∼210 hPa in the ridge and again slightly lowers at the eastern part of the cross section.

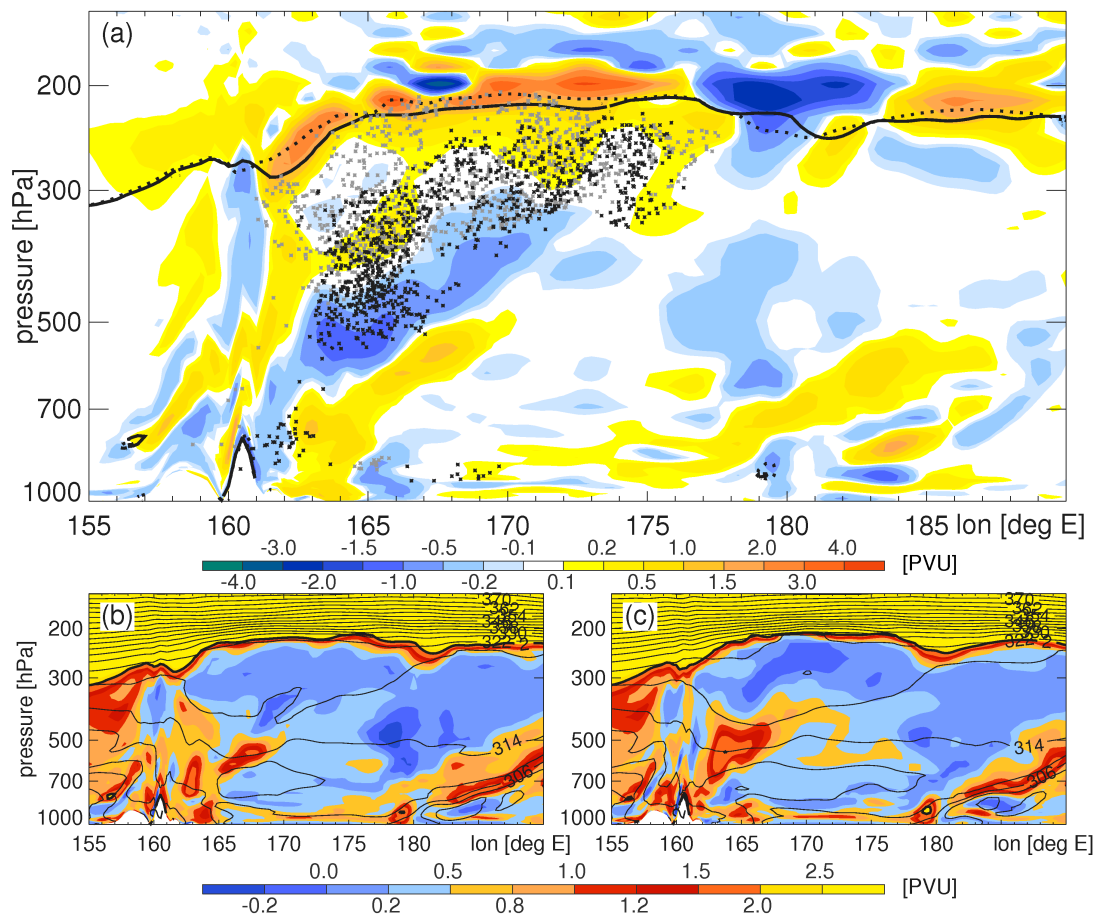Figure 5.13: Cross section at 56°N (see red line in Figure 5.12 a and b) at 12 UTC 20 September 2008 (+36h): (a) PV differences (DIAL-CTRL) (colour shaded areas) and 2 PVU isoline of DIAL (solid line) and CTRL (dashed line) forecast. (b) DIAL and (c) CTRL PV distribution (colour shaded areas) and potential temperature (black contour lines). WCB trajectories in (a) area indicated in ±0.5° latitude for the CTRL (grey dots) and DIAL (black dots) forecast.

The differences show a distinct region with positive values (up to 4 PVU) near the tropopause between 160° and 175°E which indicates a dynamical tropopause that is located ∼10 to 20 hPa (∼500 to 1000 m) higher in the CTRL forecast. The vertical displacement generates high differences because of the strong vertical PV gradient at the tropopause (Figures 5.13(b) and (c)). However, positive difference values between 0.1 and 0.5 PVU are also observed below the tropopause. Large PV differences are found in the diabatically active region on the leading edge of the trough in the mid-troposphere between 160° and 170°E. The CTRL forecast possesses higher PV values at 500 hPa compared to the DIAL forecast that depicts a less homogeneous PV maximum that is slightly shifted to the east.

The location of the WCB trajectories at upper-levels and in an area of low PV values corroborates the importance for the downstream ridge and the location of the tropopause. The fact that the CTRL trajectories (grey dots) are located at higher

altitudes suggests that the stronger outflow in the CTRL forecast lifts the local tropopause. The slightly positive values below the tropopause (at ∼300 hPa) in the ridge between 160° and 180°E (compare also the PV structure in Figures 5.13(b) and (c)) coincide with the WCB outflow. The differences at lower levels are most likely related to the impact of the WCB at earlier forecast times on the cyclone that resulted in a different structure and intensity of both forecasts (Figure 5.12(a)).

The impact of the different WCB outflow strength on the structure of the tropopause at +36 h is also illustrated in Figure 5.14 which shows PV at the 322 K isentropic surface for (a) CTRL and (b) DIAL forecast. Poleward, PV increases as
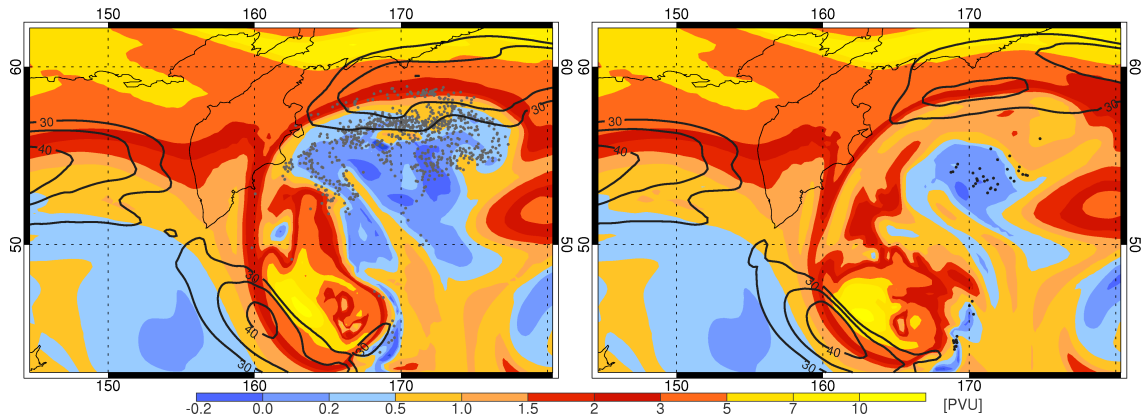
Figure 5.14: PV (colour shading, PVU) and wind speed (m s^{-1}) on the 322 K isentropic surface at 20 September 2008 12 UTC (+36 h) for (a) CTRL and (b) DIAL forecast. Trajectory positions are marked by grey dots in (a) for the CTRL and by black dots in (b) for the DIAL forecast. All positions in ±0.5 K of the isentropic level are marked.

the middleworld isentropic surface enters the stratosphere in both forecasts. The trough emerges as a PV streamer with high PV values propagating southward. The main difference in the PV distribution is found in the downstream ridge, where a broad region of low PV values emerges in the CTRL forecast (blue coloured areas) whereas the DIAL forecast shows only a small area with PV < 0.5 PVU. The connection to the WCB outflow is confirmed by the location of the WCB trajectories in the area of low PV at 322 K. The CTRL forecast shows a large amount of parcels whereas the DIAL forecast shows only a few at 322 K. The weaker outflow in the DIAL forecast is associated with a weaker isentropic PV-gradient near the tropopause and also with weaker wind speeds in the jet stream as can be seen by comparing the black contour lines in Figure 5.14(a) and (b) at ∼60°N. Along the PV gradient the wind speed is decreased by 3-6 m s^{-1} (5-15 %) due to the assimilation of the DIAL data.

At 00 UTC 21 September 2008 (+48 h forecast time) the geopotential height differences at 500 and 300 hPa between the DIAL and CTRL forecast further increased (compare Figures 5.12 and 5.15). Beside the trough centre, where the geopotential

height at 300 hPa is more than 30 m higher (positive values) in the DIAL forecast, the downstream ridge shows stronger pronounced, however, negative geopotential height differences. The trajectory positions at 300 hPa indicate the downstream advection of the WCB parcels with the jet stream. However, parts of the originally lifted airmass are still located in this region of negative differences. Most of the trajectories are lifted above 500 hPa (see Figure 5.15(a)) and only a few trajectories (mainly DIAL) remain in the mid-troposphere north of the trough at around 168°E.
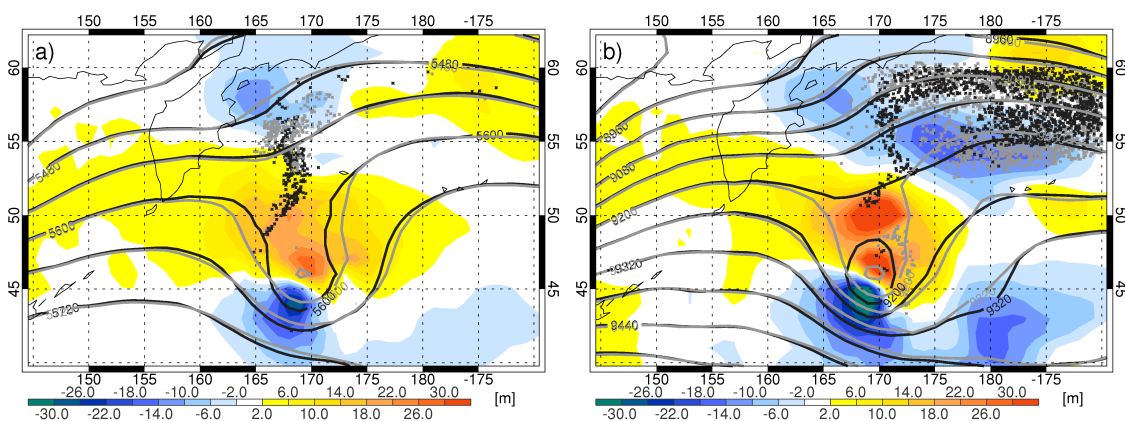
Figure 5.15: as in Figure 5.12 but for +48 h forecast time.

5.5.3   Impact on forecast skill

The foregoing section showed how the reduced low-level moisture in the initial conditions affected the forecast of the WCB. This section will investigate the skill of the forecast verified against analysis fields. The metrics presented in section 3.2.1 are used to analyse the temporal and spatial evolution of the forecast impact.

Figure 5.16 shows the improvement of the forecast in terms of vertically averaged PV and kinetic energy of the system after 24 hours. Improvement means a reduction of the forecast error of a variable or error norm in the DIAL forecast compared to the CTRL forecast (see also section 3.2.1). The vertically averaged PV between 550 and 900 hPa is chosen to illustrate the impact of the differing latent heating on the PV structure at low- to mid-levels. An impact on the averaged PV is visible in the cyclone centre and north of the surface warm front with alternating positive and negative values (see also Figure 5.1(f) for the location of the fronts). More pronounced and predominantly negative values are found on the leading edge of the trough east of the surface cold front in the region where the WCB air ascends. The negative values indicate an improvement of the vertically averaged PV in the DIAL forecast. At the same time the kinetic energy norm which is composed of winds at
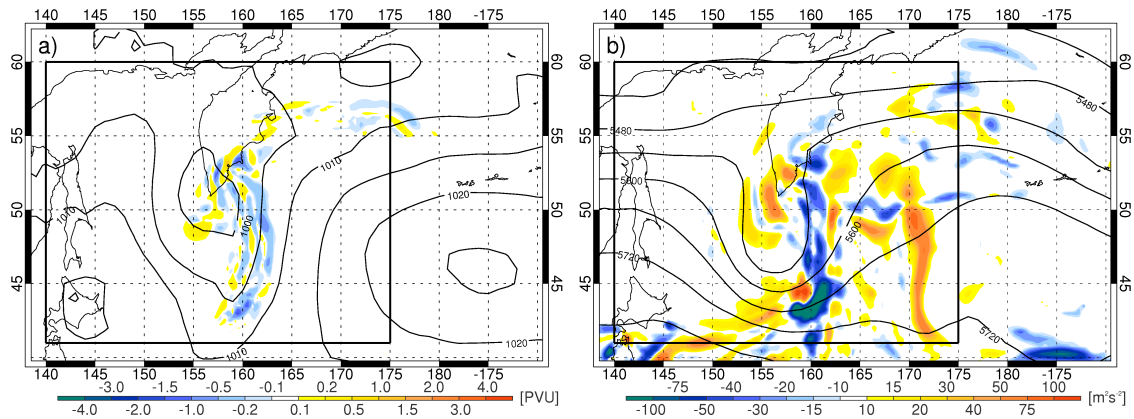
Figure 5.16: Forecast impact at 20 September 2008 (+24 h) in terms of (a) 550 to 900 hPa vertically averaged PV-Norm and (b) kinetic energy norm. Contour lines show geopotential height of the ECMWF analysis at 850 hPa (a) and 500 hPa (b). Black rectangle around the trough indicates the region (140° to 175°E and 41° to 60°N) used for averaging in Figure 5.17.

850, 500 and 250 hPa indicates positive and negative values of the same magnitude in and around the trough. However, an improvement of the dynamical structure in the DIAL forecast is found on the leading edge of the trough at about the same location where PV is improved.

The connection between the improvement of PV and the kinetic energy is further investigated by analysing the temporal evolution of averaged impact values in the box indicated in Figure 5.16. The box was selected between 140° to 175°E to cover the entire trough region over a forecast period of 48 h which is the main latent heating phase of the WCB. Figure 5.17 shows spatially averaged values of vertically averaged PV and kinetic energy. The averaged impact in terms of vertically averaged PV
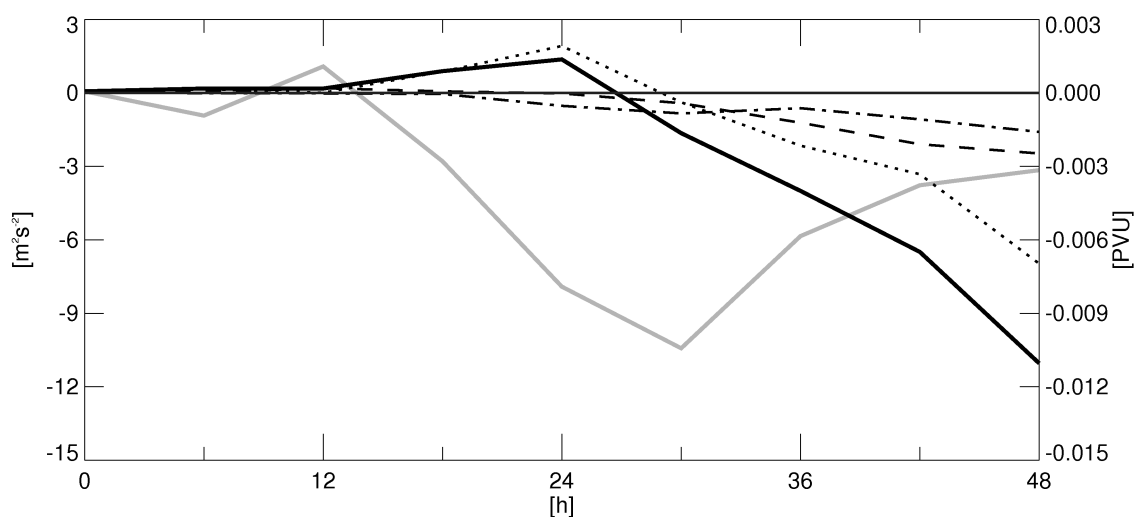

Figure 5.17: Averaged forecast impact in terms of 550 to 900 hPa vertically averaged PV-Norm (solid grey line) and kinetic energy norm (solid black line) consisting of contributions from 250 hPa (dotted), 500 hPa (dashed) and 850 hPa (dash-dotted black line). The impact is averaged in the area from 140° to 175°E and 41° to 60°N (see black rectangle in Figure 5.16).

(grey solid line) is neutral during the first 12 hours in which both forecasts showed relatively small differences in the moisture content and pressure (see Figure 5.10). After ~12 h the latent heat release begins to increase which is accompanied by negative values of the PV impact increasing up to +30 h. Consequently, the reduced moisture in the WCB inflow of the DIAL experiment results in an improvement of the PV structure at lower levels. The PV impact slightly decreases between +30 and +48 h when the airmass reaches the WCB outflow and the diabatic processes weaken. At +24 h Figure 5.17 indicates an increased average PV improvement which reflects the distribution in Figure 5.16(a).

The kinetic energy norm (black solid line) shows an improvement with a time lag of about 12 hours. After +30 h the impact continuously increases. Figure 5.17 also illustrates the contributions of the different pressure levels (250, 500, 850 hPa) to the kinetic energy impact. At first the wind fields at 850 hPa show a slight improvement (dash dotted line) at +18 h. The improvement propagates vertically and emerges at 500 hPa at +24 h and at 300 hPa at +30 h. At +24 h the averaged kinetic energy is deteriorated which mainly results from the contribution of 250 hPa (see also large areas of negative impact in the downstream ridge in Figure 5.16(b)). The regions with negative values of the kinetic energy norm in Figure 5.16(b) are caused by an improvement of the wind fields at 850 hPa.

Minimum sea level pressure (MinSLP) is used to provide information about the intensity of the cyclone. The evolution of the MinSLP for both forecasts is compared with the analysis in Figure 5.18. Up to +18 h MinSLP in the analysis is almost constant (~999 hPa). In the period of the strongest ascent, the pressure decreases by about 2.6 hPa in 6 hours and the lowest value of the minimum surface pressure in the analysis is found at +24 h (996.4 hPa). Thereafter the surface pressure increases. Up
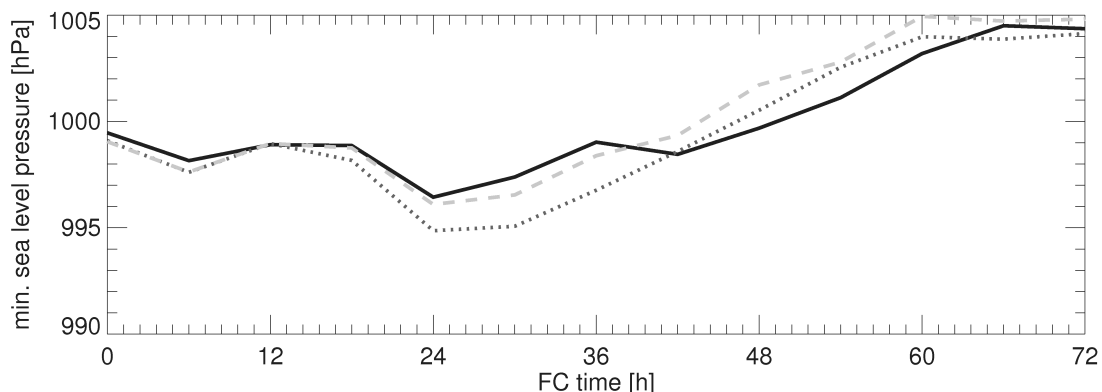

Figure 5.18: Minimum sea level pressure (MinSLP) of the surface cyclone in dependence of forecast time for analysis (solid black), DIAL (dashed light grey) and CTRL (dotted dark grey) experiment. The forecasts start at 00 UTC 19 September 2008.

to +12 h the forecast of the two experiments agree well. Between +12 and +24 h a

stronger surface cyclone develops in the CTRL forecast ($\text{MinSLP}_{CTRL} = 994.9$ hPa) than in the DIAL forecast ($\text{MinSLP}_{DIAL} = 996.43$ hPa) which is consistent with the findings of section 5.5.2. The higher MinSLP in the DIAL forecast is similar to the analysis. The difference of about 1.5 hPa between DIAL and CTRL forecasts remains constant up to +42 h. From the time the experiments diverge until +36 h, the DIAL experiment matches better with the analysed surface pressure minimum. After 48 hours the cyclone separates from the background flow and the minimum surface pressure weakens.

The following analysis focuses on how the modified WCB outflow affects the forecast skill at upper-levels and in which way this signal propagates downstream. Figure 5.19 shows the impact in terms of the geopotential height at 300 hPa from +48 to +84 h. The geopotential height of the analysis is shown by blue contours. At +48 h the cyclone is separated from the background flow and slightly narrows up to +60 h (Figure 5.19(a) and (b)). Thereafter, another trough approaches from west and the cyclone weakens (Figure 5.19(c) and (d)).
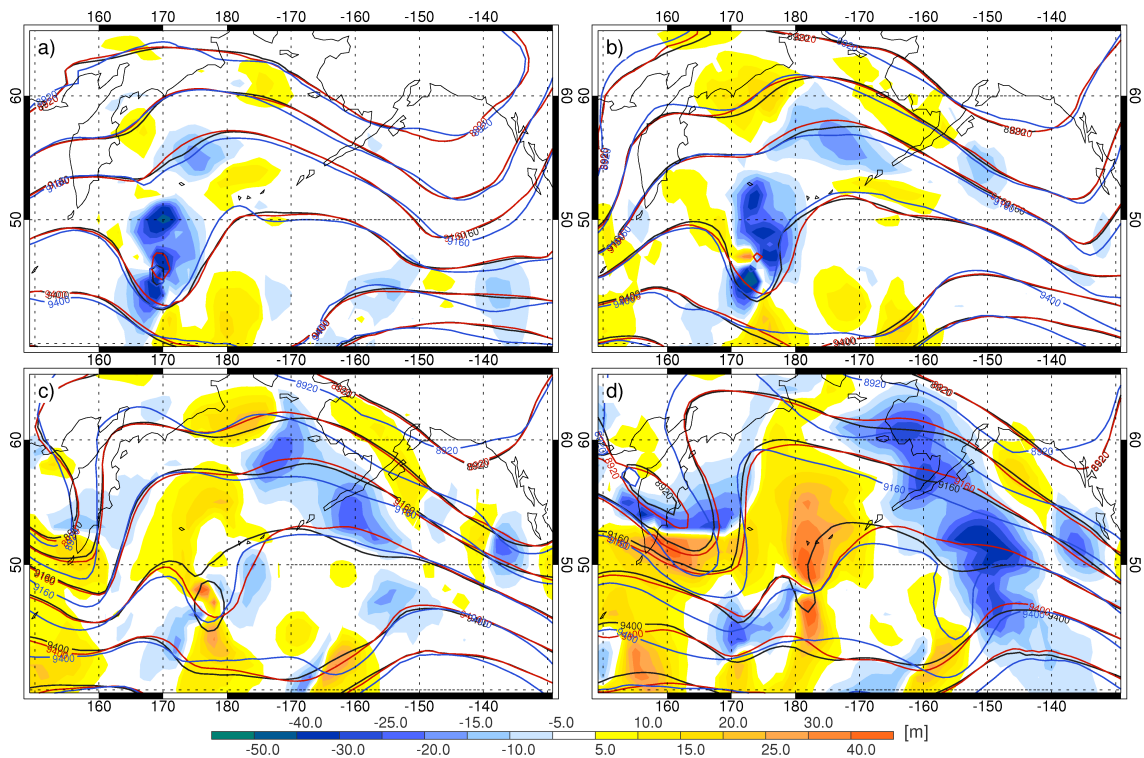

Figure 5.19: Impact on forecast of the geopotential height (colour shaded areas) at 300 hPa for (a) +48 h, (b) +60 h, (c) +72 h and (d) +84 h forecast time. Geopotential height contours of DIAL (black contour lines), CTRL (red contour lines) and analysis fields (blue contour lines).

The DIAL experiment reveals a lower geopotential height error near the centre of the upper level cyclone at +48 h (Figure 5.19(a)). The DIAL forecast produces a less intense cyclone and induces a positional shift which both contributes to the reduc-

tion of the forecast error. Additionally, an improvement of the geopotential height forecast is found in the outflow area of the WCB (see trajectories in Figure 5.15(b)). The reduced ridging in the DIAL experiment better represents the analysis (see also contour lines at ∼55°N/∼175°E). 12 hours later (+60 h, Figure 5.19(b)) the forecast of the maintained cyclone is still improved. The improvement related to the WCB outflow enlarged and moved downstream (ridge axis at about 185°W). After +60 h, the decaying cyclone is less well forecasted by the DIAL forecast which is also related to the general growth of the forecast errors. Especially, the forecast of the upstream approaching cyclone is insufficiently reproduced in both forecasts (compare contour lines in Figure 5.19(c)). Nevertheless, the downstream propagating improvement signal is very likely associated with the initially modified humidity.

5.6   Summary

On 19 September 2008 a T-PARC mission flight took place over the Pacific Ocean east of Japan in the area between the TC Sinlaku and an extratropical cyclone further north. On the leading edge of the developing midlatitude system warm and moist airmasses are incorporated from the area where the lidar observations were made. The water vapour measurements along the ∼3 hour (∼2300 km) flight show a deep moist layer belonging to the southern part of the warm sector of the developing cyclone.

A Lagrangian diagnostic is applied which analyses composite trajectories starting forward and backward in time from every measurement location along the cross section to assign the lidar observations to the WCB embedded in the cyclone. The maximum pressure decrease in 48 hours reveals that large parts of the moist layer close to the sea surface belong to the inflow region of a WCB and are transported within a WCB after the time of the observation. Maximum ascent rates of 650 hPa in 48 hours are diagnosed. Within 12 hours after the observations the air saturates and rises in a coherent tube on the leading edge of the extratropical system. The main latent heat release occurs south and east of Kamchatka. In the outflow region near the tropopause the WCB airmass turns anticyclonically to the east and is transported downstream with the jet stream.

A comparison of the wind and water vapour observations with ECMWF model fields unveils a moist bias in the moist layer over the Pacific Ocean. In the observed part of the WCB inflow the ECMWF overestimates the moisture on average by 1.4 g kg^{-1} (19 %) with peak values of up to 7 g kg^{-1}. A key topic of this thesis is to investigate how moisture errors in the initial conditions affect the forecast of

a WCB and the associated midlatitude cyclone. This is investigated by comparing two forecasts that are initialized with an analysis that overestimates the inflow humidity and another analysis with an improved humidity field that was generated by additionally assimilating DIAL observations. The DIAL assimilation is able to reduce the moist bias in the initial conditions to 0.3 g kg^{-1} by removing moisture in a broad area around the flight track. This area of reduced humidity coincides with the WCB inflow region. Thus, a different amount of moisture is transported into the WCB and ascends to the upper troposphere.

The comparison of the WCB forecasts revealed that the reduction of moisture in the initial conditions is accompanied by a reduction of the latent heat release by 3.5 K from 21 K to 17.5 K along the ascending WCB trajectories. Less PV is produced at lower levels and, additionally, the mean WCB outflow height is $\sim$70 hPa lower. A combination of the trajectory positions with difference fields of geopotential height, surface pressure and PV distribution corroborates a relationship between the initial moisture content in the WCB inflow and the strength of the simulated cyclone. In the forecast with reduced moisture, a weaker cyclone develops and the weaker WCB outflow causes a lower local tropopause (up to 20 hPa) and weaker downstream ridging. The comparison of PV on isentropic surfaces revealed a weaker isentropic PV-gradient and lower jet stream wind speeds (5-15 %) in the downstream ridge.

The forecasts are also verified against the operational analyses of the ECMWF to evaluate the impact on forecast skill. It is shown that the reduction of moisture improves the PV structure in the low and mid-troposphere especially during the period of strong latent heat release in the WCB. An improvement also occurs in the dynamical structure of the cyclone as shown by the positive impact on the kinetic energy of the system. The kinetic energy impact emerges with a temporal shift of $\sim$12 h whereby at first the lower level wind fields showed an improvement which propagates vertically to the upper troposphere. Furthermore, the MinSLP is better represented in the forecast with improved initial conditions. The cyclone did not evolve further after 48 hours and separates from the background flow before it decays at about 3 days after the observations. The improvement of the cyclone forecast therefore did not have considerable impact on the medium range forecast. However, in the WCB outflow a positive impact is found for the geopotential height field of the downstream ridge. This positive signal persists over 4 days and moves downstream over the Pacific Ocean.

Chapter 6

Conclusion and outlook

This thesis investigated WCB inflow regions by analysing airborne remote-sensing observations. It is the first time that lidar observations were employed to characterize the wind and water vapour structure in the inflow regions of WCBs. An unprecedented set of lidar data composed of measurement flights from several field experiments was evaluated to identify WCB encounters and to investigate their representation in the ECMWF global model. The impact of realistic moisture analysis errors on the forecast of an extratropical cyclone and the downstream weather could be quantified. The applied methodology combined observations, model simulations and trajectory calculation and diagnostics. The trajectory-based approach proved to be an appropriate method to associate lidar observations to distinct transport processes, i.e. the transport by a WCB. In the future, the combination of the presented data analysis tools can also be used to study other physical processes (e.g. stratosphere/troposphere exchange) or specific meteorological situations (e.g. polar lows; Wagner et al. (2011)) with lidar observations. In the following the key findings of both case studies are discussed with respect to the three main research questions of this thesis that addressed the WCB identification as well as the reasons for analysis errors in the WCB inflow region and their impact on forecast skill. Finally, an outlook is given that shows the relevance of the obtained results for future research.

Summary of the main results

Research question **Q1** that enquired whether WCB inflows were observed during past field experiments with a deployment of the DIAL (and DWL) was addressed by analysing a large data set of 260 flight hours from 81 research flights during eight research campaigns over the North Atlantic, Europe and the western North Pacific with respect to the occurrence of WCBs. After checking for suitable geographical and meteorological conditions, 17 of the 81 missions were investigated for inter-

sections with WCB trajectories. An analysis of the intersection time and altitude revealed that a WCB inflow region was observed during the ETReC research flight on 19 July 2007 over Spain. A second mission on 19 September 2008 during the T-PARC campaign provided a high data density in the inflow of a WCB over the Pacific Ocean east of Japan. For these two missions, trajectory calculations from every observation point were performed forward and backward in time to identify WCB observations. Based on comparisons with the ECMWF IFS analysis fields insufficiencies in the model analyses were diagnosed for both case studies.

The main focus of the case study on 19 July 2007 was the investigation of possible origins of moisture errors found in the ECMWF IFS that were predicted in the WCB inflow region (research question **Q2**). The flight took place over northern Spain on the leading edge of a large-scale trough that caused the development of a low-level frontal system over France. In the lower troposphere of the warm sector of the evolving cyclone over eastern Spain trajectories indicated a WCB airmass that was strongly lifted after being observed by the lidar. The WCB ascent took place over France ahead of the arriving cold front and the air parcels dispersed in the upper tropospheric outflow over southern Scandinavia and the UK.

A significant positive deviation of about 1 g kg^{-1} (14 %) on average and peak deviations of up to 7 g kg^{-1}, i.e. an overestimation of the predicted humidity, was found in the simulated low-tropospheric WCB inflow region. The comparison of simulated and observed humidity showed that an overestimation of local mixing in the IFS alone cannot explain the moisture bias of the model. A Lagrangian moisture source diagnostic was applied to determine the moisture uptake regions of the observed airmass. It was found that the large moisture deviations occurred within airmasses that were coherently transported from the western Mediterranean towards Spain. They experienced intense moisture uptake over the Ebro valley. Inaccuracies in surface evapotranspiration and turbulent vertical transport of moisture in the atmospheric boundary layer over this region likely contributed to the erroneous low tropospheric humidity in the inflow region of this summertime WCB over Spain in the ECMWF analyses.

The moisture source diagnostic is based on trajectories whose accuracy depends on the accuracy of the driving wind fields, i.e. model analysis fields. It cannot be excluded that an inaccurate representation of horizontal and vertical transport may have influenced the results. However, the coherent distribution along the lidar cross section and the consistent transport from the Mediterranean trajectories strengthens the assumption that the moisture transport over the Ebro-Valley is realistic. The NWP results also depend on the used parameterization scheme for the BL and

surface fluxes. Nevertheless, the general transport pathways should be reproduced consistently, in different models.

The moisture uptake diagnostic was applied successfully for the first time to determine the moisture sources along a lidar cross section. Recent studies also investigated the sources of water vapour, but for different regions and focusing on their connection to precipitation on a climatological time scale (e.g. Sodemann et al. 2008; Gimeno et al. 2010) or on specific exceptionally strong rainfall events (e.g. Sodemann et al. 2009). There has been less focus on shorter time scales and moisture uptake of individual weather systems. Trenberth et al. (2003) stated that the question "Where does the moisture leading to precipitation come from?" requires more attention. This thesis meets their claim for a need of improved knowledge of the water vapour transport in storms and a call for advanced and extended observations of moisture sources. The large potential of using advanced airborne lidar observations in combination with NWP models to analyse the moisture distribution and to unveil shortcomings in NWP is demonstrated in this thesis.

Research question **Q3** was addressed in the second case study on the T-PARC mission on 19 September 2008 that took place east of Japan. The trajectory analysis found an observed WCB inflow airmass that was lifted over the Pacific Ocean and transported towards the US. The observations revealed a moist bias of 1.4 g kg^{-1} in the inflow region simulated by the ECMWF IFS. If the whole moisture in the WCB inflow would condense during the vertical transport, this moist bias additionally would increase θ due to latent heat release by $\sim$3.5 K.

In order to quantify the forecast impact of this bias, two IFS experiments were started; one with the operational moisture bias and the other with initial conditions that were improved by assimilating the DIAL observations. In this way the mean moist bias in the observed part of the WCB inflow could be reduced to 0.3 g kg^{-1}. Both forecast experiments at different lead times and the WCB trajectories were compared to investigate the impact of the modified moisture analysis fields. The comparison confirmed the theoretical considerations of an erroneously increased cyclone intensity and downstream ridging. The forecast with the improved moisture analysis (less moisture at lower levels) caused a weaker WCB, i.e. less latent heat was released at lower levels. For the considered trajectories, the increase of potential temperature was 3.5 K lower in the forecast with the drier WCB inflow humidity. The reduced vertical lifting resulted in a weaker cyclone, i.e. a $\sim$1.5 hPa weaker surface cyclone that is closer to the analysed MinSLP. The upper tropospheric outflow that was found at lower altitudes than in the experiment without DIAL observations, i.e. on average the WCB air parcels are located $\sim$70 hPa lower. The modified

outflow near the tropopause was reflected in a less pronounced ridge downstream and a weaker jet (decrease of wind speed by 5 to 15 %). A comparison with the operational analysis revealed that the improvement of the moisture analysis results in a better forecast of both the midlatitude cyclone and the WCB outflow. The improvement of the dynamical structure of the cyclone started at low levels and propagated vertically to the upper troposphere. The moisture decrease in the initial conditions first improved the PV-distribution and, with a time lag of ∼12 h, the kinetic energy, i.e. the wind field of the cyclone.

Previous studies used model simulations to quantify the total impact of diabatic processes on extratropical cyclones and often found a large case-to-case variability. Less focus was put on the modification of the upper tropospheric waveguide. Conversely, this thesis demonstrates the impact of corrected moisture transport into the WCB on an extratropical cyclone and the downstream weather by accounting for realistic errors in the initial conditions. In this case study, the detected impact on the cyclone is relatively weak. The SLP only varied by 1.5 hPa and the structure of the surface cyclone did not change significantly. However, the reduced advection of low PV air in the weaker WCB modified the upper-level PV distribution and wind speed. The reduction of the tropopause height by up to 10 to 20 hPa (∼500-1000 m) resulted in a weaker ridge building. The PV inversion technique to remove the cyclone from the model fields as shown by Grams et al. (2011), can be considered as the maximum impact scenario of diabatic processes on the upper-level waveguide. In their case study a large reduction of the jet stream wind speed by 25 % was found. This suggests a comparatively strong impact on the waveguide in the present case (decrease of wind speed by 5-15 %). The downstream impact is lower with respect to the studies by Massacand et al. (2001) and Grams et al. (2011). Additionally, the here described cyclone decayed after 48 hours as it detached from the background flow which limited the effect on the midlatitude waveguide. However, as WCBs frequently occur in both hemispheres one may anticipate stronger and longer lasting WCBs where comparable errors may impact the medium range forecast more substantially.

The major difference between the two identified "lucky encounters" of observed WCBs is the location of the research flight. The ETReC WCB inflow was observed over continental Europe whereas the T-PARC case showed a WCB ascent over the Pacific Ocean. As revealed by satellite observations, the vertical moisture transport of the ETReC summer season WCB over the continent was influenced by strong convective cells. Though a data assimilation experiment of the DIAL data in the ECMWF IFS locally improved the moisture analysis in the WCB inflow region, it

showed only minor forecast differences of the WCB and the downstream develop-
ment and was therefore not considered in this thesis. The small impact is probably
related to convective processes that are parameterized in the ECMWF IFS model.
In order to investigate the impact of the moisture bias on the prediction of the large
scale flow and especially on the convection, a higher-resolution mesoscale model sim-
ulation with the different analyses serving as initial and boundary conditions could
give more information about the role of the moisture deviations.

In both cases a substantial moist bias was diagnosed in the analysis fields and
the associated cyclone caused exceptionally high amounts of rain (e.g. Prior and
Beswick 2008; Harnisch et al. 2011). The average deviations in the observed parts
of the inflow were in the order of 1 g kg^{-1}. However, peak deviations reached up to
7 g kg^{-1} in both cases. Despite the obvious importance of a correct representation
of humidity for the forecast skill only few studies identified shortcomings in NWP
models in the surrounding of extratropical cyclones. Previous studies that compared
lidar observations with ECMWF analyses reported deviations in the same order of
magnitude. Flentje et al. (2007) analysed moisture errors over the tropical and
sub-tropical Atlantic and found an overestimated moisture content in the PBL.
Schäfler et al. (2010) investigated the transport of moisture in the surrounding of
an extratropical cyclone over Europe and determined a moist bias at low levels that
reached values up to ∼6 g kg^{-1}.

Harnisch et al. (2011) assimilated all DIAL observations of the T-PARC cam-
paign and found that the mission on 19 September 2008 investigated in this thesis
showed one of the largest forecast improvements of all cases. In this thesis the
physical process that is responsible for the reduced forecast skill of an extratropical
cyclone could be attributed to a WCB. As a major result, evidence is found that
the low level moisture transport into the WCB is crucial for the forecast of the ex-
tratropical cyclone and the downstream ridging. This demonstrates the usefulness
and need of additional moisture observations in the sensitive WCB inflow regions.

Outlook

The fact that substantial moisture errors between ∼1 to 7 g kg^{-1} were observed
in different regions and seasons underlines the importance of further research on the
impact of diabatic processes. A slight improvement of the surface pressure might
be of secondary importance for NWP centres. However, the impact on the upper-
level wave guide which is decisive for the initiation of cyclones further downstream
is less well-investigated and requires more attention in the future to improve the
predictability of the medium range weather forecasting.

A correct forecast of cyclones is indispensable in midlatitudes. Especially, the prediction of so-called high impact weather events (e.g. storms, floodings) with large influence on the society and economy is still an important challenge for current NWP models. Recent research efforts to improve the forecast of high impact weather are consolidated within the WMO global atmospheric research program THORPEX. The main aim of THORPEX is to accelerate improvements in the accuracy of 1-day to 2-week high impact weather forecasts for the benefit of society, the economy and the environment. The European Plan[1] that summarizes the European research efforts and key scientific questions in the framework of THORPEX states that one of the main aims is the investigation of extratropical cyclones and their impacts on the society (like strong wind and precipitation), whereby the role of moisture and the reduction of errors in the initial conditions are denoted as specific scientific challenges. The THORPEX working group "Predictability and Dynamical Processes" proposed an international field experiment named THORPEX - North Atlantic Waveguide and Downstream Experiment (T-NAWDEX) which focuses on the investigation and representation of physical processes that are primarily responsible for degradation in the 1-7 day forecast skill in global NWP models.

In this thesis, it was shown that the WCB inflow region is a sensitive region in terms of errors in the initial conditions that affect the forecast of individual cyclones as well as the upper tropospheric waveguide. The lidar observations of humidity and wind at high resolution and accuracy proved to be valuable to investigate the moisture supply of a WCB and to validate analysis fields of NWP models.

For the future, a more precise investigation of the role of moist processes for the forecast of high impact weather events is absolutely necessary. Therefore airborne observations, e.g. during T-NAWDEX, that are primarily devoted to observe WCBs would be desirable and could contribute to a better understanding of their diabatic processes and the dependence on the moisture supply. Additionally, this would help to identify shortcomings in the initial conditions and model physics. Finally, observations of the interaction of the WCB airstreams with the waveguide would be of great value to understand the impact on downstream Rossby wave intensification.

This will also be addressed in the upcoming research project "Quantifying the role of diabatic processes for forecast errors associated with mid-latitude weather systems – A combined observational, diagnostic and modelling approach" that is part of the German research group PANDOWAE[2]. Novel datasets from the YOTC[3] project,

---

[1]THORPEX European Plan, WMO/TD-No. 1531 WWRP/THORPEX No. 14, 2010, http://www.wmo.int/pages/prog/arep/wwrp/new/documents/European_Plan_5_July_web.pdf

[2]Predictability And Dynamics Of Weather Systems in the Atlantic-European Sector, http://www.pandowae.de/

[3]YOTC = Year of Tropical Convection, http://www.ucar.edu/yotc/index.html

humidity observations from previous field experiments, and numerical model techniques will be applied to better diagnose and quantify the role of diabatic processes for the evolution of different midlatitude weather systems, including cyclones, blockings, and jet streams. Additionally, the design of flight strategies for the planned international field experiment T-NAWDEX is envisaged.

This thesis revealed that for the observation of WCB inflows with lidar a sophisticated flight planning is necessary as the required high data coverage can only be achieved in cloud free regions. The presented methods can be applied in forecast mode during future field experiments to visualize moisture source regions, WCB inflow regions and local cloud conditions as well as the transport pathways of envisaged observations.

Beside the investigation of the role of errors in the supply with moisture especially the investigation of the representation of the latent heat release due to diabatic processes is of great importance as it likewise can impact the forecast skill. The observation of the diabatic processes could be realized by applying in-situ and dropsonde measurements inside clouds. Two Lagrangian flights, i.e. a twice observation of the same WCB airmass separated in time, could give information about the latent heat release and increase of potential temperature.

Appendix A

Influence of the temporal resolution on the WCB detection method

For the calculation of Lagrangian trajectories a multitude of temporal and spatial interpolations are required. During recent years the spatial resolution of NWP models like the IFS has been significantly increased which, finally, improved the accuracy of trajectory calculations. However, it can be supposed that a higher temporal resolution would further increase the accuracy. In this thesis a 3-hourly time resolution in the driving wind fields was used for calculating the trajectories. The 6-hourly analyses were supplemented by short term forecasts. For the comparison of the continuous lidar measurements a special one hourly data output was achieved by performing special forecast experiments with the ECMWF IFS. In the following, the influence of the time resolution on the detection of the WCB will be quantified. To this end, the trajectory calculations shown in Figure A.1 were repeated with a 1- and 6-hourly time resolution of the input wind fields.

Figure A.1 demonstrates the sensitivity of the detection algorithm to the temporal resolution of the driving wind fields. The classifications illustrate observations with ascents larger than 400 hPa (same as used in Figure 4.5) detected by either one, two or by all temporal resolutions. The noisy character of the upper-tropospheric WCB region is also manifested in this diagnostic. This implies that the detection of this WCB is particularly sensitive to the temporal resolution of the driving meteorological analyses. At lower altitudes large areas are found where at least two resolutions detected WCBs (see Figure A.1). The algorithm consistently identifies the air that is lifted right after the observation time independent of the temporal resolution. It would be of great interest to investigate this sensitivity aspect in a
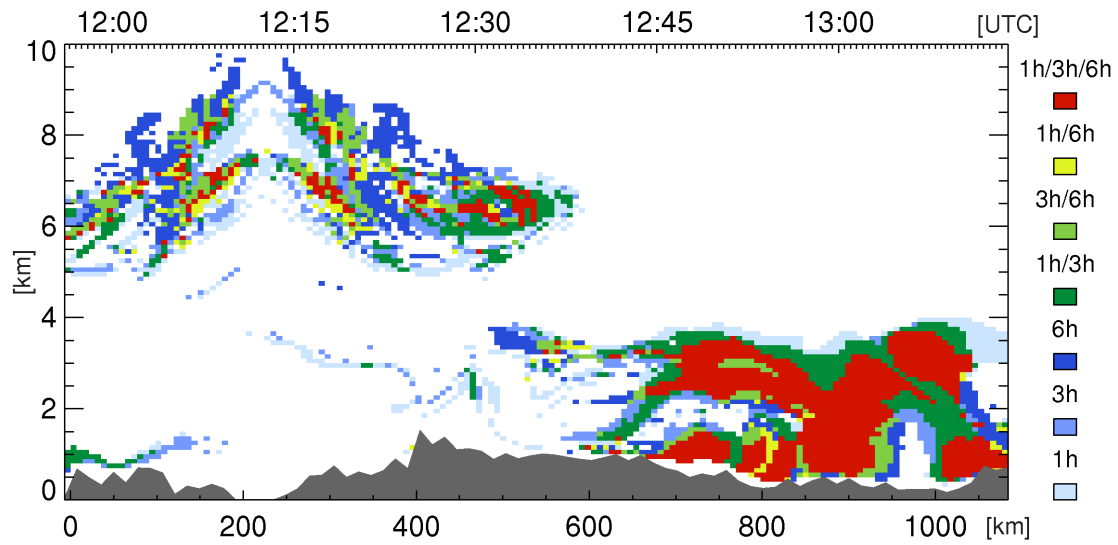
more general way for different cases and regions.

Figure A.1: Location of WCB observations (pressure decrease larger than 400 hPa). Colour coding indicates temporal resolution of the trajectory calculation in which the trajectory is identified as WCB air parcel.

Abbreviations

APD	Avalanche Photodiode
BSR	Back Scatter Ratio
CCB	Cold Conveyor Belt
4DVAR	4-Dimensional Variational
BLH	Boundary Layer Height
COPS	Convective and Orographically Induced Precipitation Study
DIAL	Differential Absorption Lidar
DLR	Deutsches Zentrum für Luft- und Raumfahrt
DWL	Doppler Wind Lidar
ECMWF	European Centre for Medium-Range Weather Forecasts
ERICA	Experiment on Rapidly Intensifying Cyclones
ETReC	European THORPEX Regional Campaign
EUCAARI	European Integrated Project on Aerosol Cloud Climate and Air Quality Interactions
EZMW	Europäisches Zentrum für Mittelfristige Wettervorhersage
FASTEX	Fronts and Atlantic Storm-Track Experiment
FC	Forecast
GALE	Genesis of Atlantic Lows Experiment
IHOP_2002	International H2O Project
IFS	Integrated Forecast System
IPY	International Polar Year
LASER	Light Amplification by Stimulated Emission of Radiation
LIDAR	Light Detection and Ranging
LAGRANTO	Lagrangian Analysis Tool
LOS	Line of Sight
MinSLP	Minimum Sea Level Pressure
MODIS	Moderate Resolution Imaging Spectroradiometer
MTSAT	Multi-functional Transport Satellite
NWP	Numerical Weather Prediction
OPO	Optical Parametric Oscillator
PANDOWAE	Predictability and Dynamics of Weather Systems in the Atlantic-European Sector

PIN	Positive Intrinsic Negative
PBL	Planetary Boundary Layer
PRF	Pulse Repetition Frequency
PV	Potential Vorticity
PVU	Potential Vorticity Units
SAMUM-2	Saharan Mineral Dust Experiment
SCOUT	Stratospheric-Climate Links with Emphasis on the UT/LS
SLP	Sea Level Pressure
T-PARC	THORPEX - Pacific Asian Regional Campaign
THORPEX	The Observing System Research and Predictability Experiment
T-NAWDEX	THORPEX - North Atlantic Waveguide and Downstream Impacts EXperiment
TC	Tropical Cyclone
TROCCINOX	Tropical Convection, Cirrus and Nitrogen Oxides Experiment
UT/LS	Upper Troposphere and Lower Stratosphere
UTC	Coordinated Universal Time
VAD	Velocity Azimuth Display
WALES	Water Vapour Lidar Experiment in Space
WCB	Warm Conveyor Belt
WMO	World Meteorological Organization

Bibliography

Ahmadi-Givi, F., 2002: A review of the role of latent heat release in extratropical cyclones within the potential vorticity framework. *J. Earth Space Phys.*, **28**, 7–20.

Ahmadi-Givi, F., G.C. Craig, and R.S. Plant, 2004: The dynamics of a midlatitude cyclone with very strong latent-heat release. *Q. J. R. Meteorol. Soc.*, **130**, 295–323.

Bader, M., G. Forbes, J. Grant, R. Lilley, and A. Waters, 1995: *Images in weather forecasting. A practical guide for interpreting satellite and radar imagery*, Volume 1. Cambridge: Cambridge University Press.

Berrisford, P., B. Hoskins, and E. Tyrlis, 2007: Blocking and Rossby wave breaking on the dynamical tropopause in the Southern Hemisphere. *J. Atmos. Sci.*, **64**, 2881–2898.

Bethan, S., G. Vaughan, C. Gerbig, A. Volz-Thomas, H. Richer, and D.A. Tiddeman, 1998: Chemical air mass differences near fronts. *J. Geophys. Res.*, **103**, 13413–13434.

Bhawar, R., P. Di Girolamo, D. Summa, C. Flamant, D. Althausen, A. Behrendt, C. Kiemle, P. Bosser, M. Cacciani, C. Champollion et al., 2011: The water vapour intercomparison effort in the framework of the convective and orographically-induced precipitation study: airborne-to-ground-based and airborne-to-airborne lidar systems. *Q. J. R. Meteorol. Soc.*, **137**, 325–348.

Birner, T., 2006: Fine-scale structure of the extratropical tropopause region. *J. Geophys. Res*, **111**, D04104.

Bjerknes, J., 1919: On the structure of moving cyclones. *Geofys. Pub*, **1(2)**, 8 pp.

Bjerknes, J., and H. Solberg, 1922: Life Cycle of Cyclones and the Polar Front Theory of Atmospheric Circulation. *Geofys. Pub.*, **3(81)**, pp. 18.

Blackburn, M., J. Methven, and N. Roberts, 2008: Large-scale context for the UK floods in summer 2007. *Weather*, **63**, 280–288.

Bolton, D., 1980: The computation of equivalent potential temperature. *Mon. Wea. Rev.*, **108**, 1046–1053.

Bösenberg, J., 2005: Differential-Absorption Lidar for Water Vapor and Temperature Profiling. In: *Lidar*, C. Weitkamp (Ed.), Volume 102 of *Springer Series in Optical Sciences*, pp. 213–239. Springer Berlin / Heidelberg. 10.1007/038725101-4_8.

Boutle, I., R. Beare, S. Belcher, A. Brown, and R. Plant, 2010: The moist boundary layer under a mid-latitude weather system. *Boundary-Layer Meteorol.*, **134**, 367–386.

Boutle, I., S. Belcher, and R. Plant, 2011: Moisture transport in midlatitude cyclones. *Q. J. R. Meteorol. Soc.*, **137**, 360–373.

Boutle, I.A., 2009: *Boundary-Layer Processes in Mid-latitude Cyclones*. Ph.D. Thesis, University of Reading.

Brennan, M., G. Lackmann, and K. Mahoney, 2008: Potential vorticity (PV) thinking in operations: the utility of nonconservation. *Wea. Forecasting*, **23**, 168–182.

Browell, E.V., E.F. Danielsen, S. Ismail, G.L. Gregory, and S.M. Beck, 1987: Tropopause fold structure determined from airborne lidar and in situ measurements. *J. Geophys. Res.*, **92**, 2112–2120.

Browning, K., 1997: The dry intrusion perspective of extra-tropical cyclone development. *Meteorol. Appl.*, **4**, 317–324.

Browning, K.A., M.E. Hardman, T.W. Harrold, and C.W. Pardoe, 1973: Structure of rainbands within a mid-latitude depression. *Q. J. R. Meteorol. Soc.*, **99**, 215–231.

Carlson, T.N., 1980: Airflow Through Midlatitude Cyclones and the Comma Cloud Pattern. *Mon. Wea. Rev.*, **108**, 1498–1509.

Charney, J., 1947: The dynamics of long waves in a baroclinic westerly current. *J. Meteor.*, **4**, 135–162.

Cooper, O.R., C. Forster, D. Parrish, M. Trainer, E. Dunlea, T. Ryerson, G. Hübler, F. Fehsenfeld, D. Nicks, J. Holloway, J. Gouw, C. Warneke, J.M. Roberts,

F. Flocke, and J. Moody, 2004: A case study of transpacific warm conveyor belt transport: Influence of merging airstreams on trace gas import to North America. *J. Geophys. Res.*, **109**, D23S08.

Cooper, O.R., J.L. Moody, D.D. Parrish, M. Trainer, T.B. Ryerson, J.S. Holloway, G. Hübler, F.C. Fehsenfeld, and M.J. Evans, 2002: Trace gas composition of midlatitude cyclones over the western North Atlantic Ocean: A conceptual model. *J. Geophys. Res.*, **107**, 4056.

Danielsen, E., 1964: Project Springfield Report. Defense Atomic Support Agency, DASA1517, Washigton D.C. 99 pp.

Davies, H., 1997: Emergence of the mainstream cyclogenesis theories. *Meteor. Z.*, **6**, 261–274.

Davis, C., M. Stoelinga, and Y. Kuo, 1993: The integrated effect of condensation in numerical simulations of extratropical cyclogenesis. *Mon. Wea. Rev.*, **121**, 2309–2330.

Didone, M., 2006: *Performance and Error Diagnosis of Global and Regional NWP Models.* Dissertation, Swiss Federal Institute of Technology, Zürich, Switzerland.

Dirks, R., J. Kuettner, and J. Moore, 1988: Genesis of Atlantic lows experiment (GALE): An overview. *Bull. Amer. Meteor. Soc.*, **69**, 148–160.

Dirren, S., M. Didone, and H.C. Davies, 2003: Diagnosis of 'forecast-analysis' differences of a weather prediction system. *Geophys. Res. Lett.*, **30**, 2060.

Eady, E., 1949: Long waves and cyclone waves. *Tellus*, **1**, 33–52.

Eckhardt, S., A. Stohl, H. Wernli, P. James, C. Forster, and N. Spichtinger, 2004: A 15-Year Climatology of Warm Conveyor Belts. *J. Climate*, **17**, 218–237.

Ertel, H., 1942: Ein neuer hydrodynamischer Wirbelsatz. *Meteor. Z*, **59**, 271–281.

Esler, J.G., P.H. Haynes, K.S. Law, H. Barjat, K. Dewey, J. Kent, S. Schmitgen, and N. Brough, 2003: Transport and mixing between airmasses in cold frontal regions during Dynamics and Chemistry of Frontal Zones (DCFZ). *J. Geophys. Res.*, **108**, 4142.

Flentje, H., A. Dörnbrack, G. Ehret, A. Fix, C. Kiemle, G. Poberaj, and M. Wirth, 2005: Water vapor heterogeneity related to tropopause folds over the North Atlantic revealed by airborne water vapor differential absorption lidar. *J. Geophys. Res.*, **110**, D03115.

Flentje, H., A. Dörnbrack, A. Fix, G. Ehret, and E. Holm, 2007: Evaluation of ECMWF water vapour fields by airborne differential absorption lidar measurements: a case study between Brazil and Europe. *Atmos. Chem. Phys.*, **7**, 5033–5042.

Gimeno, L., R. Nieto, R.M. Trigo, S.M. Vicente-Serrano, and J.I. López-Moreno, 2010: Where Does the Iberian Peninsula Moisture Come From? An Answer Based on a Lagrangian Approach. *J. Hydrometeorol.*, **11**, 421–436.

Grams, C.M., H. Wernli, S.C. Jones, M. Boettcher, J. Campa, U. Corsmeier, S.C. Jones, J.H. Keller, C.J. Lenz, and L. Wiegand, 2011: The key role of diabatic processes in modifying the upper-tropospheric wave guide: a North Atlantic case-study. *Q. J. R. Meteorol. Soc., in press.*

Hadlock, R., and C. Kreitzberg, 1988: The Experiment on Rapidly Intensifying Cyclones over the Atlantic (ERICA) field study: Objectives and plans. *Bull. Amer. Meteor. Soc.*, **69**, 1309–1320.

Harnisch, F., and M. Weissmann, 2010: Sensitivity of typhoon forecasts to different subsets of targeted dropsonde observations. *Mon. Wea. Rev.*, **138**, 2664–2680.

Harnisch, F., M. Weissmann, C. Cardinali, and M. Wirth, 2011: Experimental assimilation of DIAL water vapour observations in the ECMWF global model. *Q. J. R. Meteorol. Soc.*, **137**, 1532–1546.

Harrold, T.W., 1973: Mechanisms influencing the distribution of precipitation within baroclinic disturbances. *Q. J. R. Meteorol. Soc.*, **99**, 232–251.

Hastings, D., P. Dunbar, G. Elphingstone, M. Bootz, H. Murakami, H. Maruyama, H. Masaharu, P. Holland, J. Payne, N. Bryant et al., 1999: The global land one-kilometer base elevation (GLOBE) digital elevation model. Version 1.0. National Oceanic and Atmospheric Administration, National Geophysical Data Center, Boulder, Colorado. *National Geophysical Data Center*. Digital data base on the World Wide Web (URL: http://www. ngdc. noaa. gov/mgg/topo/globe. html) and CD-ROMs.

Hoinka, K.P., and H.C. Davies, 2007: Upper-tropospheric flow features and the Alps: An overview. *Q. J. R. Meteorol. Soc.*, **133**, 847–865.

Holton, J., 2004: *An introduction to dynamic meteorology*, Volume 1. Academic press.

Hoskins, B., 1991: Towards a PV-θ view of the general circulation. *Tellus A*, **43**, 27–35.

Hoskins, B.J., M.E. McIntyre, and A.W. Robertson, 1985: On the use and significance of isentropic potential vorticity maps. *Q. J. R. Meteorol. Soc.*, **11**, 877–946.

Iribarne, J., and W. Godson, 1981: *Atmospheric thermodynamics*, Volume 6. D. Reidel Publishing Company.

Joly, A., K.A. Browning, P. Bessemoulin, J.P. Cammas, G. Caniaux, J.P. Chalon, S.A. Clough, R. Dirks, K.A. Emanuel, L. Eymard, R. Gall, T.D. Hewson, P.H. Hildebrand, D. Jorgensen, F. Lalaurette, R.H. Langland, Y. Lemaitre, P. Mascart, J.A. Moore, P.O. Persson, F. Roux, M.A. Shapiro, C. Snyder, Z. Toth, and R.M. Wakimoto, 1999: Overview of the field phase of the fronts and Atlantic Storm-Track EXperiment (FASTEX) project. *Q. J. R. Meteorol. Soc.*, **125**, 3131–3163.

Joos, H., and H. Wernli, 2011: Influence of microphysical processes on the potential vorticity development in a warm conveyor belt: a case-study with the limited-area model COSMO. *Q. J. R. Meteorol. Soc., in press.*

Kamineni, R., T. Krishnamurti, S. Pattnaik, E. Browell, S. S. Ismail, and R. Ferrare, 2006: Impact of CAMEX-4 Datasets for Hurricane Forecasts Using a Global Model. *J. Atmos. Sci.*, **63**, 151–174.

Keil, C., A. Röpnack, G.C. Craig, and U. Schumann, 2008: Sensitivity of quantitative precipitation forecast to height dependent changes in humidity. *Geophys. Res. Lett.*, **35**, L09812.

Kiemle, C., 2008: Airborne Water Vapor Lidar Measurements. DLR Forschungsbericht 2008–19, DLR Oberpfaffenhofen, Germany. 94 pp.

Kiemle, C., M. Wirth, A. Fix, G. Ehret, U. Schumann, T. Gardiner, C. Schiller, N. Sitnikov, and G. Stiller, 2008: First airborne water vapor lidar measurements in the tropical upper troposphere and mid-latitudes lower stratosphere: accuracy evaluation and intercomparisons with other instruments. *Atmos. Chem. Phys.*, **8**, 5245–5261.

Knippertz, P., and J.E. Martin, 2005: Tropical plumes and extreme precipitation in subtropical and tropical West Africa. *Q. J. R. Meteorol. Soc.*, **131**, 2337–2365.

Kuo, Y.H., M.A. Shapiro, and E. Donall, 1991: The Interaction between Baroclinic and Diabatic Processes in a Numerical Simulation of a Rapidly Intensifying Extratropical Marine Cyclone. *Mon. Wea. Rev.*, **119**, 368–384.

Martin, J., 1999: Quasigeostrophic forcing of ascent in the occluded sector of cyclones and the trowal airstream. *Mon. Wea. Rev.*, **127**, 70–88.

Massacand, A.C., H. Wernli, and H.C. Davies, 2001: Influence of Upstream Diabatic Heating upon an Alpine Event of Heavy Precipitation. *Mon. Wea. Rev.*, **129**, 2822–2828.

Pelly, J., and B. Hoskins, 2003: A new perspective on blocking. *J. Atmos. Sci.*, **60**, 743–755.

Persson, A., and F. Grazzini, 2007: User Guide to ECMWF Forecast Products. *Meteorological Bulletin M3.2.* ECMWF self-published, Version 4.0.

Pfahl, S., and H. Wernli, 2008: Air parcel trajectory analysis of stable isotopes in water vapor in the eastern Mediterranean. *J. Geophys. Res.*, **113**, D20104.

Poberaj, G., A. Fix, A. Assion, M. Wirth, C. Kiemle, and G. Ehret, 2002: Airborne All-Solid-State DIAL for Water Vapour Measurements in the Tropopause Region: System Description and Assessment of Accuracy. *Appl. Phys. B*, **75**, 165–172.

Pomroy, H., and A.J. Thorpe, 2000: The Evolution and Dynamical Role of Reduced Upper-Tropospheric Potential Vorticity in Intensive Observing Period One of FASTEX. *Mon. Wea. Rev.*, **128**, 1817–1834.

Prior, J., and M. Beswick, 2008: The exceptional rainfall of 20 July 2007. *Weather*, **63**, 261–267.

Rabier, F., H. Järvinen, E. Klinker, J. Mahfouf, and A. Simmons, 2000: The ECMWF operational implementation of four-dimensional variational assimilation. I: Experimental results with simplified physics. *Q. J. R. Meteorol. Soc.*, **126**, 1143–1170.

Roiger, A., H. Schlager, A. Schäfler, H. Huntrieser, M. Scheibe, H. Aufmhoff, O.R. Cooper, H. Sodemann, A. Stohl, J. Burkhart, M. Lazzara, C. Schiller, K.S. Law, and F. Arnold, 2011: In-situ observation of Asian pollution transported into the Arctic lowermost stratosphere. *Atmos. Chem. Phys.*, **11**, 16265–16310.

Rossa, A.M., H. Wernli, and H.C. Davies, 2000: Growth and Decay of an Extra-Tropical Cyclone's PV-Tower. *Meteor. Atmos. Phys.*, **73**, 139–156. 10.1007/s007030050070.

Schäfler, A., A. Dörnbrack, C. Kiemle, S. Rahm, and M. Wirth, 2010: Tropospheric Water Vapor Transport as Determined from Airborne Lidar Measurements. *J. Atmos. Oceanic Technol.*, **27**, 2017–2030.

Schultz, D., D. Keyser, and L. Bosart, 1998: The effect of large-scale flow on low-level frontal structure and evolution in midlatitude cyclones. *Mon. Wea. Rev.*, **126**, 1767–1791.

Schultz, D.M., 2001: Reexamining the Cold Conveyor Belt. *Mon. Wea. Rev.*, **129**, 2205–2225.

Schwierz, C., S. Dirren, and H. Davies, 2004: Forced waves on a zonally aligned jet stream. *J. Atmos. Sci.*, **61**, 73–87.

Shapiro, M., and D. Keyser, 1990: Fronts, jet streams, and the tropopause. *Palmén Memorial Volume*, 167–191.

Shapiro, M., H. Wernli, J.W. Bao, J. Methven, X. Zou, J. Doyle, T. Holt, E. Donall-Grell, and P.J. Neiman, 1999: A planetary-scale to mesoscale perspective of the life cycles of extratropical cyclones: The bridge between theory and observations. In: *The Life Cycles of Extratropical Cyclones*, M. A. Shapiro and S. Gronas (Eds.), pp. 139–185. Amer. Meteor. Soc.

Simmons, A., and A. Hollingsworth, 2002: Some aspects of the improvement in skill of numerical weather prediction. *Q. J. R. Meteorol. Soc.*, **128**, 647–677.

Sinclair, V., S. Gray, and S. Belcher, 2008: Boundary-layer ventilation by baroclinic life cycles. *Q. J. R. Meteorol. Soc.*, **134**, 1409–1424.

Sodemann, H., C. Schwierz, and H. Wernli, 2008: Interannual variability of Greenland winter precipitation sources: Lagrangian moisture diagnostic and North Atlantic Oscillation influence. *J. Geophys. Res.*, **113**, D03107.

Sodemann, H., H. Wernli, and C. Schwierz, 2009: Sources of water vapour contributing to the Elbe flood in August 2002 - A tagging study in a mesoscale model. *Q. J. R. Meteorol. Soc.*, **135**, 205–223.

Spichtinger, P., K. Gierens, and H. Wernli, 2005: A case study on the formation and evolution of ice supersaturation in the vicinity of a warm conveyor belt's outflow region. *Atmos. Chem. Phys.*, **5**, 973–987.

Stoelinga, M.T., 1996: A Potential Vorticity-Based Study of the Role of Diabatic Heating and Friction in a Numerically Simulated Baroclinic Cyclone. *Mon. Wea. Rev.*, **124**, 849–874.

Stohl, A., 1998: Computation, Accuracy and Applications of Trajectories - A Review and Bibliography. *Atmos. Environ.*, **32**, 947–966.

Stohl, A., L. Haimberger, M.P. Scheele, and H. Wernli, 2001: An intercomparison of results from three trajectory models. *Meteorol. Appl.*, **8**, 127–135.

Stohl, A., and P. James, 2004: A Lagrangian analysis of the atmospheric branch of the global water cycle. Part I: Method description, validation, and demonstration for the August 2002 flooding in Central Europe. *J. Hydrometeorol.*, **5**, 656–678.

Stohl, A., and T. Trickl, 1999: A textbook example of long-range transport- Simultaneous observation of ozone maxima of stratospheric and North American origin in the free troposphere over Europe. *J. Geophys. Res.*, **104**, 445–462.

Trenberth, K.E., A. Dai, R.M. Rasmussen, and D.B. Parsons, 2003: The Changing Character of Precipitation. *Bull. Amer. Meteor. Soc.*, **84**, 1205–1217.

Vaughan, G., K. Bower, C. Schiller, A.R. MacKenzie, T. Peter, H. Schlager, N.R.P. Harris, and P.T. May, 2008: SCOUT-O3/ACTIVE: High-altitude Aircraft Measurements around Deep Tropical Convection. *Bull. Amer. Meteor. Soc.*, **89**, 647–662.

Vaughan, G., W.E. Garland, K.J. Dewey, and C. Gerbig, 2003: Aircraft Measurements of a Warm Conveyor Belt - A Case Study. *J. Atmos. Chem.*, **46**, 117–129.

Wagner, J.S., A. Gohm, A. Dörnbrack, and A. Schäfler, 2011: Themesoscale structure of a polar low: Airborne lidar measurements and simulations. *Q. J. R. Meteorol. Soc.*, **137**, 1516–1531.

Wallace, J., and P. Hobbs, 2006: *Atmospheric science: an introductory survey*, Volume 92. Academic press.

Wandinger, U., 2005: Introduction to Lidar. In: *Lidar*, C. Weitkamp (Ed.), Volume 102 of *Springer Series in Optical Sciences*, pp. 1–18. Springer Berlin / Heidelberg.

Weckwerth, T.M., D.B. Parsons, S.E. Koch, J.A. Moore, M.A. LeMone, B.B. Demoz, C. Flamant, B. Geerts, J. Wang, and W.F. Feltz, 2004: An Overview of the International H2O Project (IHOP_2002) and Some Preliminary Highlights. *Bull. Amer. Meteor. Soc.*, **85**, 253–277.

Weissmann, M., R. Busen, A. Dörnbrack, S. Rahm, and O. Reitebuch, 2005: Targeted Observations with an Airborne Wind Lidar. *J. Atmos. Oceanic Technol.*, **22**, 1706–1719.

Weissmann, M., and C. Cardinali, 2007: Impact of airborne Doppler lidar observations on ECMWF forecasts. *Q. J. R. Meteorol. Soc.*, **133**, 107–116.

Weissmann, M., R. Langland, C. Cardinali, P. Pauley, and S. Rahm, 2011: Influence of airborne Doppler wind lidar profiles near Typhoon Sinlaku on ECMWF and NOGAPS forecasts. *Q. J. R. Meteorol. Soc.*

Werner, C., 2005: Doppler Wind Lidar. In: *Lidar*, C. Weitkamp (Ed.), Volume 102 of *Springer Series in Optical Sciences*, pp. 325–354. Springer Berlin / Heidelberg.

Wernli, H., 1997: A lagrangian-based analysis of extratropical cyclones. II: A detailed case-study. *Q. J. R. Meteorol. Soc.*, **123**, 1677–1706.

Wernli, H., 2009: Dynamics of large-scale atmospheric flow, Lecture notes.

Wernli, H., and H.C. Davies, 1997: A lagrangian-based analysis of extratropical cyclones. I: The method and some applications. *Q. J. R. Meteorol. Soc.*, **123**, 467–489.

Wirth, M., A. Fix, P. Mahnke, H. Schwarzer, F. Schrandt, and G. Ehret, 2009: The airborne multi-wavelength water vapor differential absorption lidar WALES: system design and performance. *Appl. Phys. B*, **63**.

Wulfmeyer, V., A. Behrendt, H.S. Bauer, C. Kottmeier, U. Corsmeier, A. Blyth, G. Craig, U. Schumann, M. Hagen, S. Crewell, P. Di Girolamo, C. Flamant, M. Miller, A. Montani, S. Mobbs, E. Richard, M.W. Rotach, M. Arpagaus, H. Ruschenberg, P. Schlüssel, M. König, V. Gärtner, R. Steinacker, M. Dorninger, D.D. Turner, T. Weckwerth, A. Hense, and C. Simmer, 2008: The Convective and Orographically-induced Precipitation Study: A Research and Development Project of the World Weather Research Program for Improving Quantitative Precipitation Forecasting in Low-mountain regions. *Bull. Amer. Meteor. Soc.*, **89**, 1477–1486.

Ziv, B., H. Saaroni, M. Romem, E. Heifetz, N. Harnik, and A. Baharad, 2010: Analysis of conveyor belts in winter Mediterranean cyclones. *Theor. App. Clim.*, **99**, 441–455. 10.1007/s00704-009-0150-9.

Acknowledgment